



저작자표시-비영리-변경금지 2.0 대한민국

이용자는 아래의 조건을 따르는 경우에 한하여 자유롭게

- 이 저작물을 복제, 배포, 전송, 전시, 공연 및 방송할 수 있습니다.

다음과 같은 조건을 따라야 합니다:



저작자표시. 귀하는 원저작자를 표시하여야 합니다.



비영리. 귀하는 이 저작물을 영리 목적으로 이용할 수 없습니다.



변경금지. 귀하는 이 저작물을 개작, 변형 또는 가공할 수 없습니다.

- 귀하는, 이 저작물의 재이용이나 배포의 경우, 이 저작물에 적용된 이용허락조건을 명확하게 나타내어야 합니다.
- 저작권자로부터 별도의 허가를 받으면 이러한 조건들은 적용되지 않습니다.

저작권법에 따른 이용자의 권리는 위의 내용에 의하여 영향을 받지 않습니다.

이것은 [이용허락규약\(Legal Code\)](#)을 이해하기 쉽게 요약한 것입니다.

[Disclaimer](#)

약학박사 학위논문

**Studies on the structural and functional
details of two toxin-antitoxin system
complexes from *Streptococcus pneumoniae*
and *Klebsiella pneumoniae***

Streptococcus pneumoniae 와 *Klebsiella pneumoniae* 에서
유래한 두가지 toxin-antitoxin system 단백질의 구조적,
기능적 연구

2021 년 8 월

서울대학교 대학원
약학과 물리약학전공
金 成 龍

**Studies on the structural and functional
details of two toxin-antitoxin system
complexes from *Streptococcus pneumoniae*
and *Klebsiella pneumoniae***

Streptococcus pneumoniae 와 *Klebsiella pneumoniae* 에서
유래한 두가지 toxin-antitoxin system 단백질의 구조적,
기능적 연구

지도교수 이 봉 진

이 논문을 약학박사 학위논문으로 제출함.

2021년 6월

서울대학교 대학원
약학과 물리약학 전공
金成龍

金成龍의 약학박사 학위논문을 인준함.

2021년 7월

위원장	<u> 변영로 </u>
부위원장	<u> 안희철 </u>
위원	<u> 이봉진 </u>
위원	<u> 박성진 </u>
위원	<u> 강성민 </u>

Abstract

Studies on the structural and functional details of two toxin-antitoxin system complexes from *Streptococcus pneumoniae* and *Klebsiella pneumoniae*

Chenglong Jin

Physical Pharmacy Major

College of Pharmacy

The Graduate School

Seoul National University

Toxin–antitoxin (TA) systems regulate key cellular functions in bacteria. TA systems are promising drug targets because they are related to the survival of bacterial pathogens. Here, I report a unique structure of the *Streptococcus pneumoniae* HigBA system and a novel antimicrobial agent that activates HigB toxin, which results in mRNA degradation as an antibacterial strategy. Protein structure-based peptides were designed and successfully penetrated the *S. pneumoniae* cell membrane and exerted bactericidal activity. This discovery is a remarkable milestone in the treatment of antibiotic-resistant *S. pneumoniae*, and the mechanism of bactericidal activity is completely different from

those of current antibiotics. Furthermore, I found that the HigBA complex shows a crossed-scissor interface with two intermolecular β -sheets at both the N and C terminus of the HigA antitoxin. My biochemical and structural studies provide valuable information regarding the transcriptional regulation mechanisms associated with the structural variability of HigAs. My *in vivo* study also revealed the potential catalytic residues of HigB and their functional relationships. In addition, toxin-mimicking or antitoxin mimicking peptides were designed to disrupt HigBA complex and thereby release toxin, providing an approach to development of new conceptual antibiotics. Overall, my results provide insights into the molecular basis of HigBA TA systems in *S. pneumoniae*, which can be applied for the development of new antibacterial strategies.

Klebsiella pneumoniae is one of the most critical opportunistic pathogens. However, structural information on TA systems in *K. pneumoniae* remains lacking; therefore, it is necessary to explore this information for the development of antibacterial agents. Here, the first crystal structure of the VapBC complex from *K. pneumoniae* was presented at a resolution of 2.00 Å. I identified the toxin inhibitory mechanism of the VapB antitoxin through a Mg^{2+} switch, in which Mg^{2+} is displaced by R79 of VapB. This inhibitory mechanism at the active site is unique among the TA systems identified in bacteria. Furthermore, inhibitors, including peptides and small molecules, that activate the VapC toxin were discovered and investigated. These inhibitors can act as antimicrobial agents by disrupting the VapBC complex and activating VapC. My comprehensive investigation on the *K. pneumoniae* VapBC system will help to elucidate an unsolved information in VapBC systems and develop potential antimicrobial agents.

Keywords: Toxin-antitoxin system, HigBA, VapBC, X-ray crystallography, NMR

Student number: 2017-38501

Contents

Abstract	i
Contents	iv
List of Tables	i
List of Figures	ii
General introduction	1
Chapter 1. Structure-based design of peptides that trigger <i>Streptococcus pneumoniae</i> cell death	6
1.1 Introduction	6
1.2 Experimental procedure	7
1.2.1 Cloning, Mutation, Expression and Purification	7
1.2.2 Crystallization, X-Ray Data Collection and Structure Determination.....	11
1.2.3 Electrophoretic Mobility Shift Assay (EMSA) and Isothermal Titration Calorimetry (ITC) Measurements	14
1.2.4 NMR Spectroscopy and NMR Titration Experiment.....	15
1.2.5 <i>In Silico</i> HigBA-DNA Docking.....	16
1.2.6 <i>In Vitro</i> Ribonuclease Assay	17
1.2.7 Kill-and-Rescue Assay.....	17
1.2.8 Circular Dichroism Spectroscopy	17
1.2.9 Designed peptides Adding to the HigBA Complex and Antimicrobial Activity Test	18
1.2.10 <i>In Vivo</i> Cell Growth Assay.....	19
1.2.11 Generation of <i>S. pneumoniae</i> D39 Containing Mutated HigBA	20
1.2.12 Flow Cytometry and Confocal Microscopy	20

1.3 Results	21
1.3.1 Overall Structure of the HigBA Complex.....	21
1.3.2 Structural comparison of HigBA Structures.....	25
1.3.3 DNA-Binding Properties of HigBA.....	28
1.3.4 Active Site of HigB Deduced from Homologs.....	35
1.3.5 Intermolecular Interaction of HigBA.....	37
1.3.6 Ribonuclease Activities of HigB and Its Mutants.....	38
1.3.7 HigBA Complex Disruption by Mimicking Peptide.....	42
1.3.8 Artificial Activation of Toxin by Designed Peptides Can Exert Bactericidal Effects <i>In Vivo</i>	43
1.4 Discussion	46
1.4.1 Insights into the Transcription Regulation Mechanism of the HigBA System.....	46
1.4.2 Application of Structural Studies to the Catalytic Mechanism of HigB	47
1.4.3 HigBA Peptide Derivatives Are Promising New Antimicrobial Agents	49
1.5 Conclusion	51
 Chapter 2. Structural and functional study of the <i>Klebsiella pneumoniae</i> VapBC toxin–antitoxin system, including the development of a substance that activates VapC	
2.1 Introduction	53
2.2 Experimental procedure	55
2.2.1 Cloning, protein purification and mutation	55
2.2.2 Crystallization, data collection and processing.....	58
2.2.3 <i>In vitro</i> RNase assay for VapC and VapC mutants.....	60
2.2.4 Complex disruption assay by the peptides mimicking the VapBC interface	61

2.2.5 Structure-based pharmacophore generation and molecular docking	62
2.2.6 Assay for complex disruption of small molecules that occlude the interface pocket	63
2.2.7 Growth assay and colony forming unit measurement.....	64
2.2.8 Isothermal titration calorimetry	64
2.3 Results.....	65
2.3.1 Overall information on the VapBC complex.....	65
2.3.2 Structural insights into <i>K. pneumoniae</i> VapBC compared with its homologs	67
2.3.3 RNase activity of VapC and unveiling the inhibition mechanism of VapB.....	71
2.3.4 Exploration of peptides that activate VapC by disrupting the interface between VapB and VapC.....	73
2.3.5 Exploration of small molecules that activate VapC by occluding the interface pocket	76
2.3.6 Insights based on binding affinity.....	79
2.4 Discussion	82
2.4.1 Insight into the tertiary structure of <i>K. pneumoniae</i> VapBC complex.....	82
2.4.2 Insight into the mechanism of the <i>in vitro</i> ribonuclease activity of VapC	84
2.4.3 Insight into artificial toxin activation using small molecules and peptides.....	85
2.5 Conclusion	88
References	89
국문초록.....	104

List of Tables

Table 1. Primers used for cloning

Table 2. Data collection and refinement statistics for SeMet-substituted and native structures

Table 3. DNA used in EMSA, ITC and NMR titration

Table 4. Peptides used to disrupt the binding interface of HigBA

Table 5. Thermodynamic parameters upon binding of DNA to HigBA

Table 6. Structural similarity comparison of HigB with its homologs using the Dali server

Table 7. Structural similarity comparison of HigB with its homologs using the Dali server

Table 8. Primers used for cloning and producing mutations

Table 9. Data collection and refinement statistics for SeMet-substituted and native structures

Table 10. Peptides used to disrupt the binding interface of VapBC

List of Figures

- Figure 1.** Expression and purification of HigBA complex from *S. pneumoniae*
- Figure 2.** Generated crystals of HigBA from *S. pneumoniae*
- Figure 3.** Overall structure of heterotetrameric *S. pneumoniae* HigBA
- Figure 4.** Ribbon representation and 90°-rotated diagrams
- Figure 5.** Molecular weight estimates of HigBA and HigA¹⁹⁻⁹⁷ obtained by size-exclusion chromatography
- Figure 6.** Ribbon representation of the HigBA structures
- Figure 7.** Full-length sequence comparison and percentages of amino acid identities
- Figure 8.** Electrophoretic mobility shift assay and ITC results with palindromes in the *higBA* promoter region
- Figure 9.** EMSA study using other palindromic sequences 'A' and 'B' and control DNA 'X'
- Figure 10.** ITC results with palindromes in the *higBA* promoter region
- Figure 11.** 2D ¹H-¹⁵N HSQC spectra of full-length HigA and HigA¹⁹⁻⁹⁷
- Figure 12.** DNA-binding properties determined from NMR titration data and *in silico* docking model of the HigBA-DNA complex
- Figure 13.** Active site residues of *S. pneumoniae* HigB compared to those of other HigBs, and overall structures of ribonucleases from similar families

Figure 14. Crossed-scissor heterodimeric interface between HigB and HigA

Figure 15. *In vitro* ribonuclease activity assays of *S. pneumoniae* HigB with its mutants

Figure 16. Validation tests for toxin mutants and peptide mimetics

Figure 17. Toxicity and antitoxicity assay of HigB variants and their combinations with HigA in *E. coli*

Figure 18. Protein complex disruption and subsequent *in vivo* cell feasibility assays using binding region-mimicking peptides

Figure 19 Active site of HigB from *S. pneumoniae*

Figure 20. Expression and purification of VapBC complex from *K. pneumoniae*

Figure 21. Generated crystals of VapBC from *K. pneumoniae*

Figure 22. Growth assay and CFU measurement

Figure 23. Overall structural information on *K. pneumoniae* VapBC

Figure 24. Structural comparison of *K. pneumoniae* VapBC with its homologues

Figure 25. Active site and RNase activities of VapC

Figure 26. Heterodimeric interface of the VapBC complex and efficacy of complex disruption using the designed peptides

Figure 27. The effects of the peptides and small molecules on free VapC

Figure 28. Surface pockets on VapC (PDB ID: 7BY3) and efficacy of final compounds expressed with molecular docking

Figure 29. Inhibition curves of compounds

Figure 30. ITC assays

General introduction

Toxin–antitoxin (TA) systems were first discovered as plasmid genes in the 1980s, which is related to the inheritance of plasmids in daughter cells (1). TA system modules were later found in the most bacterial chromosomes, and their roles in bacterial cells have been intensively studied (2). TA systems consist of two or more adjacent genes encoding a toxin protein and an antitoxin. Toxins involved in diverse cellular functions, such as protein synthesis inhibition, DNA replication inhibition, and cell wall synthesis inhibition in response to unfavorable growth conditions. Usually, toxins as ribonucleases degrade mRNA in a specific or nonspecific fashion, and some toxins play roles as gyrase inhibitors and kinases. Their cognate antitoxins neutralize the toxins and regulate the transcription levels of TA operons (3,4). Recently, an abundance of TA systems in pathogenic bacteria has been reported by advances in genome sequencing and bioinformatics (5,6).

TA systems are classified into type I–VI TA systems. Type I TA systems consist of a noncoding RNA antitoxin and a toxin-encoding mRNA. Type II TA systems consist of a protein antitoxin and its cognate protein toxin. Type III TA systems consist of a small RNA antitoxin that binds directly to the toxin protein as an inhibitor. Similar to the type II TA system, both the toxin and the antitoxin of a type IV TA system are proteins, although their inhibition mechanism is not direct binding. Instead, these proteins play opposing roles in bacterial filaments. In a type V TA system, a ribonuclease antitoxin degrades the mRNA toxin. The protein toxin of a type VI TA system is neutralized by the protein antitoxin, which is degraded by cellular proteases (7).

Notably, TA systems occur more often in pathogenic bacteria than nonpathogenic kin, which indicate that TA systems would be relevant to pathogenicity of bacteria. For example, pathogenic bacteria such as *Mycobacterium tuberculosis* H37Rv possess 76 TA systems, while non-pathogenic bacteria such as *Mycobacterium smegmatis* are identified to utilize only 5 TA systems. Up to date, many structures of TA systems have been successfully analyzed through X-ray crystallography or NMR spectroscopy. For example, through searching from RCSB Protein Data Bank (<https://www.rcsb.org/>), 6 MazEF complexes, 6 RelBE complexes, 11 VapBC complexes, 4 HipBA complexes, 2 CcdAB complexes, and 4 YoeB/YefM complexes from type II TA system have been identified; and 1 ToxIN complex and 1 CptIN complex from type III TA system have also been analyzed; and 1 GhoS antitoxin from type V TA system and 2 SocA antitoxin from type VI TA system have been identified. However, none of the tertiary structure of Type I or type IV TA system have been investigated to date. Obviously, researchers focus on type II TA systems in recent years. The bacterial type II TA system contains two proteins, a biophysically stable toxin and a relatively labile antitoxin. In the normal state, the expression levels of the toxin and antitoxin are well-harmonized, so bacteria can normally survive because the antitoxin counteracts any harmful effect of the toxin (8). However, the labile antitoxin degrades faster under stress conditions, including antibiotic treatment, nutrient starvation, and unfavorable temperature. Then, the toxin is freely released from the antitoxin, and the bacteria suffer damage because of the toxicity of the released toxin (9). As classified TA systems by bacterial species, TA systems from *M. tuberculosis*, *Escherichia coli*, and *Salmonella typhimurium* have the most results of structural study. However, few TA systems from *Streptococcus pneumoniae* and *Klebsiella pneumoniae*

have been studies to date. Therefore, it is valuable to study about TA systems from these two kinds of pathogenic bacteria.

S. pneumoniae is a Gram-positive species of bacteria that causes disease mainly through respiratory infections (10). Diseases caused by *pneumococcal* species include otitis, sinusitis meningitis, bacteremia, and pneumonia (11). The infections caused by *S. pneumoniae* resulted in 515 000 death in 2015 (12), with 335 000 of which in children under 5 years of age (13). Patients infected with *S. pneumoniae* are mainly treated with antibiotics, such as penicillin, cephalosporins, macrolides, and quinolones (14). However, the advent of increasing antibiotic resistance strains of *S. pneumoniae* (15) requires the development of novel therapeutics.

K. pneumoniae is one of the most critical opportunistic pathogens. It is widespread in the environment, including in water, on solids or on leaf surfaces. *K. pneumoniae* is responsible for infections of the upper respiratory tract, urinary tract and bloodstream and causes pneumonia (16). Currently, *K. pneumoniae* is considered a significant threat to the health of people worldwide. It possesses an extraordinarily plastic genome and a great tendency to develop antibiotic resistance. In particular, drug-resistant *K. pneumoniae*, with resistance even to carbapenems, has emerged as a global problem (17).

In fact, there are several mechanisms of resistance in pathogenic bacteria (18). They include mutations in lipopolysaccharide structure, which is the binding target for the polymyxin class of antibiotics (19); the loss of porins (20), which reduce the efficacy of drug movement through bacterial outer membrane; the expression of β -lactamases in periplasmic space, which specifically degrade several β -lactam classes of antibiotics such as penicillin (20), cephalosporins (21); overexpression of transmembrane efflux pump

(22), which expels the antibiotics such as quinolones, aminoglycosides from bacterial cytoplasm before they could have an effect; expression of antibiotic-modifying enzymes (23), which make some antibiotics such as aminoglycosides or ciprofloxacin lose their functions; target site mutations such as DNA gyrase or topoisomerase IV, which prevent quinolone to interact with its site of action (24); ribosomal mutations or modifications, which prevent tetracyclines or aminoglycosides from inhibiting protein synthesis (25). In this way, bacteria have created several mechanisms of resistance against a variety of antibiotics through their own evolution. Thus, it is urgently needed to explore new conceptual antibiotics.

In the previous study, there are three major approaches to utilize type II TA system as antibacterial strategies. One is an artificial activation of toxin, which is accomplished by designing the potent peptides or small molecules using virtual screening and molecular docking. In this regard, peptides or small molecules could be designed to merely 'attack' the binding pocket of TA complex to release free toxin, which still possess its active site. Subsequently, the activated toxin results in rapid killing of target bacteria. Another approach that could be considered is to promote degradation of antitoxin by Lon or Clp proteases, resulting in toxin activation and hence triggering bacteria death. In this case, several previous studies have shown that overexpression of Lon protease or activation of Clp protease effectively leads to vitalize the toxin and hence cell death (26-28). In addition, it is demonstrated that the half-life of antitoxin is relatively low because of its flexibility. A promoter binder could be designed to inhibit the expression of antitoxin, resulting in loss of compensation for the toxin. However, the complicated and large binding interface between antitoxin and promoter DNA could be obstacles in designing

the promotor binder in this regard. As a result, the former approach, which includes the design of peptides or small molecules, is the most considerable.

Chapter 1. Structure-based design of peptides that trigger *Streptococcus pneumoniae* cell death

1.1 Introduction

Streptococcus pneumoniae is a Gram-positive, lancet-shaped, and facultative anaerobic bacteria with almost 100 known serotypes. It could cause several diseases such as pneumoniae, meningitis, bacteremia, acute otitis media, sinusitis, etc. Among them, pneumoniae is the most common disease caused by *S. pneumoniae*, which contains a variety of symptoms such as fever, cough, chain pain, rapid breathing. Up to date, genome from two kinds of *S. pneumoniae* strains have been completely sequenced, which include *S. pneumoniae* TIGR4 and *S. pneumoniae* D39. In this chapter, the type II TA systems from *S. pneumoniae* TIGR4 were focused (29).

The most widely distributed type II TA systems comprise the thermodynamically stable toxin and the unstable antitoxin. The antitoxin is cleaved by some cellular proteases and has a lower half-life than that of the toxin. Therefore, the host depends on a continuous supply of antitoxin to neutralize the toxicities of toxins (9). Currently, seven type II TA loci have been reported in *S. pneumoniae* TIGR4: three RelBEs, phd-doc, HicBA, HigBA, and one unidentified family. Among these seven TA systems, HigBA systems share limited sequence homology among HigB toxins and HigA antitoxins exhibit considerable structural variability (30-32).

Here, the complex structure of HigBA from *S. pneumoniae* was presented as determined by X-ray crystallography. The crossed-scissor constitutes a new type of interface between HigB and HigA. The binding interface showed critical residues in the formation of the HigBA complex. HigB from *S. pneumoniae* showed *in vitro* ribonuclease activity, and the mRNA cleavage mechanism was scrutinized through numerous single point mutations. The peptides that mimicked toxin or antitoxin helices could hinder HigBA complex formation. These peptides could penetrate *S. pneumoniae* and exert bactericidal activity. The antitoxin does not block the active site of HigB in the HigBA complex structure, thus revealing that peptide binding may allosterically inhibit HigB activity. HigA has DNA-binding properties through its helix-turn-helix motif (HTH) and regulates HigBA expression. The residues of HigA that are important for DNA binding were investigated by nuclear magnetic resonance (NMR). This approach may contribute to my understanding of the structure–function relationships of TA systems, including the HigBA system. My biochemical and structural studies will provide valuable information and insights into the molecular basis of TA systems as an antibacterial target.

1.2 Experimental procedure

1.2.1 Cloning, Mutation, Expression and Purification

The genes encoding *S. pneumoniae* (strain TIGR4) HigB (*sp_1143*) and HigA (*sp_1144*) were amplified by polymerase chain reaction (PCR) using the primers *higB*-F, *higB*-R, *higA*-F, and *higA*-R (Table 1). The restriction enzymes Nde1 and Xho1 were used to cut the PCR products and vectors [pET-28b(+) for *higB* and pET-21a(+) for *higA*]

(Novagen, USA). The cloned plasmids of *higB* and *higA* were cotransformed into *E. coli* Rosetta (DE3) pLysS for the overexpression of the HigBA complex. The cells were grown in Luria-Bertani (LB) medium containing 50 µg/ml ampicillin and 30 µg/ml kanamycin at 310 K until an OD₆₀₀ of 0.5 was reached. The overexpression of the target proteins was induced by 0.5 mM isopropyl-β-D-thiogalactopyranoside (IPTG) with an additional incubation for 4 h (Figure 1A). The cells were harvested at 11,355 x g. The harvested cells were lysed by ultrasonication in buffer A (20 mM Tris-HCl, pH 7.9, 500 mM NaCl) containing 10% (v/v) glycerol. The entire lysate was centrifuged at 28,306 x g for 1 h at 277 K. The supernatant was loaded onto an open Ni²⁺-affinity column (Qiagen, Germany), pre-equilibrated with buffer A and washed with buffer A containing 50 mM imidazole. The protein bound to the column was eluted by an imidazole gradient (100–700 mM) (Figure 1B). For further purification using ion-exchange chromatography, the buffer containing the target proteins was changed to buffer B (50 mM MES, pH 6.0). Proteins were loaded onto a HiTrap SP column (GE Healthcare, UK) pre-equilibrated with buffer B and eluted with a NaCl gradient (0–1500 mM). As a final step, size-exclusion chromatography was conducted using a HiLoad 16/600 Superdex 200 prep-grade column (GE Healthcare, UK) in a final buffer (50 mM MES, pH 6.0, 500 mM NaCl). The purified proteins were verified by sodium dodecyl sulfate-polyacrylamide gel electrophoresis and concentrated using an Amicon Ultra centrifugal filter unit (Merck Millipore, USA) in preparation for crystallization. The HigBA complex displaced by selenomethionine (SeMet) (Calbiochem, USA) was expressed and purified by the same procedure, except M9 medium containing extra essential amino acids was used for cell growth.

For the ribonuclease activity assay of HigB, 8 M urea was added to purified HigBA complex as a denaturant. The final buffer containing 8 M urea and HigBA complex was incubated at 293 K for 4 h. Size-exclusion chromatography was conducted on the denatured HigBA complex using a HiLoad 16/600 Superdex 200 prep-grade column (GE Healthcare, UK). The eluted fraction containing HigB was diluted to remove the denaturant and enable refolding, and the denatured HigB was diluted by a factor of one thousand with the final buffer. Mutated forms of HigB were constructed and subjected to a ribonuclease activity assay. Ten residues of HigB were mutated to alanine (F17A, M20A, D40A, L44A, D61A, E66A, R68A, R73A, F90A and K92A) (Table 1) using an EZ Change Site-Directed Mutagenesis Kit (Enzymomics, South Korea). The protein complexes of HigB mutants with the WT HigA were expressed and purified by the same procedure used for the WT HigBA. Each HigB mutant was generated by denaturation and refolding by the same procedure used for the WT HigB.

A HigA construct consisting of residues 19 to 97 was used for the NMR experiments. The genes encoding *higA*¹⁹⁻⁹⁷ were amplified by PCR using primers *higA*-F¹⁹⁻⁹⁷ and *higA*-R (Table 1) and cloned into pET-28b(+) (Novagen, USA), resulting in a twenty-residue tag (MGSSHHHHHSSGLVPRGSH) at the N-terminus. The plasmid encoding *higA*¹⁹⁻⁹⁷ was transformed into *E. coli* Rosetta (DE3) pLysS for overexpression, and the cells were grown in M9 minimal medium supplemented with 1 g/L [¹⁵N] ammonium chloride and 1 g/L [¹³C] glucose as the sole nitrogen and carbon sources, respectively. The purification procedure was the same as that used for the complex. To remove the N-terminal tag, thrombin was added to the purified protein (10 units/ml) and incubated at 293 K overnight. Finally, size-exclusion chromatography was conducted using a HiLoad 16/600 Superdex 200 prep-grade column (GE Healthcare, UK) in buffer (50 mM MES,

pH 6.0, 100 mM NaCl). The concentration of HigA¹⁹⁻⁹⁷ was measured based on the Bradford method (33) because of the absence of aromatic amino acid residues.

Table 1. Primers used for cloning

Primer	Sequence
<i>higB</i> -F ^a	5'-GGAATTC <u>CATATG</u> ATGCATAATATCTATTTT-3'
<i>higB</i> -R ^b	5'-CCGCTC <u>GAGT</u> TATTTTTCATTGTCTAAAC-3'
<i>higA</i> -F ^a	5'-GGAATTC <u>CATATG</u> ATGAAAAATAATGCTATTGG-3'
<i>higA</i> -R ^b	5'-CCGCTC <u>GAGT</u> TAAACCTGCTCATGCTCTAATGGT-3'
<i>F17A</i> -F ^a	5'-GGCAATGAGCCTGTTGCTGATTATATGCGAGAG-3'
<i>F17A</i> -R ^b	5'-CTCTCGCATATAATCAGCAACAGGCTCATTGCC-3'
<i>M20A</i> -F ^a	5'-CCTGTTTTTGATTATGCGCGAGAGCTTACCAGT-3'
<i>M20A</i> -R ^b	5'-ACTGGTAAGCTCTCGCGCATAATCAAAAACAGG-3'
<i>D40A</i> -F ^a	5'-CTTAATAAAATTAATGCTTATATTGAGTTGTTA-3'
<i>D40A</i> -R ^b	5'-TAACAACCTCAATATAAGCATTAATTTTATTAAG-3'
<i>L44A</i> -F ^a	5'-AATGATTATATTGAGGCGTTAAGCCAACATGGA-3'
<i>L44A</i> -R ^b	5'-TCCATGTTGGCTTAACGCCTCAATATAATCATT-3'
<i>D61A</i> -F ^a	5'-TATATTAAGCATTTAGCTGCTGAAATTTGGGAG-3'
<i>D61A</i> -R ^b	5'-CTCCCAAATTCAGCAGCTAAATGCTTAATATA-3'
<i>E66A</i> -F ^a	5'-GATGCTGAAATTTGGGCGCTGAGACCACTTAGA-3'
<i>E66A</i> -R ^b	5'-TCTAAGTGGTCTCAGCGCCCAAATTCAGCATC-3'
<i>R68A</i> -F ^a	5'-GAAATTTGGGAGCTGGCACCCTTAGAGATAGA-3'
<i>R68A</i> -R ^b	5'-TCTATCTCTAAGTGGTGCCAGCTCCCAAATTC-3'
<i>R73A</i> -F ^a	5'-AGACCACTTAGAGATGCAATTTTATTTGTTGCT-3'
<i>R73A</i> -R ^b	5'-AGCAACAAATAAAATTGCATCTCTAAGTGGTCT-3'
<i>F90A</i> -F ^a	5'-GTTTTACTGCATCATGCTATGAAAAGGACACAG-3'
<i>F90A</i> -R ^b	5'-CTGTGTCCTTTTCATAGCATGATGCAGTAAAAC-3'
<i>K92A</i> -F ^a	5'-CTGCATCATTTTATGGCAAGGACACAGAAAACA-3'
<i>K92A</i> -R ^b	5'-TGTTTTCTGTGTCCTTGCCATAAAATGATGCAG-3'
<i>higA</i> ¹⁹⁻⁹⁷ -F ^a	5'-GGAATTC <u>CATATG</u> AGCAAAGAGGAAATTTTGG-3'

^{a, b} F and R represent forward and reverse, respectively. Enzyme sites are underlined.

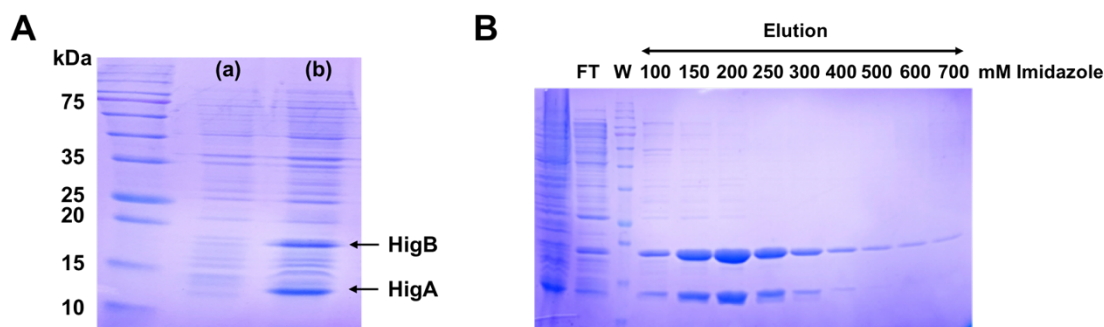


Figure 1. Expression and purification of HigBA complex from *S. pneumoniae*. (A) Expression of HigBA complex from *S. pneumoniae*. Lanes: a, uninduced whole-cell; b, induced whole-cell. (B) Purification of HigBA complex from *S. pneumoniae* by gradient elution using an open Ni²⁺-affinity column. FT, flowthrough; W, wash.

1.2.2 Crystallization, X-Ray Data Collection and Structure

Determination

Crystals of the HigBA complex were grown using the sitting-drop vapor diffusion method at 293 K by mixing equal volumes (0.5 μ l each) of the protein solution (11 mg/ml in 50 mM MES, pH 6.0, 500 mM NaCl) and the reservoir solution (20% (w/v) PEG 1000, 100 mM KH₂PO₄/ Na₂HPO₄, pH 6.2, 200 mM NaCl) (Figure 2). A cryoprotectant solution consisting of 25% (v/v) glycerol was added to the reservoir solution for data collection under a liquid nitrogen stream. The crystal was vitrified in the cold nitrogen gas stream, and the data were collected using an ADSC Quantum Q270r CCD detector at beamline 5C of the Pohang Light Source, Republic of Korea. Crystals of HigBA belonged to the *monoclinic* space group P2₁, with unit cell parameters of $a = 74.903 \text{ \AA}$, $b = 74.403 \text{ \AA}$, $c = 98.321 \text{ \AA}$, $\alpha = \gamma = 90.00^\circ$, $\beta = 90.08^\circ$ for the native complex and $a = 74.575 \text{ \AA}$, $b = 67.038 \text{ \AA}$, $c = 87.717 \text{ \AA}$, $\alpha = \gamma = 90.00^\circ$, $\beta = 94.22^\circ$ for the SeMet-labeled complex. The structure of the HigBA complex was first phased at 2.80 \AA resolution by single-

wavelength anomalous dispersion using SeMet. The structure of the HigBA complex was calculated using 2.30 Å resolution diffraction data of the native complex with a molecular replacement based on the SeMet protein model. The detailed statistical information is described in Table 2. PHENIX (34) was first used to automatically build a residue, and the remaining residues were built in COOT (35) to provide the final model. The R_{work} and R_{free} (36) values were calculated by REFMAC and PHENIX for refinement (34,37). The overall geometry was validated using MolProbity (38). PyMOL was used to generate figures (39). The electrostatic potential surfaces were calculated using the Adaptive Poisson-Boltzmann solver (APBS) method (40).

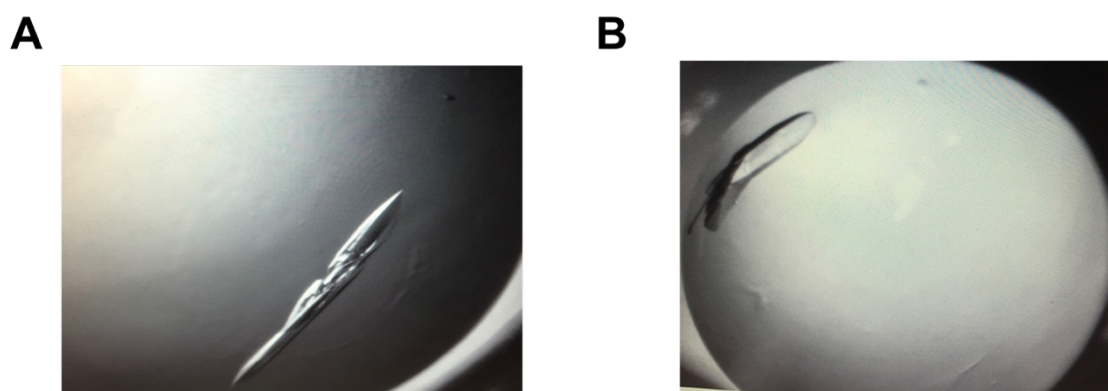


Figure 2. Generated crystals of HigBA from *S. pneumoniae*. (A) Crystal of native form. (B) Crystal of SeMet form.

Table 2. Data collection and refinement statistics for SeMet-substituted and native structures.

(a) Data collection details. Values in parentheses are for the highest-resolution shell.

Data set	SeMet	Native
X-ray source	5C beamline of PLS, Korea	5C beamline of PLS, Korea
X-ray wavelength (Å)	0.9794	0.9794

Space group	P2 ₁	P2 ₁
Unit cell parameters		
a, b, c (Å)	74.575, 67.038, 87.717	74.903, 73.403, 98.321
α , β , γ (°)	90.0, 94.223, 90.0	90.0, 90.077, 90.0
Resolution range (Å)	50.0-2.80	50.0-2.30
Molecules per ASU	2 HigBA heterotetramers	2 HigBA heterotetramers
Observed reflections (>1 σ)	235871	163245
Unique reflections	21414	45671
$\langle I / \sigma(I) \rangle$	24.8 (1.13) ^e	23.7 (1.61) ^e
Completeness (%)	99.9 (99.6) ^e	97.0 (100.0) ^e
Multiplicity ^a	11.0 (9.0) ^e	3.6 (3.8) ^e
R_{merge} (%) ^b	13.2 (139.8) ^e	10.3 (70.9) ^e
CC _{1/2} , CC	(0.651, 0.888) ^e	(0.823, 0.950) ^e

(b) Refinement statistics

Data set	SeMet	Native
R_{work} ^c (%)		21.6
R_{free} ^d (%)		25.4
No. of atoms / average <i>B</i> factor (Å ²)		6810 / 60.0
RMSD ^f from ideal geometry		
Bond distance (Å)		0.006
Bond angle (°)		1.135
Ramachandran statistics		
Most favored regions (%)		95.60
Additional allowed regions (%)		4.40
Residues in disallowed regions (%)		0.00
PDB accession code		6AF4

^a $N_{\text{obs}}/N_{\text{unique}}$

^b $R_{\text{merge}} = \Sigma (I - \langle I \rangle) / \Sigma \langle I \rangle$

^c $R_{\text{work}} = \Sigma_{hkl} ||F_{\text{obs}}| - k |F_{\text{calc}}|| / \Sigma_{hkl} |F_{\text{obs}}|$

^d R_{free} was calculated in the same way as R_{work} , but with 5% of the reflections excluded from the refinement.

^e Values in parentheses indicate the highest-resolution shell.

^f Root mean square deviation (RMSD) was calculated with REFMAC.

1.2.3 Electrophoretic Mobility Shift Assay (EMSA) and Isothermal Titration Calorimetry (ITC) Measurements

The binding affinities of HigA and HigBA to the palindromic sequence in their own operator region were estimated by EMSA. Typically, type II antitoxins interact with DNA via symmetric palindromic stretches that are approximately 15–30 nucleotides long called inverted repeats. For *higBA*, I was able to locate several inverted repeats within the promoter region. Four DNA duplexes were selected and termed *Pal-I*, *Pal-II*, *Pal-III* and *Pal-IV* (Table 3). Control experiments were also performed with DNA ‘X’ and the two other palindromic sequences ‘A’ and ‘B’ (Table 3). Purified DNA duplexes were purchased from Bioneer (Daejeon, South Korea). Reaction mixtures (10 μ l) containing 0.01 mM of duplex DNA and different protein concentrations (a series of protein concentrations, with the HigA dimer and HigBA hetero-tetramer ranging from 0 to 0.6 mM) were prepared in binding buffer (50 mM MES, 500 mM NaCl, pH 6.0) and incubated for 30 min at 293 K. The reaction mixtures were electrophoresed on a 0.5% agarose gel with 0.5x TBE for 20 min. The results were visualized using a Printgraph 2M (ATTO, Japan).

ITC experiments were performed using an iTC200 calorimeter (Malvern Instruments, UK) at 25°C. The proteins and promoter dsDNAs were prepared in a buffer consisting of 50 mM MES, pH 6.0, and 100 mM NaCl for both HigA and HigBA. The DNA duplexes used in the ITC measurements were the same as those used in the EMSA (Table 3). Affinity experiments were conducted with the protein solution (10 μ M HigA dimer and HigBA hetero-tetramer, 320 μ l) in the cell and the dsDNA solution (600 μ M) as the injected titrant. In total, 19 injections performed at 180 s intervals were used for

data collection. The MicroCal Origin software was used for curve fitting to calculate the binding affinity (K_d), the enthalpy of binding (ΔH), the entropy of binding (ΔS) and the stoichiometry (n). The raw data were fitted using a one-site binding model. The Gibbs free energies (ΔG) were calculated using the standard equation $\Delta G = \Delta H - T\Delta S$.

1.2.4 NMR Spectroscopy and NMR Titration Experiment

For the NMR analysis, HigA¹⁹⁻⁹⁷ was uniformly labeled with ¹³C and ¹⁵N and prepared in 20 mM MES, pH 6.0, 50 mM NaCl, 1 mM EDTA, 0.1 mM PMSF, and 10% D₂O. All NMR measurements were conducted at 308 K using an AVANCE 800 MHz spectrometer equipped with a cryogenic probe (Bruker BioSpin, USA). ¹H, ¹³C, and ¹⁵N chemical shift assignments for the backbone nuclei were obtained using 2D ¹H-¹⁵N HSQC and a set of triple resonance experiments to obtain the HNC(O), HN(CA)CO, HNCA, HN(CO)CA, HNCACB and HN(CO)CACB spectra. Data were processed using NMRPipe and nmrDraw (41) and further analyzed using NMRviewJ (42).

NMR titration experiments on ¹⁵N-labeled HigA¹⁹⁻⁹⁷ with the promoter dsDNA *Pal-III* (Table 3) were conducted by acquiring the ¹H-¹⁵N HSQC spectra. Throughout the NMR titration experiments, the concentration of the HigA¹⁹⁻⁹⁷ dimer was maintained at 0.5 mM, and the concentration of the promoter dsDNA was increased from 0 to 0.1 mM. The chemical shift perturbation (CSP) was calculated and analyzed using Equation 1, where $\Delta\delta_N$ and $\Delta\delta_H$ are the CSP values of the amide nitrogen and proton, respectively. The intensity ratio was calculated by dividing the peak intensity of the last spectrum by the peak intensity of the first spectrum:

$$\Delta\delta_{\text{avg}} = [(0.2 \times \Delta\delta^2_N + \Delta\delta^2_H) / 2]^{1/2}$$

Table 3. DNA used in EMSA, ITC and NMR titration.

DNA	Sequence
<i>Pal-I-F</i> ^a	AGCATCTAGGAACTAGGTGCT
<i>Pal-I-R</i> ^b	AGCACCTAGTTTCCTAGATGCT
<i>Pal-II-F</i> ^a	AACTTAAAAGTATTTACAAACAATAACTTTTAGGTT
<i>Pal-II-R</i> ^b	AACCTAAAAGTTATTGTTTGTAATACTTTTAAGTT
<i>Pal-III-F</i> ^a	TATTTTAATAACTTAAAAGT
<i>Pal-III-R</i> ^b	ATAAAAATTATTGAATTTTCA
<i>Pal-IV-F</i> ^a	TAGGTTATAATTGTTATTAGGAA
<i>Pal-IV-R</i> ^b	TTCCTAATAACAATTATAACCTA
'X'-F ^a	GATTTTTTTTTGATTTTTTTT
'X'-R ^b	AAAAAAATCAAAAAAATC
'A'-F ^a	TATTTTAATAACTTAAAAGT
'A'-R ^b	ACTTTTAAGTTATTAATA
'B'-F ^a	TAATAGAATAATAAGTATCACTCCTTA
'B'-R ^b	TAAAGGAGTGATACTTATTATCTATTA

^{a, b} F and R represent forward and reverse, respectively.

1.2.5 *In Silico* HigBA-DNA Docking

In silico molecular docking to examine the interaction between *Pal-III* and HigBA was performed using the High Ambiguity Driven protein-protein DOCKing algorithm (HADDOCK) (43). The 20-base pair promoter DNA was modeled using a 3D-DART server (44). Residues S57, T69, and Q72 were defined as 'active residues' based on the NMR titration results. Residues A2, C12, T13 and T14 of *Pal-III-F*, T7, T8, A9 and C19 of *Pal-III-R*, Q47, R63, and T75 of HigA were additionally designated to generate a rational interface for HTH recognition contact between the protein and DNA. Passive residues were defined automatically as the residues surrounding the active residues.

1.2.6 *In Vitro* Ribonuclease Assay

The ribonuclease activity of HigB and HigB mutants was confirmed using an RNase Alert Kit (IDT, USA). In this assay, a fluorophore is covalently attached to one end of a synthetic RNA strand and quenched by a quencher group at the other end of the synthetic RNA. If synthetic RNA containing a fluorophore-quencher pair interacts with ribonuclease, the synthetic RNA is digested, and fluorescence is detected. The released fluorophore emits fluorescence at 520 nm upon excitation at 490 nm. The RFU was observed on a SpectraMax Gemini XS microplate reader (Molecular Devices, USA).

1.2.7 Kill-and-Rescue Assay

Genes encoding HigB mutants (R68A, R73A, F90A and K92A) were amplified and cloned into pBAD33. The compatible plasmid pairs (pBAD33 and pET-21a(+)) with and without each HigB mutant and HigA were cotransformed into BL21 (DE3) competent cells and grown overnight at 37°C. The overnight cultures were diluted by 100-fold in 20 ml of fresh M9 minimal medium containing 25 µg/ml chloramphenicol and 50 µg/ml ampicillin. The bacteria were then streaked onto LB medium plates supplemented with inducer L-arabinose (0.2% w/v) or 0.5 mM IPTG. The plates were incubated overnight at 37°C before examination of the cell growth.

1.2.8 Circular Dichroism Spectroscopy

CD measurements were performed to verify the structural integrity of the HigB and HigB mutants using a Chirascan plus spectropolarimeter (Applied Photophysics, UK) at

20°C in a cell with a 1-mm light path. CD scans were performed from 260 nm to 190 nm with a 1 nm bandwidth and a scan speed of 100 nm/min. Three scans were averaged, followed by subtraction of the solvent signal.

1.2.9 Designed peptides Adding to the HigBA Complex and Antimicrobial Activity Test

Three peptides that mimicked the binding interface region between HigB and HigA were designed and purchased from AnyGen (GwangJu, South Korea). Theoretically, mimicked peptides compete with the original protein for binding, and if peptides occupy the binding site, the toxin is freely released to digest RNA, which results in the detection of fluorescence in the fluorescence quenching assay. To disrupt the binding interface between HigB and HigA and restore the toxicity of HigB, peptides were added to the HigBA complex (Table 4).

The antimicrobial activity of the mimicking peptides was evaluated by measuring their minimum inhibitory concentration (MIC) values using the serial dilution method. The activity of the peptides against gram-positive *S. pneumoniae* TIGR4 (ATCC® BAA-334™) was tested. Each bacterial strain was grown overnight in the presence of various concentrations of peptide (0.4–100 µM). The MIC was defined as the lowest peptide concentration that completely inhibited bacterial growth. Each test was conducted in duplicate. Several scrambled peptides with the same amino acid sequence as the HigB α 2 helix-mimicking peptide were also tested (Table 4).

Table 4. Peptides used to disrupt the binding interface of HigBA.

Residues (start - end)	Mimicked protein	Mimicked region
SRIKLNKINDYIELL (31-45)	HigB	$\alpha 2$
DINLLSENIKYIRKL (31-45 scrambled)		
ENKIKLDRLISNYLI (31-45 scrambled)		
IKDILYSNLRIKLEN (31-45 scrambled)		
IYLLLEIDINLKSKRN (31-45 scrambled)		
KLKIISLEIDNYNRL (31-45 scrambled)		
LNLISLKREDKYNII (31-45 scrambled)		
LYNRIKIELSLNDIK (31-45 scrambled)		
SINRDKKELYILLNI (31-45 scrambled)		
YLRKNNSKELLIIDI (31-45 scrambled)		
YSLINRIDLIKEKNL (31-45 scrambled)		
SNWKDVRAELF (8-18)	HigA	$\alpha 1$
EEILESDMRVAIMSELIE (21-38)	HigA	$\alpha 2$

1.2.10 *In Vivo* Cell Growth Assay

For the cell growth assay, *S. pneumoniae* TIGR4 was grown for 10 h without agitation at 310 K in Todd Hewitt Broth (THB) in air containing 5% CO₂ until the mid-exponential phase (OD₆₀₀ of 0.5). The 10 h cultures were inoculated into fresh medium for assays. The cells were incubated at 37°C for 10 h, and growth was monitored at 1 h intervals. The average OD₆₀₀ values, along with the standard error of the mean, were plotted in MicroCal Origin software.

1.2.11 Generation of *S. pneumoniae* D39 Containing Mutated HigBA

For the electroporation experiments, *S. pneumoniae* D39 cells were grown at 37°C in THB until the early-exponential phase (OD₆₀₀ of 0.1–0.2). They were harvested and washed twice using electroporation medium containing 0.5 M sucrose, 7 mM potassium phosphate, pH 7.5, and 1 mM MgCl₂. Subsequently, they were concentrated ten times in the same medium mentioned above. Then, 0.1 ml of the concentrated cell suspension was poured into a Bio-Rad cuvette along with 1 µg/ml plasmid DNA. The mixture was incubated on ice for 10 min. A single impulse of current was supplied with the gene pulse apparatus set at 6.25 kV and 25 µF. The electro-transformed cells were then incubated at 37°C with constant shaking for approximately 1 h. Finally, the desired cells were obtained using selective media.

1.2.12 Flow Cytometry and Confocal Microscopy

S. pneumoniae TIGR4 cells were cultured in a 96-well flat bottom plate containing THB (MBcell) with various concentrations of peptide using a serial dilution method. At two time points (1 h later and 10 h later), bacteria cells were harvested and stained with a LIVE/DEAD BacLight Kit (Thermo Fisher Scientific, USA) containing SYTO[®] 9 and PI. A positive control was prepared by measuring fresh cells, and a negative control was prepared by incubating cells with 70% iso-propyl alcohol for 15 min before washing. For staining, the cells were incubated with 5 µM SYTO[®] 9 and 30 µM PI at room temperature and protected from light for 15 min. The cells were analyzed with an LSRFortessa cell analyzer (BD Bioscience, USA), and the data were analyzed using FlowJo software

(TreeStar, USA). *S. pneumoniae* D39 cells and four active-site mutants containing *S. pneumoniae* D39 cells were subjected to the same treatment used for the *S. pneumoniae* TIGR4 cells after 10 h of incubation with peptides.

S. pneumoniae cells were cultured in THB during exponential growth (OD₆₀₀ between 0.4 and 0.6). The cells were diluted with Difco™ Mueller Hinton Broth (BD Bioscience, USA) to obtain a 10% cell suspension. The cell suspension was incubated with 1 μM peptide samples conjugated with fluorescein for 30 min, and then, to remove the peptides bound to the cell surface, 1 mg/ml trypsin from bovine pancreas (Sigma Life Sciences, USA) was added for quenching. After 30 min, the cells were washed with PBS and then analyzed with a Leica TCS SP8 (Leica Microsystems, Germany) confocal microscope.

1.3 Results

1.3.1 Overall Structure of the HigBA Complex

The asymmetric unit of the HigBA complex structure is a heterotetramer containing two HigB toxins and two HigA antitoxins (Protein Data Bank (PDB) code 6AF4) (Figure 3A and Figure 4A–D). A secondary structural analysis was conducted using the 2Struc server (45). The oligomeric state of HigBA was determined to be a heterotetramer based on a molecular weight comparison with various reference proteins (Figure 5).

The *S. pneumoniae* HigB toxin contains three α -helices, one 3_{10} -helix (η) and five β -strands in the following order: β 1 (residues 4–7), α 1 (residues 15–25), α 2 (residues 29–

48), η 1 (residues 49–52), β 2 (residues 57–61), β 3 (residues 64–67), β 4 (residues 72–78), β 5 (residues 84–91), and α 3 (residues 99–115). The *S. pneumoniae* HigA antitoxin contains five α -helices and two β -strands in the following order: β 1 (residues 6–9), α 1 (residues 10–17), α 2 (residues 20–42), α 3 (residues 47–54), α 4 (residues 58–66), α 5 (residues 73–83), and β 2 (residues 85–91). The β -strands of HigB (β 1– β 5) form antiparallel β -sheets. The interactions of helices α 1 and α 2 of both HigB and HigA form a heterodimeric interface (Figure 3B). Helices α 3 and α 4 of the HigA antitoxin constitute the HTH DNA-binding motif (46) (Figure 3C). The N-terminal β 1-strands of both HigB and HigA form intermolecular β -sheets. Because the C-terminal β -strands of proximal HigAs bind to form a dimeric interface, two intermolecular β -sheets form at both the N- and C-termini of HigA (Figure 3A).

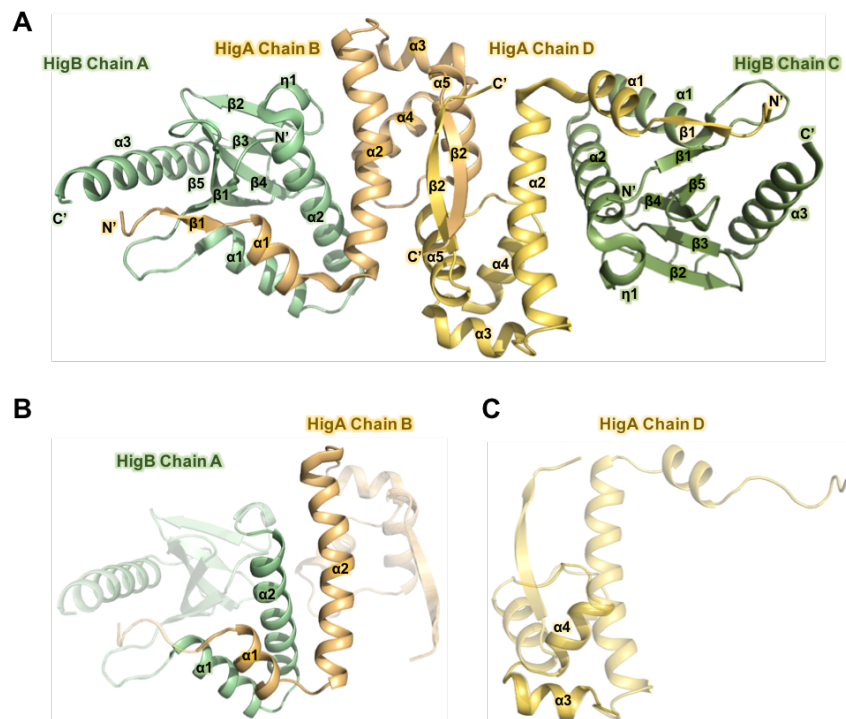


Figure 3. Overall structure of heterotetrameric *S. pneumoniae* HigBA. PyMOL was used to generate Figure 3. **(A)** ribbon representation of the HigBA heterotetramer. Chains A and C of HigB are shown in green and olive, respectively. Chains B and D of HigA are shown in orange and yellow, respectively. The structure reveals a dimeric interface between the C-terminal β -strands of the HigA subunits. The β -strands of HigB ($\beta 1$ - $\beta 5$) form antiparallel β sheets. **(B)** Binding conformation of the HigBA complex. Interactions between the N-terminal helices of both HigB and HigA result in a crossed-scissor conformation at the heterodimeric interface. **(C)** HTH DNA-binding motif consisting of $\alpha 3$ and $\alpha 4$ of HigA.

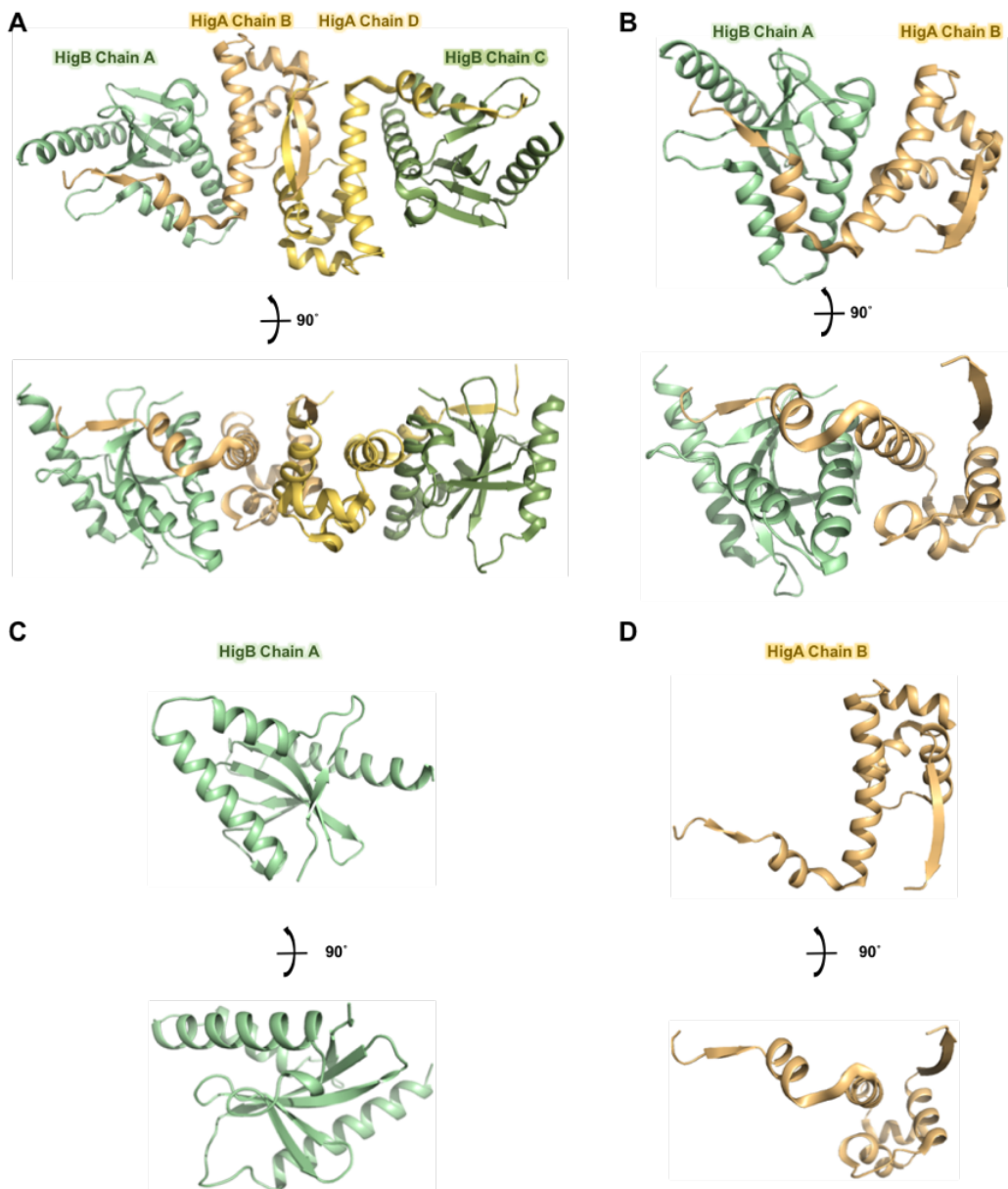


Figure 4. Ribbon representation and 90°-rotated diagrams of (A) HigBA heterotetramer, (B) HigBA dimer, (C) HigB and (D) HigA.

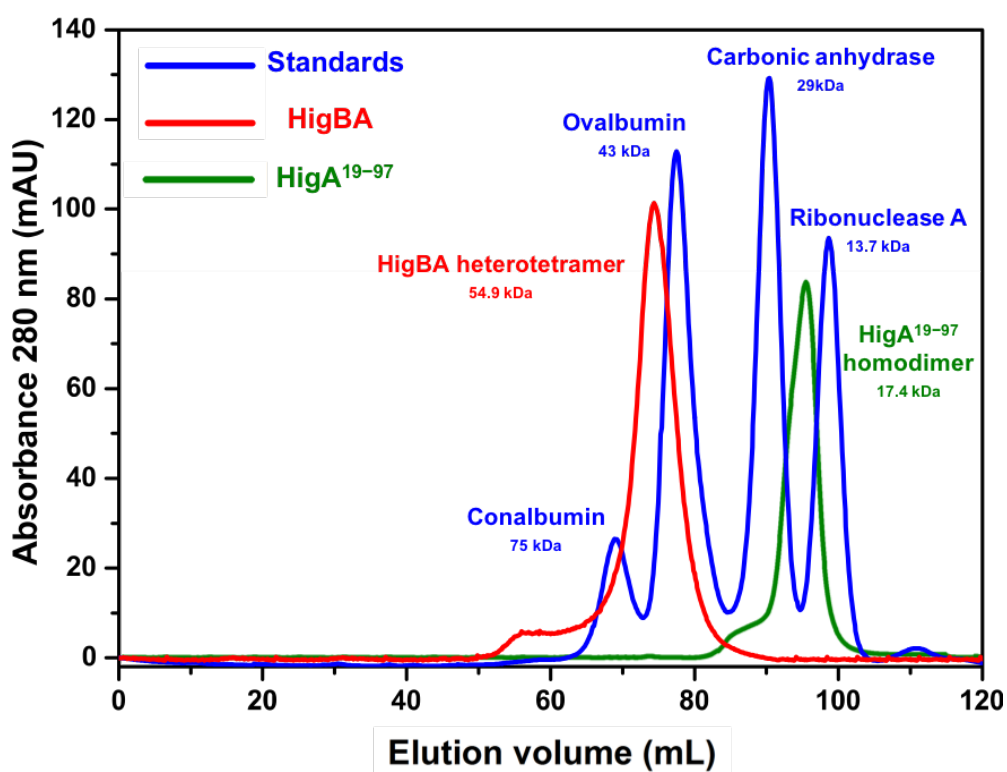


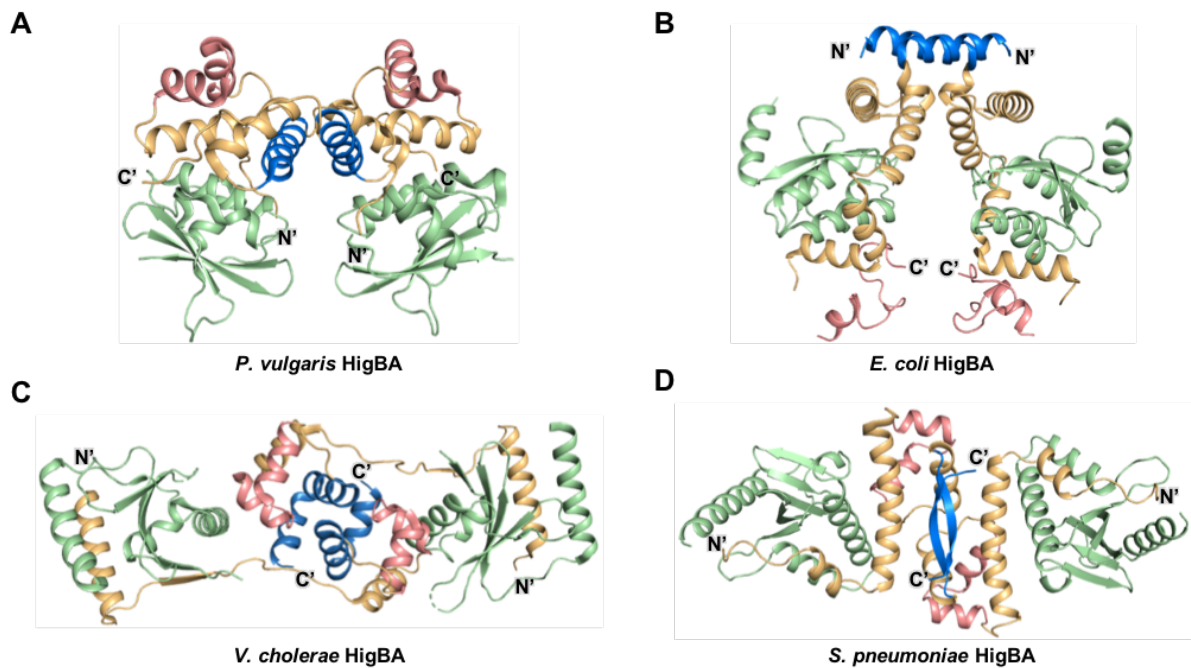
Figure 5. Molecular weight estimates of HigBA and HigA¹⁹⁻⁹⁷ obtained by size-exclusion chromatography. Each sample was fractionated on a Superdex 200 pg size-exclusion column. Chromatograms were overlaid and are displayed with molecular weight calibration standards, which are indicated as follows: 75 kDa, 43 kDa, 29 kDa and 13.7 kDa. The overlay shows that the molecular weight of HigBA is between 43 kDa and 75 kDa. The molecular weight of heterotetrameric HigBA (54.9 kDa) is in this range. The overlay also shows that the molecular weight of HigA¹⁹⁻⁹⁷ is between 13.7 kDa and 29 kDa. The molecular weight of homodimeric HigA¹⁹⁻⁹⁷ (17.4 kDa) is in this range.

1.3.2 Structural comparison of HigBA Structures

The three previously reported structures of HigBA from *Proteus vulgaris* (31) (PDB code 4MCT) (Figure 6A), *Escherichia coli* (PDB code 5IFG) (Figure 6B) (32) and *Vibrio cholera* (PDB code 5JAA) (Figure 6C) (30) were compared with the newly obtained structure of HigBA from *S. pneumoniae* (PDB code 6AF4) (Figure 6D). These four structures share the features that each HigB has antiparallel β -sheets as its main functional unit and each HigA contains an HTH DNA-binding motif. They form a heterotetrameric assembly, and dimerization is achieved only through the HigAs [HigB-(HigA)₂-HigB].

However, significant differences occur in the complex structures, the interface between HigB and HigA, the conformation of the HigA dimer, and the position of the DNA-binding motif of HigA are quite different from each other.

HigAs from *E. coli* and *S. pneumoniae* wrap the cognate HigB with their two helices. HigA from *V. cholerae* wraps its cognate HigB, with one α -helix and one β -strand. However, two helices from *P. vulgaris* HigA form boundary junctions with two helices from its cognate HigB. The dimerization domains of HigAs are also quite different from each other. In *P. vulgaris* and *E. coli*, one helix is involved in dimerization, and in *V. cholerae*, two helices are packed to form a dimerization domain. In contrast, in *S. pneumoniae*, an antiparallel β sheet is formed between the C-termini of the two subunits. The HTH motif of *P. vulgaris* HigA is located at the N-terminus, while the motif of *E. coli* HigBA is at the C-terminus. In *V. cholerae* and *S. pneumoniae* HigA, the HTH motif occurs in the middle of the proteins. To understand the differences among HigBAs, a full-length sequence comparison and the resulting amino acid identity percentages are presented in figure 7. Alignments of amino acid residues were carried out using ClustalW (47) and visualized using ESPrpt 3.0 (48).



HigBA from bacterial species	HigBA binding interface	HigA dimerization architecture	Location of HTH domain
<i>P. vulgaris</i> (PDB code 4MCT)	Boundary junction by helices	One helix	N-terminal $\alpha 1$ - $\alpha 2$
<i>E. coli</i> (PDB code 5IFG)	Wrapping (two helices)	One helix	C-terminus
<i>V. cholerae</i> (PDB code 5JAA)	Wrapping (one helix and one strand)	Two helices	C-terminal $\alpha 3$ - $\alpha 4$
<i>S. pneumoniae</i> (PDB code 6AF4)	Wrapping (two helices)	Antiparallel β sheets	C-terminal $\alpha 3$ - $\alpha 4$

Figure 6. Ribbon representation of the HigBA structures. HigBs and HigAs are shown in green and orange, respectively. HigA dimerization domains are shown in blue, and HigA HTH DNA-binding domains are shown in red. Structural information is summarized in the table. The N terminus and C terminus of each HigA are also indicated. PyMOL was used to generate Figure 6. **(A)** HigBA from *P. vulgaris*. **(B)** HigBA from *E. coli*. **(C)** HigBA from *V. cholerae*. **(D)** HigBA from *S. pneumoniae*

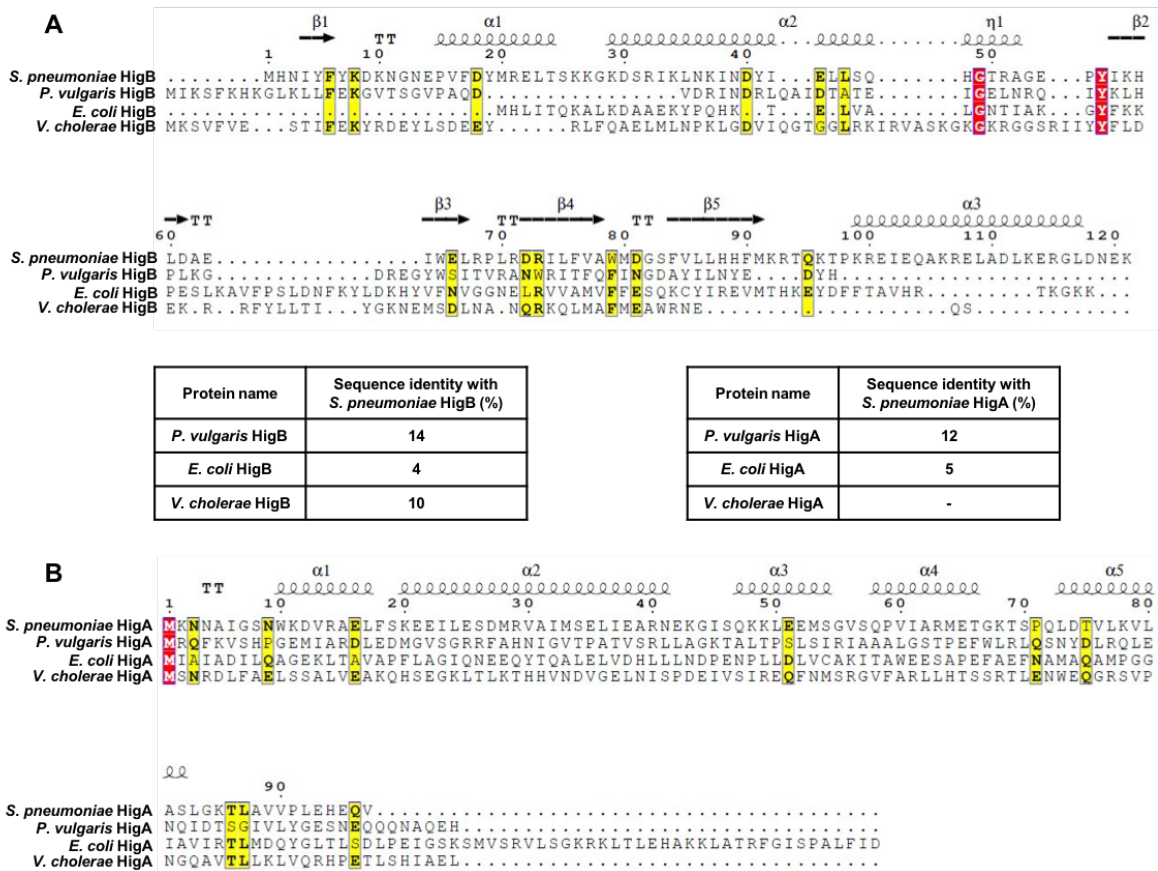


Figure 7. Full-length sequence comparison and percentages of amino acid identities of (A) HigBs and (B) HigAs. Structural information of *S. pneumoniae* HigBA was used as the top secondary structures, and the description and sequence numbering on the topside correspond to *S. pneumoniae* HigBA. Residues showing similarity are highlighted in red and yellow.

1.3.3 DNA-Binding Properties of HigBA

To confirm the DNA-binding properties of HigBA and HigA, an electrophoretic mobility shift assay (EMSA) experiment was conducted using the four palindromic DNAs of the HigBA upstream region (*Pal-I, II, III* and *IV*) (Figure 8A). The palindromic DNAs exhibited a conserved sequence represented as xaxxt(...)axxaa. In the EMSA experiment, the DNA concentration was fixed at 0.01 mM and the protein concentration was increased from 0 to 0.6 mM (HigA dimer and HigBA hetero-tetramer). As the amount of added protein increased, the bands of the DNA-protein complex shifted upward,

showing that HigBA binds to all four DNAs (*Pal-I, II, III* and *IV*) (Figure 8B). In the EMSA results, two complexes showing distinct mobility were observed. I surmised that HigBA binds to DNA, which results in the formation of a lower-shifted band. However, because the DNA sequences are relatively long (at least 20mer), two HigBA heterotetramers might be able to bind to one DNA. Therefore, an increase in the fraction of the super-shifted band likely occurred at higher concentrations of HigBA. HigBA showed the highest affinity for *Pal-III* among the four DNAs. To confirm the binding specificity of HigBA to its upstream promoter, an EMSA experiment was also conducted using the other two palindromic sequences 'A' and 'B', which did not belong to the promoter region of HigBA. The results showed that band shifts did not occur in the cases of 'A' and 'B' or the control DNA 'X', indicating a lack of DNA-protein complex formation between the proteins and DNA (Figure 9). An isothermal titration calorimetry (ITC) experiment was performed to estimate the binding affinity of HigBA (Figure 8C). The DNA-binding reaction of HigBA is endothermic and entropically driven, and the thermodynamic parameters are listed in Table 5. The binding stoichiometry (n) indicates that one HigBA heterotetramer binds to each DNA duplex. The thermodynamic parameters of HigA are provided in Figure 10. The experimental results showed that the HigBA complex has a higher affinity for DNA than the HigA complex based on the K_d values. Calorimetric trials were also performed in the absence of proteins under the same experimental conditions. No changes in heat were observed in the control experiments using a protein-free buffer. In addition, no thermal changes were observed in the experimental injections of control DNA 'X' or those with the palindromic sequences 'A' and 'B'.

To determine the DNA-binding site of HigA, a NMR titration experiment on HigA was conducted with *Pal-III* DNA, which had the highest affinity with HigA. Because of

the poor quality of the spectrum of full-length HigA (Figure 11A), HigA¹⁹⁻⁹⁷ was used for this experiment. The 63 N-H peaks in the ¹H-¹⁵N heteronuclear single quantum coherence spectroscopy (HSQC) spectra were assigned to individual residues of HigA¹⁹⁻⁹⁷ (Figure 11B). The oligomeric state of the deletion mutant HigA¹⁹⁻⁹⁷ was determined to be a homodimer and showed an unchanged binding mode (Figure 5). Then, the HSQC spectra of HigA¹⁹⁻⁹⁷ (0.5 mM) with increasing concentrations of *Pal-III* (0 to 0.1 mM) were overlaid (Figure 12A). The ¹H-¹⁵N HSQC peaks of HigA showed no significant chemical shift changes with decreased intensity as illustrated in Figure 12B. The intensity reduction and disappearance of the ¹H-¹⁵N HSQC cross-peak of HigA may originate from the increased transverse relaxation rate of HigA¹⁹⁻²⁷ by complex formation with *Pal-III* DNA. Although small chemical shift changes were observed, S34, T69, Q72 and A88 showed relatively distinct chemical shift changes compared with the other residues (Figure 12B) as well as large intensity reductions. Although the overall cross-peaks exhibited intensity reduction, the largest effects for ¹H-¹⁵N HSQC cross-peak intensity reduction were found in helices α_3 , α_4 , and α_5 and their connecting loops. Helices α_3 and α_4 form the HTH motif, which is strongly related to DNA binding. In addition, α_5 and its connecting loop are close to the HTH motif.

Based on these results, the binding pattern between DNA and HigBA was deduced by HADDOCK. Multiple solutions of the *in silico* docking model of the HigBA-DNA complex were clustered automatically to obtain the best single cluster of docking results. The best solution showed a score of -207.9 ± 2.7 , the smallest root mean square deviation (RMSD) ($2.2 \text{ \AA} \pm 0.3 \text{ \AA}$), and the largest buried surface area ($2458.2 \pm 38.0 \text{ \AA}^2$) (Figure 12C). Helices α_3 and α_4 of HigA constituting the HTH motif bind mainly to the major

groove of the DNA. In the electrostatically generated interface, $\alpha 3$ exhibited a negative charge while $\alpha 4$ exhibited a positive charge.

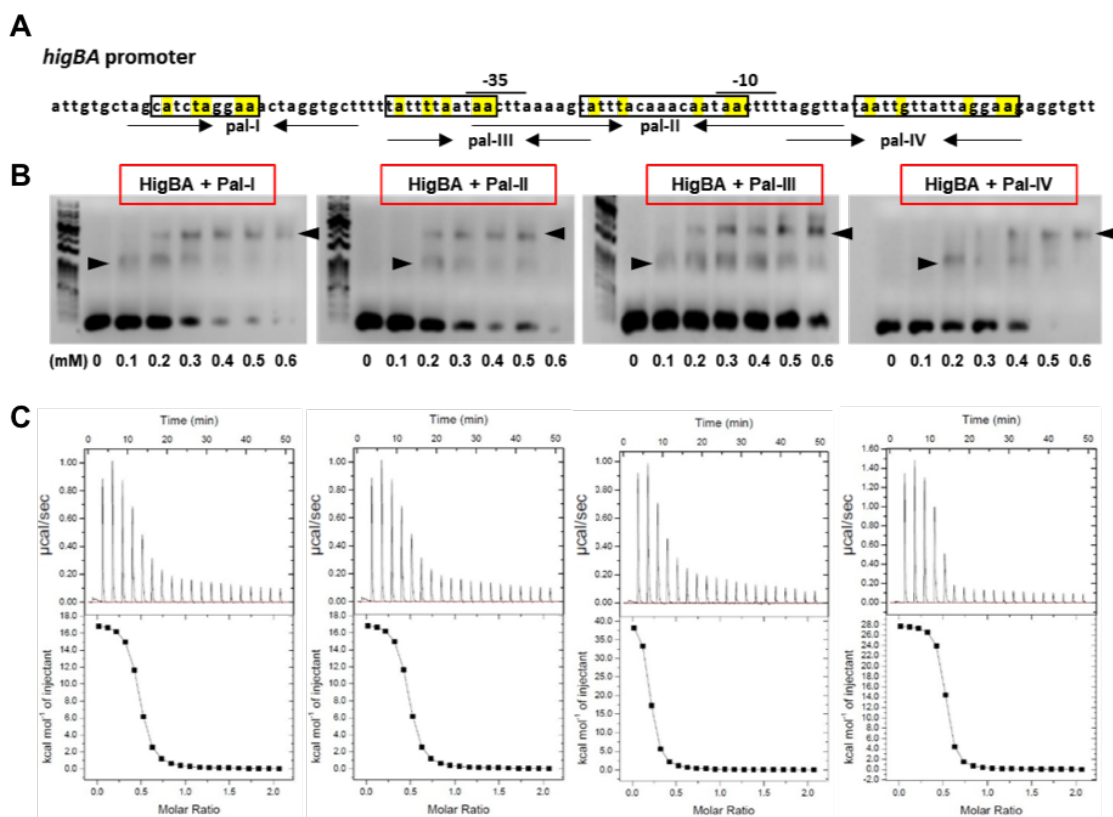


Figure 8. Electrophoretic mobility shift assay and ITC results with palindromes in the *higBA* promoter region. **(A)** *higBA* promoter region. The putative 10 box and 35 box are denoted. The palindromic sequences *Pal-I*, *Pal-II*, *Pal-III*, and *Pal-IV* are shown by arrows facing each other. Consensus recognition sequences are boxed, and identical sequences are highlighted as yellow. **(B)** EMSAs demonstrated that increasing concentrations of the HigBA complex bound to the four palindromes. Shifted bands are indicated with arrowheads. Each reaction mixtures (10 μ L) contained 0.01 mM DNA duplex. Shown data are representative of three independent experiments. **(C)** ITC assay of four palindromes to which the HigBA complex bound. The binding parameters are described in Table 5

Table 5. Thermodynamic parameters upon binding of DNA to HigBA.

DNA	<i>n</i> (the binding stoichiometry)	K_d (μ M)	ΔH (kcal mol^{-1})	$T\Delta S$ (kcal mol^{-1})	ΔG (kcal mol^{-1})
<i>Pal-I</i>	0.53 ± 0.07	0.46 ± 0.03	2.8 ± 0.4	8.74	-5.94
<i>Pal-II</i>	0.49 ± 0.06	0.70 ± 0.08	3.6 ± 0.3	7.37	-3.77
<i>Pal-III</i>	0.48 ± 0.04	0.20 ± 0.01	1.7 ± 0.2	8.14	-6.44
<i>Pal-IV</i>	0.48 ± 0.05	1.19 ± 0.14	4.3 ± 0.3	9.73	-5.43

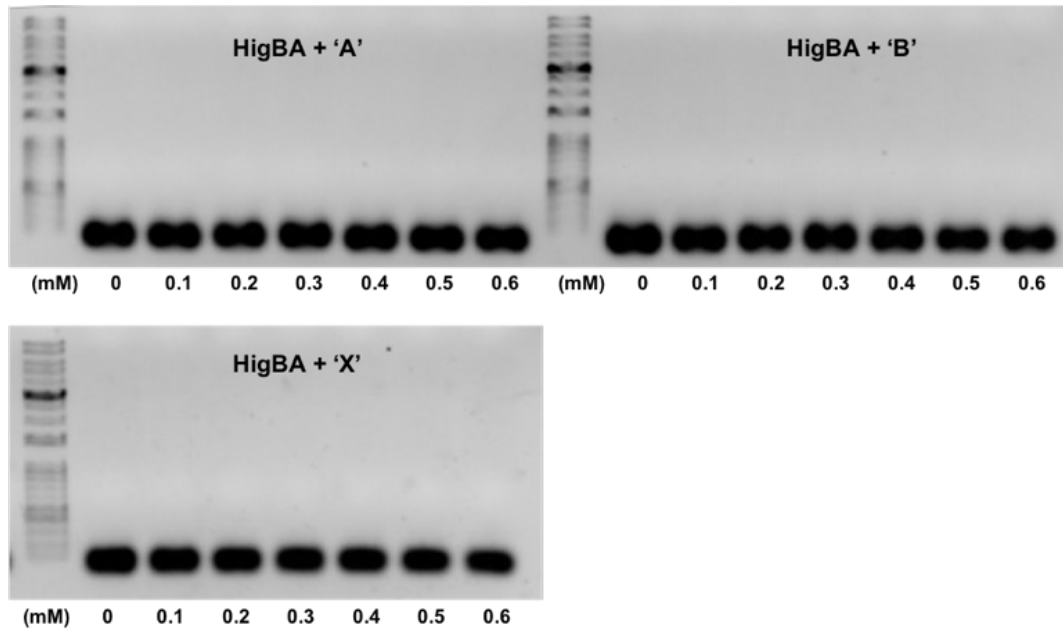
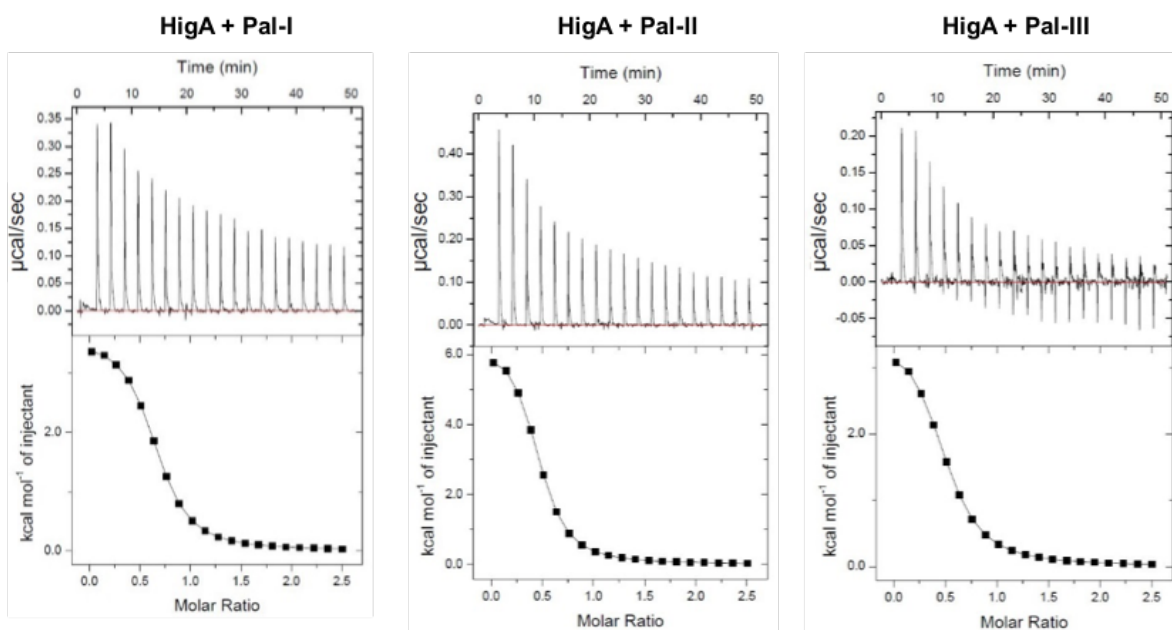


Figure 9. EMSA study using other palindromic sequences 'A' and 'B' and control DNA 'X'. Upper left: EMSA experiment testing the binding of HigBA to 'A'. Upper right: EMSA experiment testing the binding of HigBA to 'B'. Lower: EMSA experiment testing the binding of HigBA to DNA 'X'. Each DNA concentration was 0.01 mM, and protein concentrations are indicated in each lane.



DNA	n (the binding stoichiometry)	K_d (μM)	ΔH (kcal mol^{-1})	$T\Delta S$ (kcal mol^{-1})	ΔG (kcal mol^{-1})
Pal-I	0.53 ± 0.04	1.61 ± 0.02	6.4 ± 0.5	8.79	-2.39
Pal-II	0.51 ± 0.02	2.53 ± 0.11	6.5 ± 0.3	7.53	-1.03
Pal-III	0.50 ± 0.04	1.34 ± 0.01	5.7 ± 0.4	12.5	-6.80

Figure 10. ITC results with palindromes in the *higBA* promoter region. ITC assay of the binding of three palindromes (*Pal-I*, *Pal-II* and *Pal-III*) to HigA antitoxin. The binding parameters are described in the table (lower).

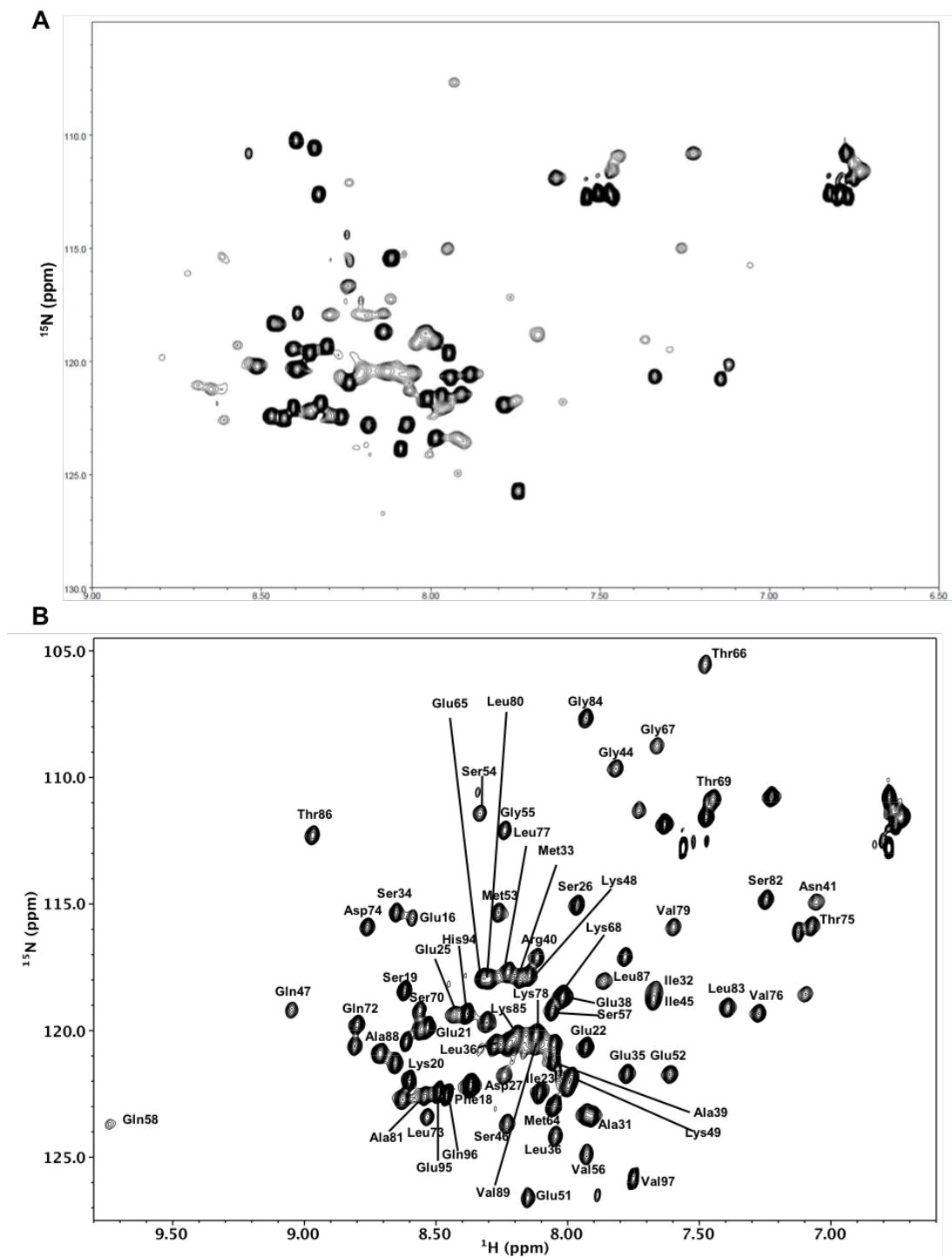


Figure 11. 2D ^1H - ^{15}N HSQC spectra of full-length HigA and HigA¹⁹⁻⁹⁷. (A) 2D ^1H - ^{15}N HSQC spectrum of full-length HigA. The peaks of the full-length spectrum of HigA could not be assigned. (B) 2D ^1H - ^{15}N HSQC spectrum of HigA¹⁹⁻⁹⁷. The assigned residues are indicated in the spectrum.

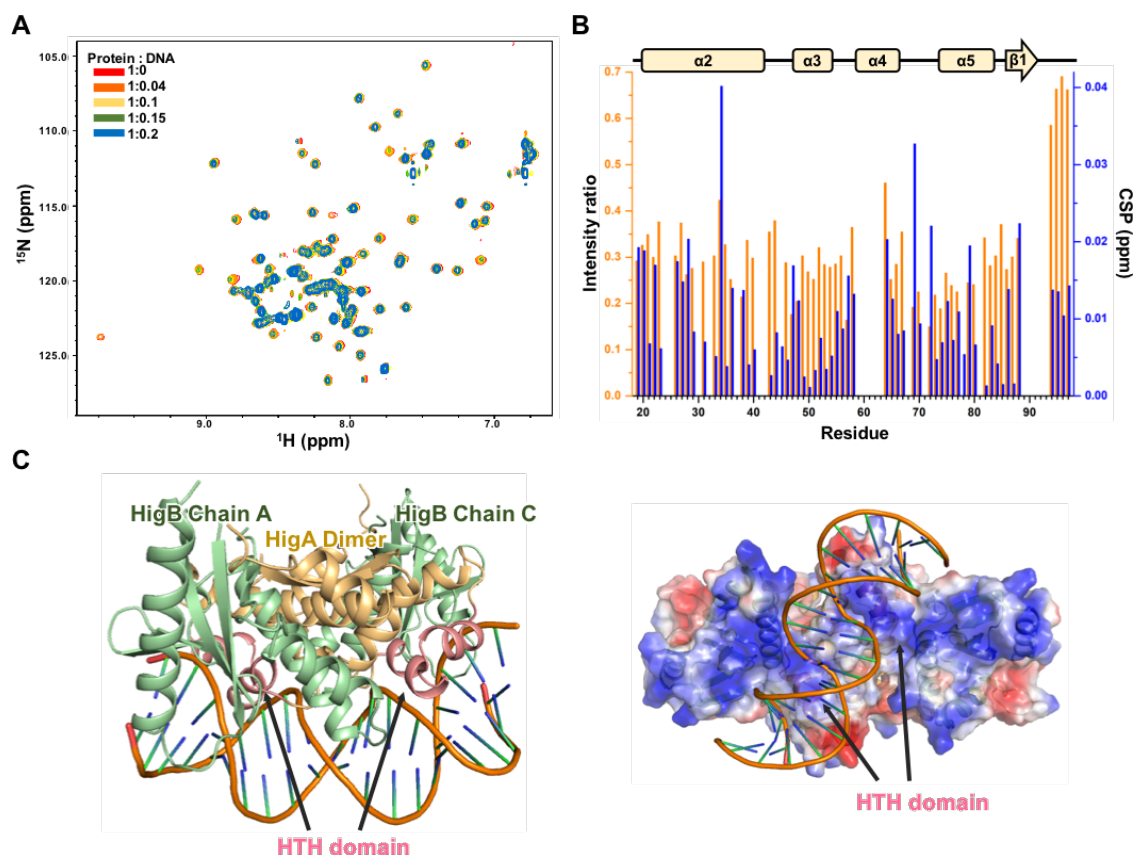


Figure 12. DNA-binding properties determined from NMR titration data and *in silico* docking model of the HigBA-DNA complex. **(A)** NMR titration of HigA19-97 with *Pal-III* DNA. 2D-1H, 15N HSQC spectra of HigA19-97 (0.5 mM) acquired at varying *Pal-III* DNA concentrations (0 to 0.1 mM) are overlaid. The ratios and color coding are shown in the figure. **(B)** Intensity ratio (orange columns) and CSP value (blue columns) plotted against the residue number. **(C)** *In silico* docking model of the HigBA-DNA complex (left) with the electrostatic potential surface (right). HTH DNA-binding domains of HigA are shown in red. PyMOL was used to generate Figure 12C.

1.3.4 Active Site of HigB Deduced from Homologs

HigB toxins contain several conserved active site residues that are essential for the cleavage of mRNA. For a detailed comparison of *S. pneumoniae* HigB (Figure 13A and E) with other HigBs, the structural similarities of HigBs were analyzed using Dali (49), and the reported active site residues were arranged. Despite low statistical similarity, the active sites of HigBs were found to be located in their antiparallel β -sheets. The detailed Dali search results with HigB from *Vibrio cholera* (30) (Figure 13B), HigB from *E. coli*

(32) (Figure 13C) and HigB from *Proteus vulgaris* (31) (Figure 13D) are shown in Table 6. According to the structural alignment, the putative active residues of *S. pneumoniae* HigB for ribonuclease activity may be D61, E66, R68, R73, F90 and K92. Compared with other HigBs, the active site residues of *S. pneumoniae* HigB are sterically hindered by a flexible loop between $\beta 5$ and $\alpha 3$.

In addition, the overall structures of ribonucleases from similar families were compared using Dali, which showed high statistical values for ParE from *Mesorhizobium opportunistum* (50) (Figure 13F), RelE from *Pyrococcus horikoshii* (51) (Figure 13G), and YoeB from *E. coli* (52) (Figure 13H) (Table 7). These ribonucleases showed significant structural similarity despite their low sequence identity. The C-terminal α -helix in *S. pneumoniae* HigB is not conserved in other structural homologs.

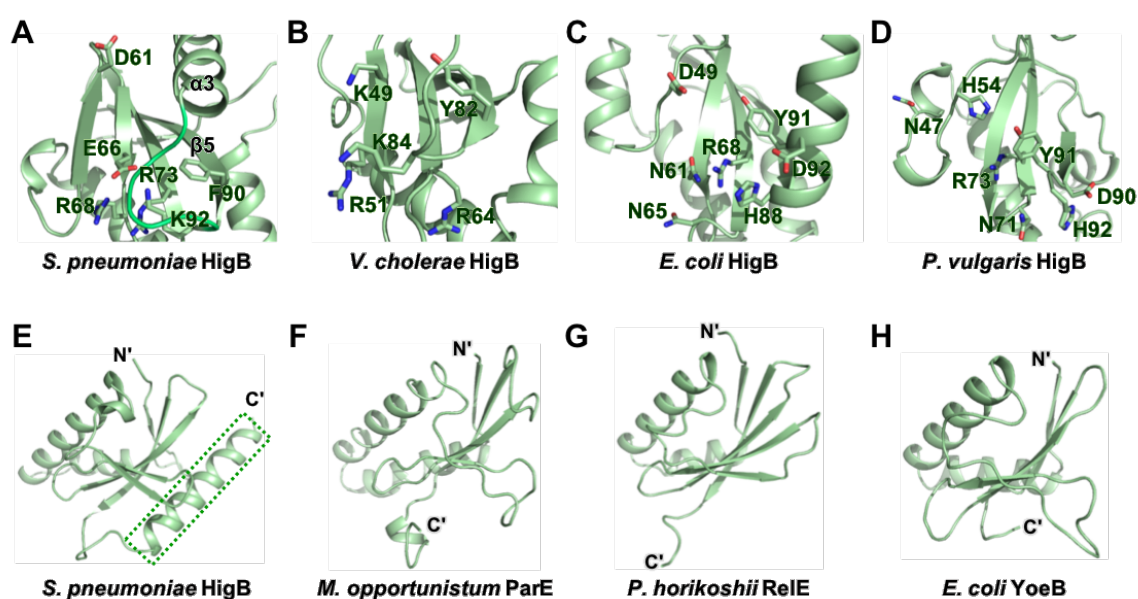


Figure 13. Active site residues of *S. pneumoniae* HigB compared to those of other HigBs, and overall structures of ribonucleases from similar families. PyMOL was used to generate Figure 13. (A–D) Active site residues of *S. pneumoniae* HigB compared to those of other HigBs. The HigB active site residues of (A) *S. pneumoniae*, (B) *V. cholerae*, (C) *E. coli*, and (D) *P. vulgaris*. The active sites of HigBs are oriented to show the antiparallel β -sheets in frontal view. (E–H) Overall structures of ribonucleases from similar families. The C-terminal α -helix observed only in *S. pneumoniae* HigB is highlighted in a green dashed box. (E) *S. pneumoniae* HigB, (F) *M. opportunistum* ParE, (G) *P. horikoshii* RelE, and (H) *E. coli* YoeB

Table 6. Structural similarity comparison of HigB with its homologs using the Dali server.

Protein name	Source	PDB code (used chain)	Z-score	RMSD (Å)	Number of aligned Ca	Sequence identity (%)
HigB	<i>V. cholera</i>	5JAA (D)	6.8	3.6	87	10
HigB	<i>E. coli</i>	5IFG (A)	6.9	2.9	83	4
HigB	<i>P. vulgaris</i>	4MCT (D)	6.4	2.7	77	14

Table 7. Structural similarity comparison of HigB with its homologs using the Dali server.

Protein name	Source	PDB code (used chain)	Z-score	RMSD (Å)	Number of aligned Ca	Sequence identity (%)
ParE	<i>M. opportunistum</i>	5CEG (D)	9.8	2.4	86	3
RelE	<i>P. horikoshii</i>	1WMI (A)	9.8	1.8	80	11
YoeB	<i>E. coli</i>	2A6R (D)	9.8	2.0	79	16

1.3.5 Intermolecular Interaction of HigBA

Substantial intermolecular networks between HigB and HigA are formed at the cross-scissor interface. Helices $\alpha 1$ and $\alpha 2$ of both HigB and HigA underwent hydrophilic and hydrophobic interactions to form binding interfaces. In the interface, the residues of HigB involved in hydrophilic interactions are R21, R32, N39, D40, E43 and H48, and they interact with W10, R14, E16, E22, S26, R29 and S34 of HigA. D40 of HigB has the closest interactions with S26 and R29 of HigA (Figure 14A). Hydrophobic interactions are contributed by F17, M20, L35, Y41, I42 and L44 of HigB and by W10, V13, L17, F18, V30 and M33 of HigA. F17, M20 and L44 of HigB have hydrophobic interactions with multiple counterparts (Figure 14B). These binding networks are summarized in Figure 14A and B.

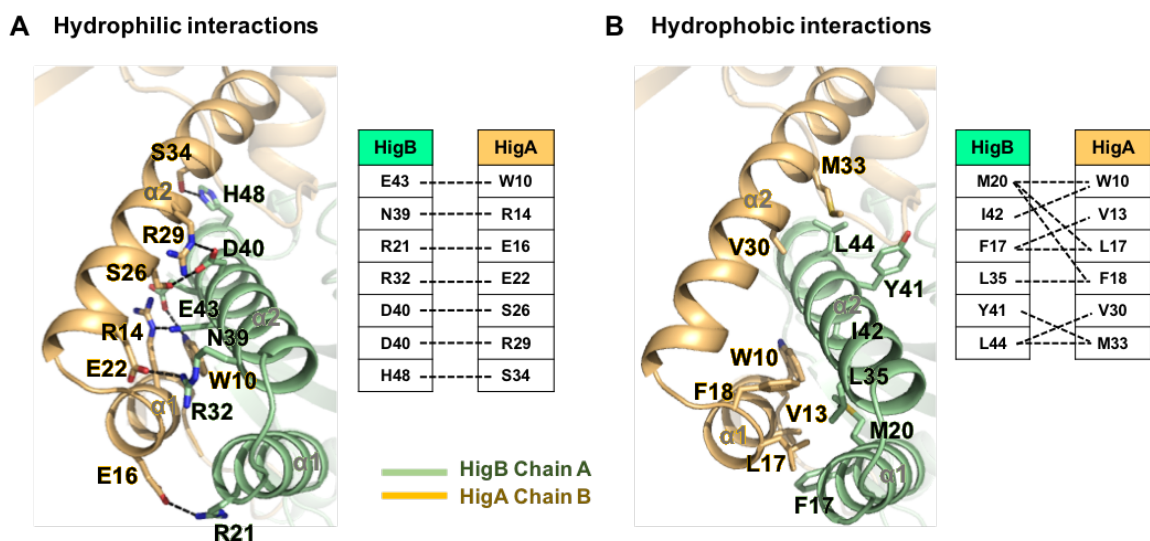


Figure 14. Crossed-scissor heterodimeric interface between HigB and HigA. The same colors as in Figure 3 are employed. PyMOL was used to generate Figure 14. **(A)** Residues involved in hydrophilic interactions at the interface. Hydrogen bonds and salt bridges are shown as black dotted lines. The residues participating in hydrophilic interactions are also shown in stick representation. **(B)** Residues involved in hydrophobic interactions at the interface. The residues participating in hydrophobic interactions are also shown in stick models. **(A,B)** Schematic diagrams of the hydrophilic interactions (left) and hydrophobic interactions (right) contributed by residues in the heterodimeric interface of HigBA

1.3.6 Ribonuclease Activities of HigB and Its Mutants

Ribonuclease activity assays on HigB were performed using fluorescence-labeled RNA substrates. When the substrates are cleaved, fluorescence is emitted in proportion to the amount of the substrate cleaved by HigB. The ribonuclease activity of *S. pneumoniae* HigB is confirmed through the increase in resulting fluorescence (RFU) as a function of time and concentration (Figure 15A). The control containing only RNA substrate without proteins showed no ribonuclease activity.

In addition, to determining the mutation effects of active site residues and the main residues interacting with HigA, ribonuclease activity was also measured for a total of 10 single amino acid mutants (mutations in active site residues D61A, E66A, R68A, R73A, F90A and K92A and HigA-interacting residues D40A, M20A, F17A and L44A) (Figure

15B). R73A showed approximately 70% less ribonuclease activity than the wild-type (WT) HigB, and F90A and R68A also showed significant reductions in ribonuclease activity. The mutation effect of K92 (K92A) was relatively reduced, and the mutations of D61, E66 and the HigA-interacting residues had almost negligible effects on ribonuclease activity. The secondary structural integrity of HigB and the HigB mutants was verified by circular dichroism (CD) spectroscopy (Figure 16A).

Based on these *in vitro* results, four efficient mutants (R68A, R73A, F90A and K92A) showing significant reductions in ribonuclease activity were validated through an *in vivo* toxicity neutralization test. To perform this kill-and-rescue assay using *E. coli*, HigB and its mutants were cloned into the L-arabinose inducible vector pBAD33 and HigA was cloned into the IPTG inducible vector pET-21a(+). As expected from the *in vitro* test results, the toxicity of HigB was efficiently rescued by HigA and HigB mutations of residues R68, R73 and F90. The K92A mutant exhibited slightly weak toxicity compared to the WT HigB, showing that the toxicity of HigB was not strongly affected by the mutation of K92 compared to mutations of the other residues (R68, R73 and F90) (Figure 17). This assay demonstrated that HigB is a *bona fide* toxin with cytotoxicity and that the active site of HigB has been successfully deduced.

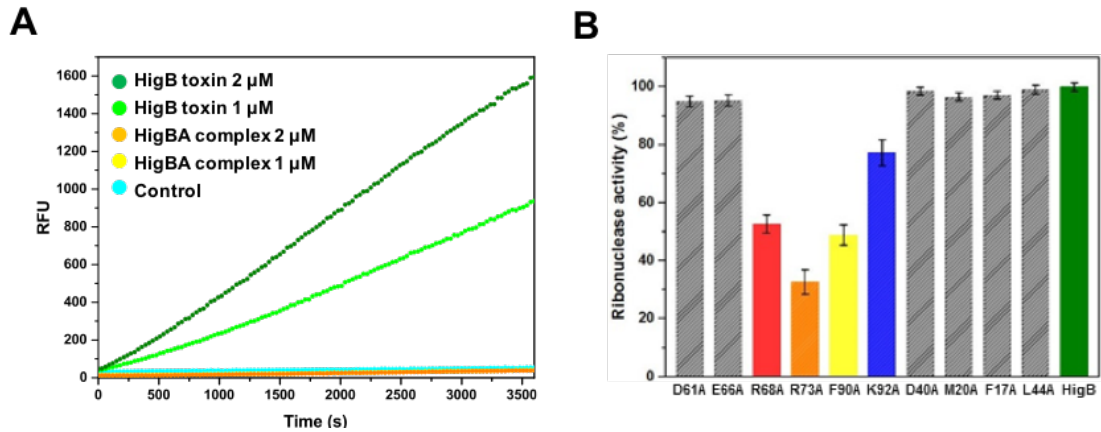


Figure 15. *In vitro* ribonuclease activity assays of *S. pneumoniae* HigB with its mutants. Each experiment was performed in triplicate. **(A,B)** *In vitro* ribonuclease activity assays of *S. pneumoniae* HigB and comparison of the ribonuclease activity with that of HigB mutants. **(A)** Fluorescence measurements as a function of time. The control did not show activity, and HigB showed concentration-dependent ribonuclease activity. **(B)** Comparison of the ribonuclease activity of the WT HigB with those of the HigB mutants. A WT HigB at 2 μM was used as a reference for comparison. The concentration of each HigB mutant was the same as that of the WT HigB. The RFU obtained with the reference was taken as 100%. Arg73 of HigB showed the strongest effect on the ribonuclease activity of HigB. Error bars represent the standard deviations of the three replicate reactions

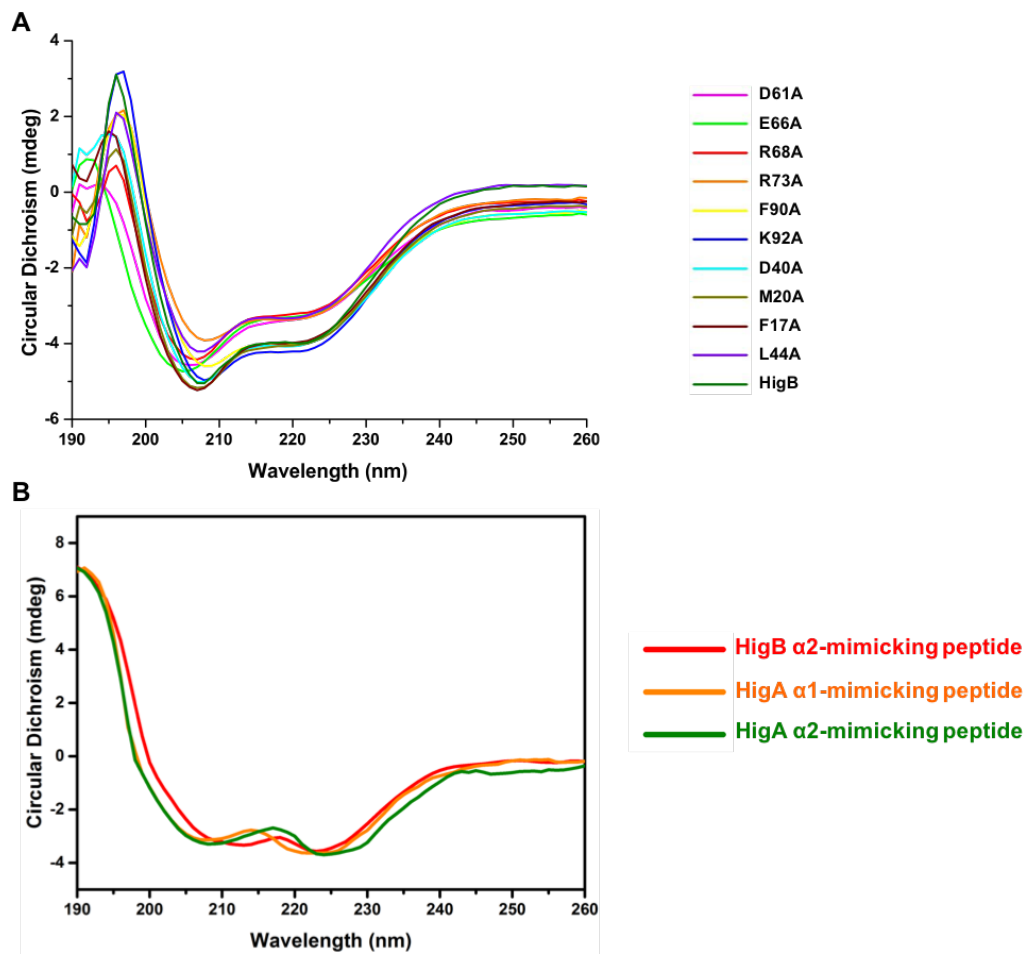


Figure 16. Validation tests for toxin mutants and peptide mimetics. **(A and B)** Circular dichroism spectra of the **(A)** HigB mutants and **(B)** mimicking peptides in 50 mM MES, pH 6.0, 500 mM NaCl. All mutants regained their secondary structure after refolding.

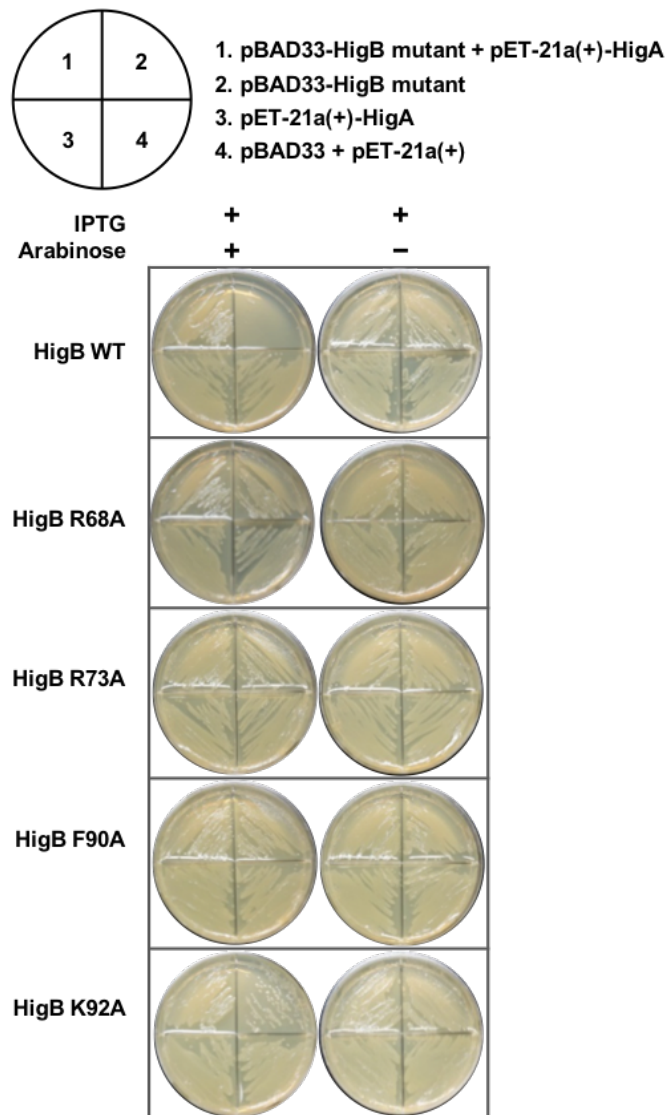


Figure 17. Toxicity and antitoxicity assay of HigB variants and their combinations with HigA in *E. coli*. Each quadrant contains the corresponding plasmids indicated above. The plate on the left contained both L-arabinose and IPTG that induced HigB (toxin) variants and HigA (antitoxin) expression, whereas the plate on the right contained IPTG that induced only antitoxin expression. The expression of plasmids encoding the WT HigB (using the pBAD33 vector) resulted in cell growth arrest; the toxicity was neutralized by coexpression of the plasmid encoding HigA (using the pET-21(a) vector). The mutations of R69, R73, and F90 reduced the activity of the HigB toxin, and the mutation of K92 slightly reduced the activity of HigB toxin (segment 2). The HigA-induced toxicity inhibition can be confirmed via good growth

1.3.7 HigBA Complex Disruption by Mimicking Peptide

Peptides mimicking the binding region between HigB and HigA were added to disrupt the HigBA complex. When the HigBA complex is disrupted by peptides and free

HigB is released, fluorescence-labeled RNA substrates emit fluorescence in proportion to the amount of the substrate cleaved by HigB. The α -helical nature of one HigB-mimicking peptide and two HigA-mimicking peptides was confirmed by CD spectroscopy (Figure 16B).

The addition of mimicking peptides resulted in the effective disruption of HigBA, showing regeneration of the toxicity of peptide-treated HigBA compared to the activity of HigB (Figure 18A). When the HigB $\alpha 2$ helix-mimicking peptide was added to HigBA, the ribonuclease activity reached approximately 80% of that of HigB. Subsequently, the complex disruption of the HigB-mimicking peptide was also verified by chromatograms using a Superdex 75 10/300 prepacked column (GE Healthcare, Chicago, IL, USA) (Figure 18B).

1.3.8 Artificial Activation of Toxin by Designed Peptides Can Exert Bactericidal Effects *In Vivo*

To support the above results in an *in vitro* enzyme-level experiment, diverse *in vivo* studies were performed. An antimicrobial activity test of the mimicking peptides against *S. pneumoniae* TIGR4 revealed that cell growth was inhibited at concentration of 6.3 μ M HigA $\alpha 1$ -, $\alpha 2$ - or HigB $\alpha 2$ -mimicking peptide. A cell growth assay of the designed peptides at 6.3 μ M showed the highest growth defects in the presence of the HigB $\alpha 2$ -mimicking peptide (Figure 18C). Scrambled peptides with the same amino acid sequence as the HigB $\alpha 2$ -mimicking peptide did not inhibit *S. pneumoniae* cell growth.

The effect of HigB $\alpha 2$ -mimicking peptide addition on *S. pneumoniae* TIGR4 cells was then tested by the flow cytometry analysis of cells labeled with LIVE/DEAD

BacLight stains (Figure 18D). In the absence of peptides, 22.1% of *S. pneumoniae* TIGR4 cells were permeable to propidium iodide (PI). In contrast, for *S. pneumoniae* TIGR4 cells treated with peptides, the proportion of PI-permeable cells increased to 78.1% in the presence of 6.3 μ M peptides after 10 h of incubation, indicating the bactericidal activity of the structure-based designed peptides. To support the suggested mode of killing, the data after 1 h incubation with peptides are provided (Figure 18E and F). The results show that most cells lived after 1 h incubation. Thus, the peptides might not have caused the loss of membrane potential and membrane barrier function.

The successful intracellular localization of peptides was also demonstrated by confocal microscopy using fluorescein-labeled peptides (Figure 18G). Fluorescein-only (left) and bright-field images of *S. pneumoniae* TIGR4 (middle) are presented. An overlaid image (right) indicates the successful intracellular localization of the peptide. Because surface-bound peptides and extracellular peptides were degraded by trypsin, the images indicate that the fluorescence signals are indeed mediated by peptide internalization. Because confocal images were taken after 1 h incubation with the peptides, the peptides were introduced much earlier than PI and peptide passage might have allowed the cytoplasmic membrane to maintain its barrier and energy generating function for quite some time after introducing the peptide.

For further proof of the suggested killing mechanism, *S. pneumoniae* D39 without *higBA* and *S. pneumoniae* D39 containing intact *higBA* or active site-mutated *higBA* were treated with 6.3 μ M peptides. After 1 h, the peptides entered the *S. pneumoniae* D39 cells containing active site-mutated *higBA*, and the results were consistent with that of *S. pneumoniae* TIGR4 (Figure 18H). However, after 10 h, *S. pneumoniae* D39s containing active site-mutated *higBA* presented longer lifespans than *S. pneumoniae* D39s containing

intact *higBA* (Figure 18I). *S. pneumoniae* D39s that did not contain *higBA* seemed to be unaffected by peptides.

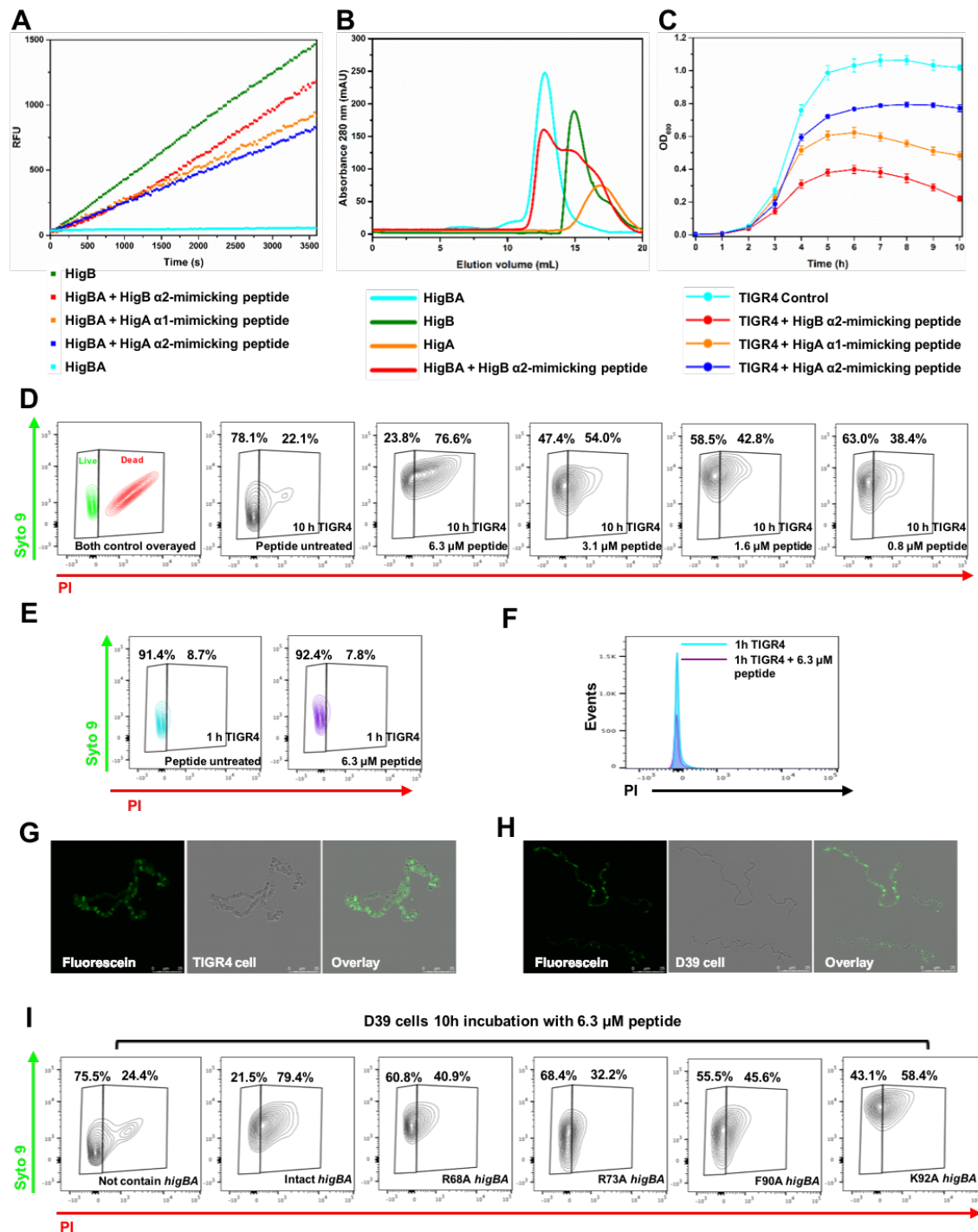


Figure 18. Protein complex disruption and subsequent *in vivo* cell feasibility assays using binding region-mimicking peptides. **(A)** *In vitro* ribonuclease activity assays using binding region-mimicking peptides. Each experiment was performed in triplicate. Each mimicking peptide (10 μ M) was added to 2 μ M HigBA. Forty units of RiboLockTM (Thermo Scientific, USA) RNase inhibitor was used to prevent ribonuclease

contamination. **(B)** Size-exclusion chromatography of HigBA, HigA, HigB, and HigB α 2 helix-mimicking peptide added. Absorption at 280 nm is plotted as a function of the elution volume. The volume of injected protein was 100 μ L, and the concentrations of proteins and HigB α 2-mimicking peptide were 200 μ M and 1 mM, respectively. **(C)** Effect of peptides on the growth of *S. pneumoniae* TIGR4 was measured based on the OD600. Error bars represent the standard error of the mean across three biological replicates. **(D–I)** Cell viability confirmation using flow cytometry and confocal imaging. **(D)** *S. pneumoniae* TIGR4 was treated with various concentrations of HigB α 2 mimicking peptide selected by the results of the MIC test. Cells were labeled with LIVE/DEAD BacLight stains (Syto 9; PI) and analyzed by fluorescence-activated cell sorting (FACS). The results of the untreated peptide cells are also presented for comparison. Live cell/dead cell areas were established using this TIGR4 control. **(E)** FACS data of 6.3 μ M peptide-treated *S. pneumoniae* TIGR4 after 1 h of incubation. **(F)** Flow cytometry of *S. pneumoniae* TIGR4 cells obtained from untreated (cyan) and 6.3 μ M peptide-treated (purple) cells stained with the fluorescent dye PI. Detection of cell-penetrating peptides in living cells by confocal laser scanning microscopy using **(G)** *S. pneumoniae* TIGR4 and **(H)** *S. pneumoniae* D39 containing active site-mutated higBA (shown data are images of R73A). **(G,H)** Shown data are representative maximum intensity Z projection images of three independent experiments with scale bar, 25 μ m. **(I)** FACS data of *S. pneumoniae* D39 that was treated with 6.3 μ M peptide and contained the active site-mutated higBA

1.4 Discussion

1.4.1 Insights into the Transcription Regulation Mechanism of the HigBA System

Although many other proteins present HTH DNA-binding motifs, antitoxins with HTH motifs in the HigBA system not only reveal differences in the location of their DNA-binding motifs but also show functional differences. HigA antitoxins have almost no structural similarity to other proteins with an HTH motif, such as the domain position, dimerization mechanism, and binding pattern to the cognate HigB toxin. The structural variability of these HigA antitoxins will cause differences in their transcriptional regulation. In the case of *S. pneumoniae* HigA, the binding between DNA and HigA is dominated by certain residues belonging to the HTH motif and their neighboring residues. When DNA was added to HigA through titration, these residues showed an overall

reduction in NMR peak intensity, which shows that these residues are affected by DNA binding.

HigBA and HigA from *S. pneumoniae* seem to have different binding affinities for the four palindromic sequences tested. HigA has been suggested to regulate transcription by sequence-specific interactions with DNA and by multisite binding (53). In addition, my experimental data show that the HigBA complex has higher binding affinity to DNA than to HigA antitoxin alone. Because the affinities of HigA to *Pal-I*, *Pal-II* and *Pal-III* are weak compared with those of HigBA, the DNA-binding modes of HigA and the HigBA complex will differ. Additionally, an operator appears to be preferentially recognized when the HigBA complex is formed. Therefore, there might be more than one transcriptional regulation mechanism. In general, the diversity of transcriptional regulation mechanisms due to the structural variability of HigA antitoxins is likely a key aspect of the transcription regulation mechanism governed by the HigBA TA system.

1.4.2 Application of Structural Studies to the Catalytic Mechanism of HigB

HigB from *S. pneumoniae* is structurally homologous to the ribosome-dependent toxin RelE (54); however, experimental results showed possible similarities to the ribosome-independent toxin YoeB (52). Since HigBA system proteins share very low sequence similarity, many proteins belonging to the HigBA system have been elucidated via structural studies (30-32). Therefore, the deposition of structural information regarding additional HigBA proteins in the database may allow for confirmation of whether the C-terminal helix present in HigB is related to target specificity. Knowledge

about the regulation of type II toxin-mediated cleavage could explain the mechanism underlying the cellular responses of bacteria to environmental changes (54,55). Furthermore, recent studies demonstrated that type II toxins play crucial roles in bacteria and participate in various functions, such as drug resistance and persistent cell formation (56,57). Therefore, understanding the molecular mechanism of RNA recognition can provide fundamental principles for understanding toxin function. Residues that have a major role in the activity of HigB have been proposed according to the results of structural and functional studies; however, data on other types of HigB are needed to understand the detailed mechanisms, such as substrate recognition and catalytic stabilization.

The active site of HigB from *S. pneumoniae* is positively charged, suggesting possible interactions with the negatively charged RNA phosphate backbone (Figure 19). As evidenced by the mutational study, the following four key residues participate in catalysis and constitute the active site: R68, R73, F90 and K92. Individual active site residues can significantly contribute to the activity of HigB. The basic nature of the positively charged residues Arg68 and Arg73 is thought to contribute to the charge stabilization of the negatively charged transition state (54). The HigBs may also have specificity depending on the type of residue containing the phenyl ring. F90 might be important for the catalytic efficiency of HigB and facilitate the positioning of nucleotide substrates (55). Taken together, the evidence shows that arginine and phenylalanine, which constitute the active site, will participate in the RNA cleavage reaction by organizing the active site and substrate geometry through an acid-base mechanism. Lysine may only be related to additional charge stabilization in the catalysis without greatly affecting the activity of *S. pneumoniae* HigB in this study (58).

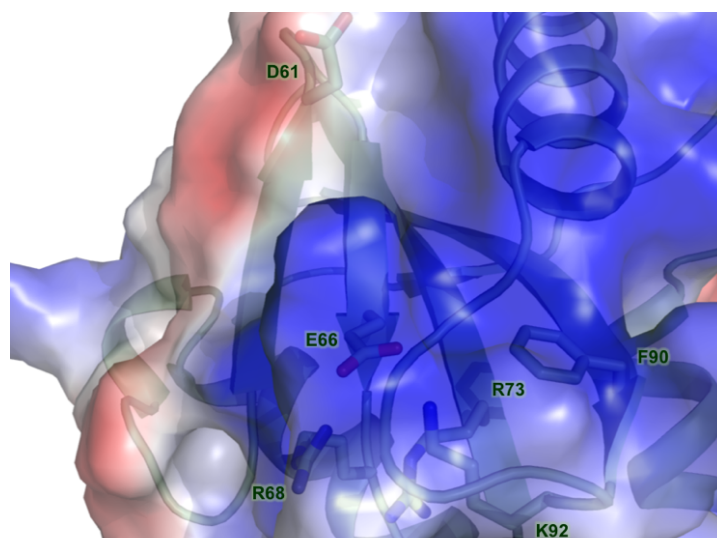


Figure 19. Active site of HigB from *S. pneumoniae*. It is positively charged, indicating possible interactions with the negatively charged RNA phosphate backbone

1.4.3 HigBA Peptide Derivatives Are Promising New Antimicrobial Agents

The active site of HigB is not occluded, although the formation of the HigBA complex can block the toxicity of HigB. I focused on the neutralization of HigB toxin via binding with HigA and designed a peptide that mimics the binding site between HigB and HigA to estimate the potential of an antibiotic peptide through free toxin release by competition with HigB or HigA at the binding site. In my mutational study, the single point mutation of any interacting residue in the tight binding region of the HigBA complex did not result in HigB toxicity. However, the HigBA complex was fully disrupted by mutation of the binding region-mimicking peptides containing numerous interacting residues; thus, a large increase in RFU was observed in the *in vitro* test. The active site of HigB is not blocked by HigA in the HigBA complex structure. And the active site and HigA binding region of HigB are distant from each other. Therefore, it can

be inferred that the peptide blocks the toxicity of HigB allosterically. These notable characteristics are also observed in other HigBA complex structures. In *P. vulgaris* HigBA complex, *P. vulgaris* HigA does not cover the *P. vulgaris* HigB active site and only forms a minimal boundary junction (31). Similarly, *V. cholerae* HigA does not interact with the active site of *V. cholerae* HigB but sufficiently neutralizes the *V. cholerae* (30) HigB . In general, HigB inhibition likely is not solely mediated by active site obstruction by HigA.

In my *in vivo* experiments, the peptides designed based on structural information about HigBA also successfully penetrated the cell membrane of *S. pneumoniae* and proved its growth arrest effect on *S. pneumoniae*. Therefore, I suggest the possibility of new antimicrobial agents based on structural and functional studies of the HigBA TA system, which has a completely new mechanism that does not exist in current antibiotics. HigB toxin does not exhibit toxicity when it is part of a TA complex because the HigA antitoxin completely blocks the active site of the HigB. However, when a peptide binds to a TA complex and interacts with its binding partners, the complex is disrupted by the peptide inhibitor and the toxin is released from the complex. Additionally, in the case of the VapBC and HicBA systems, the activity of the toxin is regenerated when an active site of the free toxin is exposed by the addition of a peptide mimicking the binding site (59,60). Taken together, my study establishes that the structurally designed peptides can function as bactericidal agents in *S. pneumoniae*. Furthermore, improvements in activity and stability obtained by modifying current candidate peptides using hydrocarbon α -helix stapling or hydrogen bond surrogates will enable these antibiotic peptides as a new type of antimicrobial agent that targets specific pathogenic bacteria (9,61,62).

1.5 Conclusion

Toxin-antitoxin (TA) system occur more often in pathogenic bacteria than nonpathogenic bacteria. This would imply that TA systems are correlated with bacterial pathogenicity. In addition, TA systems are utilized by pathogenic bacteria to survive and not found in any eukaryotes. Therefore, they would be a promising drug targets for bacterial pathogens.

Currently, seven type II TA loci have been reported in *S. pneumoniae*. In this study, I present the complex structure of HigBA from *S. pneumoniae* as determined by X-ray crystallography. The crossed-scissor constitutes a new type of interface between HigB and HigA. The binding interface showed critical residues in the formation of the HigBA complex. HigB from *S. pneumoniae* showed *in vitro* ribonuclease activity, and the active site of HigB has been successfully deduced through numerous single point mutations. The peptides that mimicked toxin or antitoxin helices could hinder HigBA complex formation. These peptides could penetrate *S. pneumoniae* and exert bactericidal activity. The antitoxin does not block the active site of HigB in the HigBA complex structure, thus revealing that peptide binding may allosterically inhibit HigB activity. HigA possesses DNA-binding activity through its helix-turn-helix motif (HTH) and modulates HigBA expression. The results of isothermal titration calorimetry (ITC) experiments showed that the HigBA complex has a higher affinity for DNA than the HigA complex based on the K_d values. It could be speculated that HigBA complex could be a stronger transcription repressor than HigA antitoxin. In addition, the residues of HigA that are important for DNA binding were investigated by nuclear magnetic resonance (NMR). This approach may contribute to my understanding of the structure-function relationships of TA systems,

including the HigBA system. My biochemical and structural studies will provide valuable information and insights into the molecular basis of TA systems as an antibacterial target.

Chapter 2. Structural and functional study of the *Klebsiella pneumoniae* VapBC toxin–antitoxin system, including the development of a substance that activates VapC

2.1 Introduction

Klebsiella pneumoniae is gram-negative, facultative anaerobic, rod-shaped bacterium, which includes two kinds of strains such as “Classic” non-virulent *K. pneumoniae* (c-KP) and hypervirulent *K. pneumoniae* (hv-KP). *K. pneumoniae* belongs to the *Enterobacteriaceae* family and is an opportunistic pathogen, which is a normal commensal living in the mouth and gut. However, it causes diseases such as acute pneumoniae when *K. pneumoniae* transports to elsewhere among patients with weak respiratory defense. Within the last few decades, *K. pneumoniae* is resistant to many antibiotics, among which carbapenem-resistant *K. pneumoniae* (CRKP) is the most lethal pathogen with 44% mortality rate. In this chapter, I focused on the type II TA systems of *K. pneumoniae* MGH 78578 (ATCC 700721) strain, which now is highly resistant to several antibiotics, including ampicillin, trimethoprim-sulfamethoxazole, gentamicin, etc.

Type II TA systems are more broadly distributed in pathogenic bacteria than in nonpathogenic bacteria (63). This suggests that TA systems are closely related to bacterial pathogenicity. Additionally, TA systems are not found in any eukaryotes and are therefore

a promising drug target for bacterial pathogens (9). Dozens of structures from the TA systems of pathogenic bacteria have been solved in structural and functional studies; however, the structural information on TA systems in *K. pneumoniae* MGH 78578 is still unknown (64). To gain molecular insights into and validate the *K. pneumoniae* TA system as a future drug target, it is essential to explore the structure of *K. pneumoniae* TA systems.

VapBC is one of the largest families of type II TA systems. To date, at least 11 complex structures have been identified in the VapBC TA system: *Neisseria gonorrhoeae* FitAB (65), *Shigella flexneri* VapBC (66); *Rickettsia felis* VapBC2 (67); *Caulobacter crescentus* VapC1 (68); *Haemophilus influenzae* VapC1 (69); *M. tuberculosis* VapBC3 (70), VapBC5 (71), VapBC11 (72), VapBC15 (73), VapC26 (59) and VapBC30 (74). These VapBC complexes highlight the great structural complexity of VapB, which contains a variable DNA-binding domain and flexible region, whereas VapC exhibits a conserved rigid domain.

The VapC toxin contains a pilus retraction protein (PilT) N-terminal (PIN) domain, which is crucial for ribonuclease (RNase) activity. These PIN domains comprise approximately 130 amino acid proteins and contain a strictly conserved negatively charged acidic quartet of residues coordinated by Mg²⁺ in the active site. On the other hand, the cognate antitoxin VapB folds into a ribbon-helix-helix (RHH) DNA-binding motif at the N-terminus and wraps the active site of VapC via its C-terminal helices (59). As VapB sterically blocks the catalytic site of VapC and acts as a tight binding inhibitor, the molecules that inhibit the binding between VapB and VapC can generate and release the free toxin. There are previous reports about these inhibitory molecules acting as binding competitors, leading to growth arrest or ultimately cell death in other pathogenic bacteria (59,60). The exploitation of TA systems as an antibacterial strategy via artificial

activation of the toxin has been proposed as a potential treatment approach (75). In some recent studies, sequence-specific antisense peptide nucleic acid oligomers and peptide-based inhibitors led to bacterial cell death, highlighting this strategy (72,76).

Here, the first crystal structure of the VapBC complex from *K. pneumoniae* was presented at a resolution of 2.00 Å. First, through structural analysis, I found that R79 of VapB displaces the coordinated Mg²⁺ from the neighboring D9, E43 and D90 of VapC to D9, D90 and D111 of VapC and abolishes the RNase activity of VapC. This finding was further verified by site-directed mutagenesis and *in vitro* RNase activity experiments. I designed peptides mimicking the binding interface of the VapBC complex and confirmed the complex disruption ability of peptides by the successful generation of RNase activity of the VapC toxin. Additionally, using the structural information, a total of 400 small molecules were screened. The final small-molecule candidate is thought to be a potent structure-based inhibitor with complex disrupting efficacy. This comprehensive investigation of the *K. pneumoniae* VapBC system will help to decipher unsolved conundrums in VapBC systems and develop potential antimicrobial agents against *K. pneumoniae*.

2.2 Experimental procedure

2.2.1 Cloning, protein purification and mutation

For the structural determination of the VapBC complex, the genes encoding *K. pneumoniae* (strain MGH78578) VapB (*kpn_04185*) and VapC (*kpn_04186*) were

amplified by PCR using the primers *vapB*-F/*vapB*-R¹ and *vapC*-F/*vapC*-R (Table 8). The restriction enzymes Nde1 and Xho1 were used to doubly cleave all of the PCR products and vectors. Then, the cleaved PCR products were ligated to pET-21a (*kpn_04185*) and pET-28a (*kpn_04186*). The pET-28a vector, used for VapC (*kpn_04186*), has an N-terminal tag (MGSSHHHHHHSSGLVPRGSH). The cloned plasmids were cotransformed into competent *E. coli* BL21(DE3) cells (Novagen, USA). The bacterial cells were grown at 37°C using Luria broth (LB) until the optical density at 600 nm (OD₆₀₀) reached 0.6. The cells were then induced by 0.5 mM IPTG and further incubated for 4 h at 37°C (Figure 20A). The induced cells were centrifuged at 11,355 × *g* and suspended in buffer containing 20 mM Tris-HCl, pH 7.9, and 500 mM NaCl with 5% glycerol. The suspended cells were lysed by ultrasonication and centrifuged at 28,306 × *g*. After centrifugation, the supernatants containing soluble proteins were loaded onto a Ni²⁺ affinity open column (Bio-Rad, USA) equilibrated in advance with buffer A. The bound proteins were washed with buffer A containing 100 mM imidazole and eluted by an imidazole gradient (150–500 mM) (Figure 20B). The eluted proteins were diluted with buffer containing 20 mM HEPES, pH 7.5 and 100 mM NaCl and further purified using a HiTrap Q HP anion-exchange chromatography column (GE Healthcare, UK) with a NaCl gradient (200–800 mM). These eluted proteins were exchanged with a buffer containing 20 mM HEPES, pH 7.5 and 400 mM NaCl by size-exclusion chromatography on a HiLoad Superdex 200 prep-grade column (GE Healthcare, UK) and concentrated to 20 mg/ml using an Amicon Ultra Centrifugal Filter Unit (Millipore, USA).

For the purification of the selenomethionine (SeMet)-labeled VapBC complex, the same procedure described above was used, except that the cells were grown in SeMet Medium Base plus Nutrient Mix (Molecular Dimensions, USA) containing extra SeMet.

To create VapC mutations, forward (F) and reverse (R) primers for D9A, E43A, D90A and D111A were used (Table 8). The mutations were created by using the EZchange™ Site-Directed Mutagenesis Kit (Enzynomics, South Korea). PCR products were ligated to pET-28a with an N-terminal tag (MGSSHHHHHSSGLVPRGSH). The VapC and mutated VapC proteins were produced by identical steps to those of native VapBC complexes. The purities of the purified proteins were verified by SDS-PAGE at every step.

Table 8. Primers used for cloning and producing mutations.

Primer	Sequence
<i>vapB</i> -F ^a	5'-GGAATTC <u>CATATG</u> AGCATGATGGCTGAAAG-3'
<i>vapB</i> -R ^{1,b}	5'-CCGCTC <u>GAGTT</u> ACCACTCCTTGCGTAGC-3'
<i>vapB</i> -R ^{2,b}	5'-CCGCTC <u>GAGCC</u> ACTCCTTGCGTAGC-3'
<i>vapC</i> -F ^a	5'-GGAATTC <u>CATATG</u> ACCTCCGGATCTGCGC-3'
<i>vapC</i> -R ^b	5'-CCGCTC <u>GAGTT</u> ATTCAGGGTGGATTTTCG-3'
<i>D9A</i> -F ^a	5'-GGATCTGCGCTTTTGTATACCAATATTCTTATT-3'
<i>D9A</i> -R ^b	5'-AATAAGAATATTGGTATCAAAAAGCGCAGATCC-3'
<i>E43A</i> -F ^a	5'-CTGATTACCTGGATGGAGGTGATGGTTGGCGCT-3'
<i>E43A</i> -R ^b	5'-AGCGCCAACCATCACCTCCATCCAGGTAATCAG-3'
<i>D90A</i> -F ^a	5'-AAGCTTAAGCTGCCGGATGCCATCATTCTGGCG-3'
<i>D90A</i> -R ^b	5'-CGCCAGAATGATGGCATCCGGCAGCTTAAGCTT T-3'
<i>D111A</i> -F ^a	5'-ACGCGGAATACGAAGGATTTTGCCGGTATTCT-3'
<i>D111A</i> -R ^b	5'-AGGAATACCGGCAAAATCCTTCGTATTCCGCGT-3'

^{a, b} F and R represent forward and reverse, respectively. Enzyme sites are underlined.

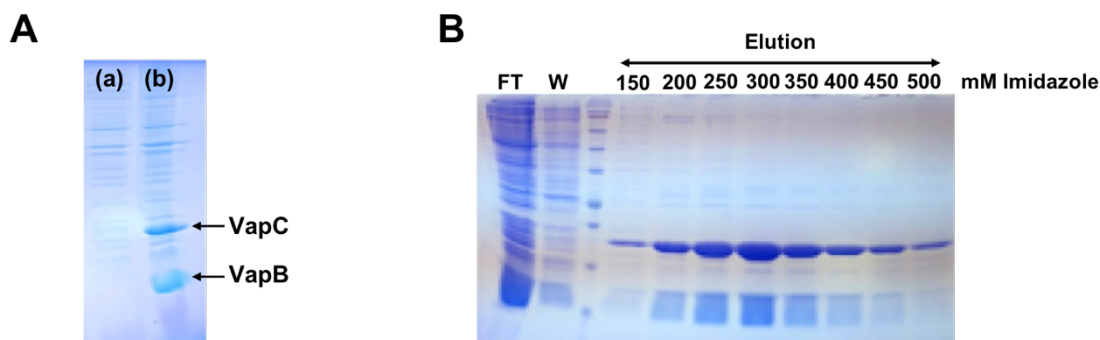


Figure 20. Expression and purification of VapBC complex from *K. pneumoniae*. (A) Expression of VapBC complex from *K. pneumoniae*. Lanes: a, uninduced whole-cell; b, induced whole-cell. (B) Purification of VapBC from *K. pneumoniae* by gradient elution using an open Ni²⁺-affinity column. FT, flowthrough; W, wash.

2.2.2 Crystallization, data collection and processing

To crystallize the VapBC complex, the sitting drop vapor diffusion method was employed by using the Wizard Classic crystallization screen series (Rigaku, Japan) at 20°C. The final crystallization condition was 0.1 M sodium citrate, pH 5.5 and 200 mM lithium sulfate (Figure 21). Crystals were cryoprotected with 20% glycerol and flash-cooled in liquid nitrogen. The diffraction data were collected using an ADSC Quantum Q270r CCD detector at beamlines 5C and 11C of Pohang Light Source, Republic of Korea. All raw data were scaled and processed by using HKL2000 (77). The detailed statistical information is shown in Table 9. During the structural calculation, PHENIX (78) was used to automatically build the model, and Coot (79) was utilized to refine it. REFMAC and PHENIX (78,80) were employed to obtain the plausible R_{work} and R_{free} values. MolProbity (81) was used to validate the overall geometry. PyMOL (The PyMOL Molecular Graphics System, Schrödinger, LLC., USA) was used to generate figures (39).

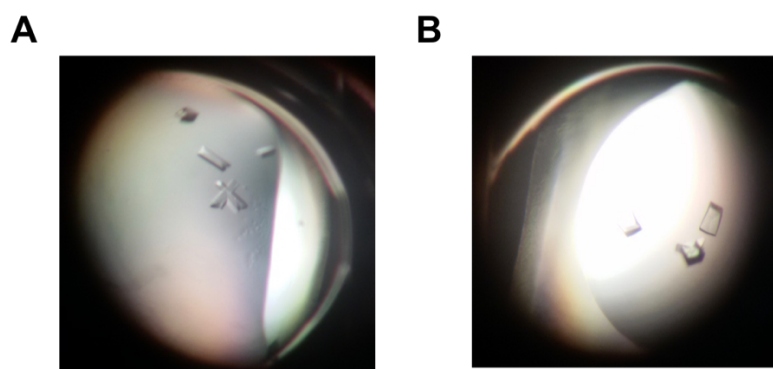


Figure 21. Generated crystals of VapBC from *K. pneumoniae*. (A) Crystal of native form. (B) Crystal of SeMet form.

Table 9. Data collection and refinement statistics for SeMet-substituted and native structures.

(a) Data collection details. Values in parentheses are for the highest-resolution shell.

Data set	SeMet	Native
X-ray source	5C beamline of PLS, Korea	5C beamline of PLS, Korea
X-ray wavelength (Å)	0.9794	0.9795
Space group	C222 ₁	C2
Unit cell parameters		
a, b, c (Å)	79.200, 110.323, 59.703	110.435, 79.019, 59.609
α , β , γ (°)	90.000, 90.000, 90.000	90.000, 89.985, 90.000
Resolution range (Å)	50.0-2.60 (2.64-2.60)	50.0-2.00 (2.04-2.00)
Molecules per ASU	VapBC heterodimer	2 VapBC heterodimers
Observed reflections ($>1\sigma$)	110563	139747
Unique reflections	8245	31667
$\langle I/\sigma(I) \rangle$	57.8 (5.02) ^e	48.3 (8.81) ^e
Completeness (%)	99.9 (100.0) ^e	96.8 (99.9) ^e
Multiplicity ^a	13.4 (10.8) ^e	4.4 (4.7) ^e

R_{pim} (%) ^b	5.4 (63.2) ^e	3.7 (26.7) ^e
CC _{1/2} , CC	(0.912, 0.977) ^e	(0.890, 0.971) ^e

(b) Refinement statistics

Data set	SeMet	Native
R_{work} ^c (%)	26.8	24.4
R_{free} ^d (%)	29.0	27.2
No. of atoms/RMS	1252/5.07	3192/2.72
RMSD ^f from ideal geometry		
Bond distance (Å)	0.008	0.005
Bond angle (°)	1.099	1.056
Ramachandran statistics		
Most favored regions (%)	98.01	96.70
Additional allowed regions (%)	1.99	3.30
Residues in disallowed regions (%)	0.00	0.00
PDB ID	7BY2	7BY3

^a $N_{\text{obs}}/N_{\text{unique}}$

^b $R_{\text{merge}} = \Sigma (I - \langle I \rangle) / \Sigma \langle I \rangle$

^c $R_{\text{work}} = \Sigma_{hkl} ||F_{\text{obs}}| - k |F_{\text{calc}}|| / \Sigma_{hkl} |F_{\text{obs}}|$

^d R_{free} was calculated in the same way as R_{work} but with 5% of the reflections excluded from the refinement.

^e Values in parentheses indicate the highest-resolution shell.

^f Root-mean-square deviation (RMSD) was calculated with REFMAC.

2.2.3 *In vitro* RNase assay for VapC and VapC mutants

The RNase activities of VapC and VapC mutants were confirmed using an RNase Alert Kit (Integrated DNA Technologies, USA). In this assay, each well contained 50 pM of synthetic RNA containing a fluorophore at one end and a quencher group at the other end. If the prepared RNA is contacted by RNase, the quencher is detached. Then, the resulting fluorescence during the 1 h reaction period was detected by a SPECTRAmax GEMINI XS spectrofluorometer (Molecular Devices, USA) at 490 nm and 520 nm as the excitation and emission wavelengths, respectively. For this assay, the purified VapC and

VapC mutants were treated with 10 mM EDTA to remove metal ions and exchanged with purification buffer containing 10 mM Mg²⁺. In each experiment, the concentration of both VapC and VapC mutants was 10 μM. Forty units of RiboLock™ (Thermo Scientific, USA) was added to each well to prevent contamination. RiboLock™ does not inhibit prokaryotic RNases I and H. VapC is similar in architecture to RNase H and is thus not affected by RiboLock™ (82). The final concentration of RNA was 5 pM, and the buffer components were 20 mM HEPES, pH 7.5 and 400 mM NaCl.

2.2.4 Complex disruption assay by the peptides mimicking the VapBC interface

To disrupt the VapBC complex and activate the VapC toxin, several peptides mimicking the binding interface of VapBC were designed (Table 10). The peptides were designed through structural analysis and synthesized by ANYGEN (GwangJu, South Korea). In these assays, the peptide (100 μM) was added to the VapBC complex (10 μM), and the resulting fluorescence (RFU) from the activated VapC toxin was measured. Other experimental protocols used for the peptides were the same as those used for the RNase activity test of VapC and VapC mutants.

Table 10. Peptides used to disrupt the binding interface of VapBC.

Name	Residues (N- to C-terminus)	Mimicked protein	Mimicked region
VapB ⁷¹⁻⁷⁸	GMEYQRQL (71-78)	VapB	α3
VapB ^{71-78,Y74A}	GMEAQRQL (71-78)	VapB	α3
VapB ^{71-78,Q75A}	GMEYARQL (71-78)	VapB	α3

VapB ^{71-78,Y74A,Q75A}	GMEAARQL (71-78)	VapB	$\alpha 3$
VapB ⁷¹⁻⁷⁹	GMEYQRQLR (71-79)	VapB	$\alpha 3$
VapB ⁷¹⁻⁸⁰	GMEYQRQLRK (71-80)	VapB	$\alpha 3$
VapC ¹⁰⁻¹⁷	TNILIDLF (10-17)	VapC	$\alpha 1$
VapC ⁹⁻¹⁷	DTNILIDLF (9-17)	VapC	$\alpha 1$
VapC ¹⁰⁻¹⁸	TNILIDLFS (10-18)	VapC	$\alpha 1$
VapC ⁹⁻¹⁸	DTNILIDLFS (9-18)	VapC	$\alpha 1$

2.2.5 Structure-based pharmacophore generation and molecular docking

The structure-based drug design was carried out with a structure-based pharmacophore (SBP) model and molecular docking simulation to virtually screen the primary hit compounds. SBP modeling, which extracts the chemical features from the protein-ligand complex structure, was performed to generate an SBP model of the crystal structure of the VapBC complex (PDB ID: 7BY3). Receptor-ligand pharmacophore generation was used in the pharmacophore generation tools of Discovery Studio (DS) 2018 software (DASSAULT SYSTEMES, 2017) with the default parameters. The SBP model, having four significant chemical features (two hydrogen bond (HB) donors, one HB acceptor, and one hydrophobic interaction), was designed by considering only the VapB $\alpha 2$ - $\alpha 3$ loop region (W64, C67, and Y74 of VapB) as a replacement ligand to inhibit the protein-protein interaction. The generated SBP model was used to retrieve a total of ~610,000 Korea Chemical Bank (KCB) compounds and select ~16,000 compounds by filtering.

Subsequently, the molecular docking simulation was performed with the resulting compounds and 7,155 diverse set compounds, representing a total of ~610,000 KCB

compounds. The target binding site of VapC was set from the cocrystal structure of VapB, especially the $\alpha 2$ - $\alpha 3$ loop region with a 14 Å radius sphere. The 3D structure of VapC was refined and protonated by the Prepare protein tool implemented in DS 2018. To perform the docking simulation, CDOCKER(83) was used in DS 2018. CDOCKER is a CHARMM-based docking tool that uses a powerful ligand flexibility algorithm and a refinement process that performs random rotation and grid-based simulated annealing at high temperatures. The resulting hit compounds were ranked by the score, which considers both fit value and negative CDOCKER interaction energy (including van der Waals and electrostatic interactions).

2.2.6 Assay for complex disruption of small molecules that occlude the interface pocket

To disrupt the VapBC complex and activate the VapC toxin, 400 small molecules were initially selected by virtual screening using the pharmacophore model and molecular docking. These 400 small molecules were provided by KCB dissolved in DMSO solution in 384-well plates. In this virtual screening, small molecules that are expected to occlude the interface pocket of the VapBC complex were explored and listed in the order of their virtual fitness scores as criteria for selecting initial candidates. Small molecules (1 μ M) were added to the VapBC complex (10 μ M), and their efficacies for activating VapC were tested. Other experimental protocols were the same as those described for the complex disruption assay by the peptides. The synthetic procedures of the final selected two compounds were as described in Supporting information. The purity of all compounds was > 95%, as determined by LC-MS.

2.2.7 Growth assay and colony forming unit measurement

The genes encoding VapC were additionally cloned into pBAD33. The cloned plasmid was transformed into competent *E. coli* BL21 (DE3) cells with previously cloned genes encoding VapB. This compatible plasmid pair (pBAD33 and pET-21a) was grown overnight at 37°C in M9 minimal medium plus 25 µg/ml chloramphenicol and 50 µg/ml ampicillin. The overnight cultures were diluted 50-fold and further grown for the next 5 h. At an OD₆₀₀ of 0.2, 0.2% arabinose was added. For the growth assay, 0.5 mM IPTG was added after 1 h. For the colony forming unit (CFU) measurement, every 30 minutes, cell samples were collected and streaked onto LB medium plates with 0.2% glucose and 0.5 mM IPTG. The plates were incubated for 16 h before counting.

2.2.8 Isothermal titration calorimetry

Isothermal titration calorimetry (ITC) was carried out using a MicroCal200 (GE Healthcare, UK). Concentrations of proteins and DNA were determined by NanoDrop (Thermo, USA) at 280 nm and 260 nm, respectively. Stock solutions of peptides and small molecules were prepared at the appropriate concentrations. Titrations were performed at 25°C. Data were fitted to a single-site binding model with the Origin-based software provided by MicroCal200.

2.3 Results

2.3.1 Overall information on the VapBC complex

First, I validated the *K. pneumoniae* VapBC TA system experimentally. VapC expression resulted in considerable restraint of cell growth and a decrease in CFU. However, suppressed cell viability was almost fully rescued by the expression of VapB (Figure 22). To solve the structure of VapBC, the single-wavelength anomalous diffraction (SAD) data for the SeMet-labeled VapBC complex were refined (Protein Data Bank (PDB) ID: 7BY2) and used to solve the phase problem. Then, the native data were refined (PDB ID: 7BY3) by molecular replacement employing the structure of the SeMet-labeled VapBC complex as the search model.

As a result of the structural calculation of *K. pneumoniae* VapBC from native data, the overall conformation of the VapBC complex was obtained. The VapB antitoxin is divided into an N-terminal part containing a DNA-binding domain and a C-terminal part containing a toxin-binding region, which blocks the active site of the VapC toxin. Interestingly, the phased structure of VapBC from the SAD data showed an incomplete complex structure with the C-terminus of VapB digested; thus, the active site of VapC was not inhibited by VapB. Detailed new findings related to this observation will be described in the third subsection of the results and discussion section.

In the crystal structures, I observed two types of intermolecular interfaces, which originated from crystal packing. The first is a toxin dimerization-driven heterotetramer (Figure 23A). In this case, the interaction between α -helices in the adjacent toxin monomers is a main binding force. The other is an antitoxin dimerization-driven

heterotetramer (Figure 23B), which is mediated by the DNA-binding domain of the antitoxin.

A schematic diagram of the VapBC heterodimer is helpful for understanding the spatial arrangement of the secondary structural elements that make up the heterodimeric architecture (Figure 23C). In my native structure, the first β -strand of the VapB N-terminus was not observed due to the poor electron density in the map. According to the prediction by PSIPRED (84), VapB is expected to have an RHH DNA-binding domain (85) in the order $\beta 1$ - $\alpha 1$ - $\alpha 2$ (Figure 23D) at the N-terminus.

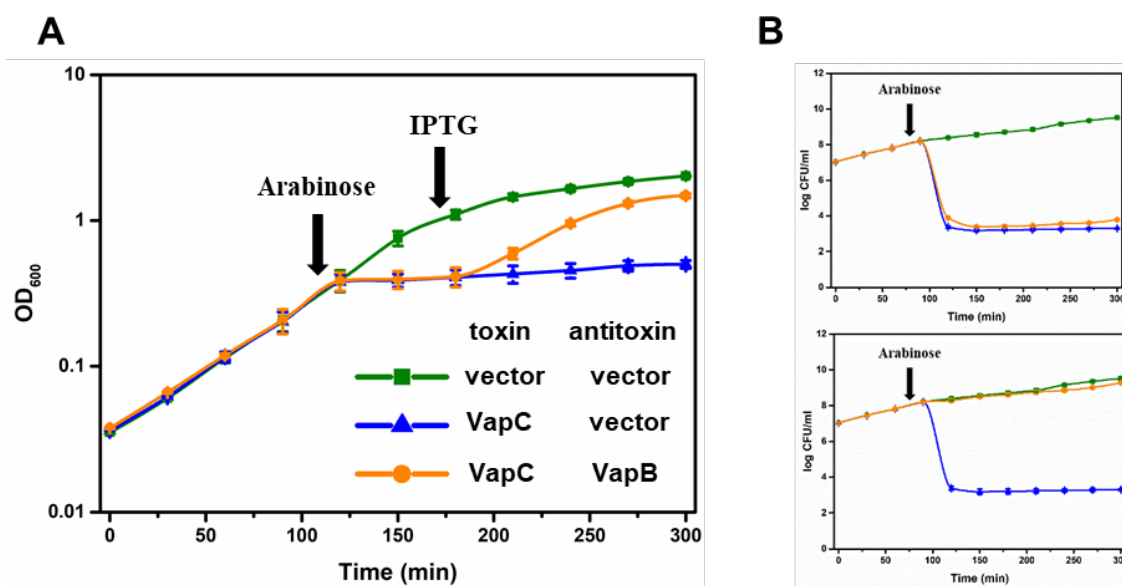


Figure 22. Growth assay and CFU measurement. (A-B) Each curve represents a variant written on the table in the graph. The data show the average values obtained in triplicate reactions; the standard deviations are indicated by error bars. (A) growth assay of *K. pneumonia* VapBC TA system. (B) Upper: CFU measurements of plates that treated with only 0.2% glucose. Lower: CFU measurements of plates that treated with both 0.2% glucose and 0.5 mM IPTG.

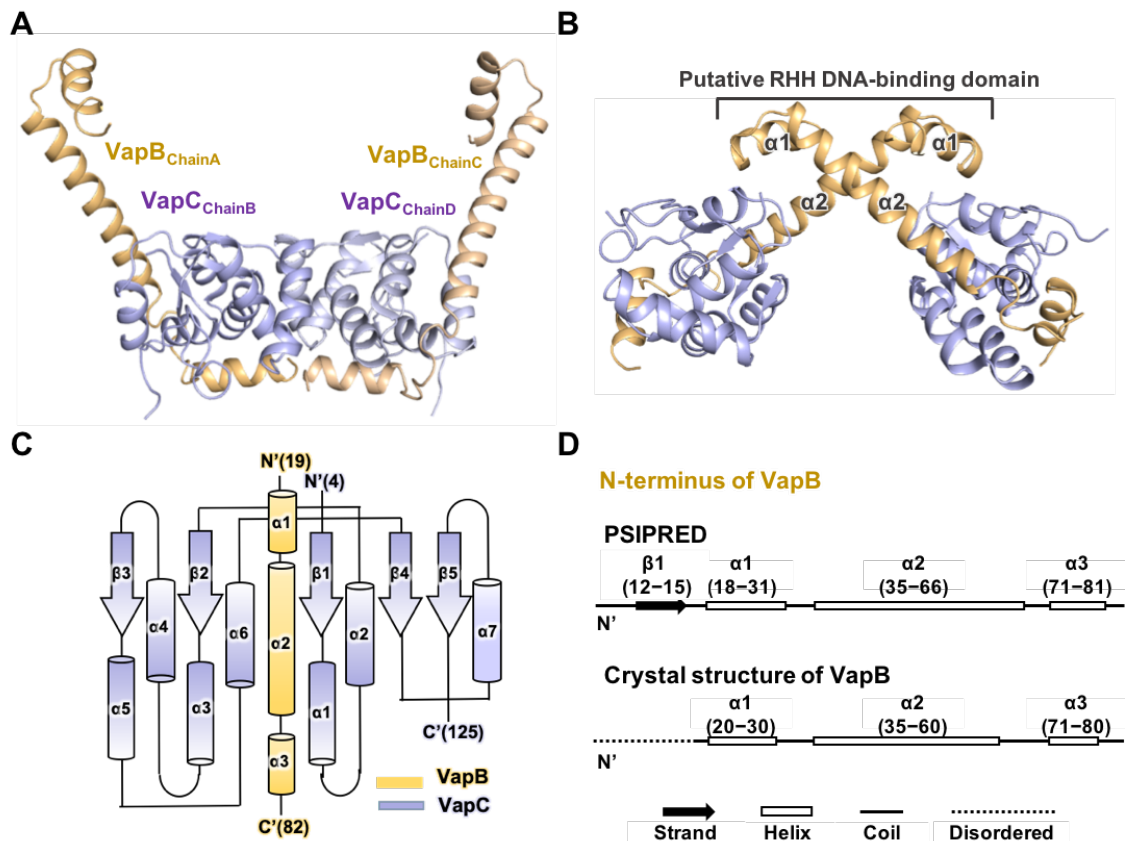


Figure 23. Overall structural information on *K. pneumoniae* VapBC (PDB ID: 7BY3). (A–C) Antitoxin VapB subunits are shown in yellow and the toxin VapC subunits are shown in light purple. (A) Heterotetrameric assembly of the VapBC complex containing an intermolecular interface formed by the dimerization of VapC. (B) Heterotetrameric assembly of the VapBC complex containing an intermolecular interface formed by the dimerization of the N-terminal DNA-binding domain of VapB. The DNA-binding domain of VapB is labeled. (C) Schematic diagram of the VapBC heterodimer showing the secondary structural architecture. (D) Secondary structure analysis of the N-terminal DNA binding domain of VapB. Prediction data using the PSIPRED server are presented with structural information on the N-terminus of VapB in the crystal structure.

2.3.2 Structural insights into *K. pneumoniae* VapBC compared with its homologs

To identify the structural characteristics of *K. pneumoniae* VapBC, a comparative analysis was performed with its structural homologs, and the complex structure was solved. To reflect the latest information, comparisons were made with relatively recently reported homologs since 2017. First, an amino acid sequence alignment of the VapC

toxins using Clustal Omega 1.2.1 (86) and ESPrpt 3.0 (87) was carried out. In this alignment, the primary sequences of *Mycobacterium tuberculosis* VapC11 (PDB ID: 6A7V) (72) and VapC26 (PDB ID: 5X3T) (59), *Caulobacter crescentus* VapC1 (PDB ID: 5K8J) (68), and *Hemophilus influenza* VapC1 (PDB ID: 6NKL) (69) were compared with that of *K. pneumoniae* VapC. The alignment revealed seven highly conserved residues (Figure 24A). The first, third, fourth and sixth conserved residues are negatively charged and acidic residues, such as aspartate and glutamate, which make up the active site of the toxin. Among the remaining three residues, the locations of the second threonine and seventh phenylalanine are closely related to the location of the active site, and hydrogen bonding and hydrophobic interactions between these residues and the active site residues support and contribute to the building and structural integrity of the active site (Figure 24B).

Despite the low sequence similarity (13.7% on average) to the four homologs, *K. pneumoniae* VapC shares structural similarity with the other VapC proteins. VapC toxins adopt a canonical $\alpha/\beta/\alpha$ sandwich fold composed of five parallel β -strands flanking seven α -helices. VapC toxins also similarly feature the PIN domain, which is essential for ribonuclease activity (88). The conserved acidic residues in PIN domain proteins coordinate with divalent metals and trigger catalytic activity based on acid-base reactions (82).

The four homologs were also compared with *K. pneumoniae* VapBC to determine the differences in the VapB structures and VapB and VapC binding patterns (Figure 24C). In comparison, the VapC structures had similar folds; however, the binding patterns of the VapC toxin with its cognate VapB and the VapB DNA-binding domains were quite different. The C-terminal toxin-binding region of VapB is intrinsically extremely flexible;

thus, structural folding and integrity are achieved only after binding to the toxin (59). For this reason, the α -helical contents and the loop contents of each VapB in each binding region between these VapB antitoxins and VapC toxins seem to have large differences. In addition, there are two different DNA-binding domains in VapB, including the RHH (85) and AbrB-type (89) domains. Interestingly, DNA-binding domains in VapB differ not only in their type of domain but also within the same domain type, and the orientation of the domain varies considerably depending on the curve at the hinge region. This emphasizes that the structural variability of VapB proteins causes a diversity of transcription regulation mechanisms and further explains the specificity in the recognition of their own promoter regions.

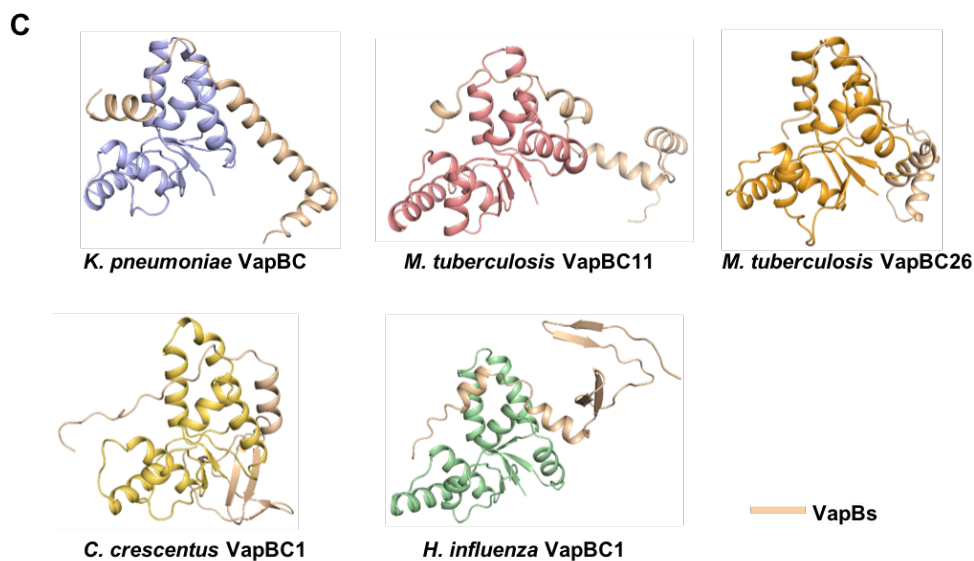
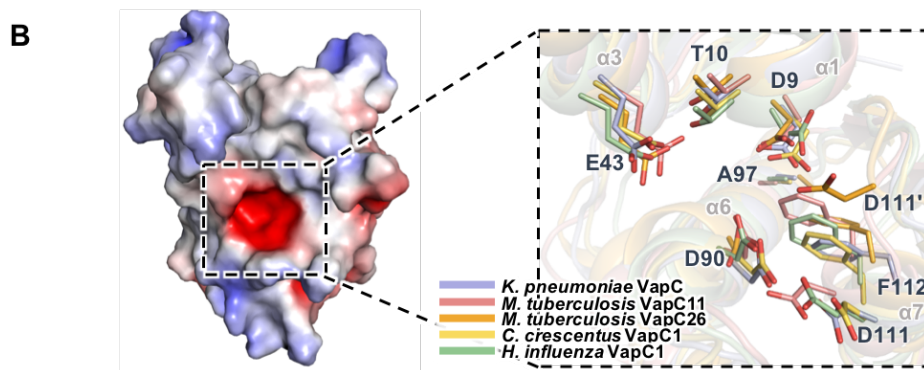
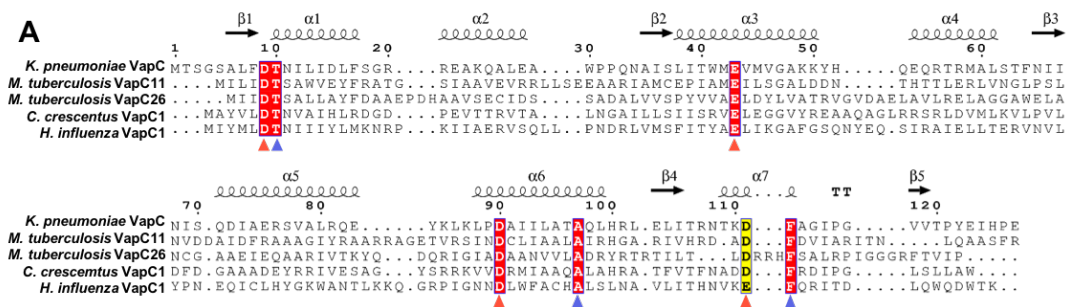


Figure 24. Structural comparison of *K. pneumoniae* VapBC with its homologues. **(A)** Sequence alignment of *K. pneumoniae* VapC with its homologues. The secondary structural elements of these proteins are shown above the alignment. Highly conserved residues are highlighted in red and yellow. Among them, the acidic active-site residues and residual residues are marked as red and blue triangles, respectively. **(B)** Electrostatic surface of VapC (left) (PDB ID: 7BY3). Positive and negative charges are colored blue and red, respectively. An acidic active site of VapC is shown enlarged in cartoon and stick representations (right) showing the locations of seven conserved residues in the structure of each homologue. Seven conserved residues are shown in stick representation. **(C)** Comparison of the VapBC complexes (PDB IDs: in the order of 7BY3, 6A7V, 5X3T, 5K8J, and 6NKL). Each VapBC complex is shown in the same direction based on the VapC structure. For VapC, the same colors as in Figure 24B are used.

2.3.3 RNase activity of VapC and unveiling the inhibition mechanism of VapB

As mentioned in the first subsection, the structure obtained from the SAD data is in an open form with an active site exposed due to the natural digestion of the C-terminus of VapB (Figure 25A). On the other hand, the native structure obtained from the native crystal shows a closed form with an active site in which the toxin-binding region of VapB is completely preserved (Figure 25A). In accordance with the innate nature of VapC, its RNase activity is only shown when divalent metal ions such as Mg^{2+} are present. *K. pneumoniae* VapC showed RNase activity only when Mg^{2+} was added to the protein solution. In the open form without VapB interference in the active site, Mg^{2+} is located in the midst of the conserved active site residues (D9, E43 and D90) of VapC. However, in the closed form, VapB covers the active site of the toxin. R79 of VapB exactly blocks the original Mg^{2+} site and displaces Mg^{2+} to the center of residues D9, D90 and D111 of VapC, causing the active site to switch from the open state to the closed state (Figure 25B). This inhibitory mechanism of the active site is a novel TA system mechanism. This inhibitory mechanism of the active site is first observed through two states of crystal structures.

To expand the importance of these results, I mutated each residue comprising the active site of VapC and measured the RNase activities of each VapC mutant (Figure 25C). From the graphs, which express the kinetics for 1 h and show a proportional plot for VapC, the residue with the largest contribution to activity was E43, and the residue with the least contribution was D111. In conclusion, as R79 of VapB causes the displacement of Mg^{2+} , VapC active site inhibition is achieved by completely abolishing the contribution of E43

to the RNase activity. However, based on the mutation experiments, when E43 of VapC is mutated to alanine, VapC still has approximately 40% of its RNase activity. This suggests that the RNase activity of VapC depends on the position of Mg^{2+} , which could be displaced by VapB, as well as the contribution of each residue constituting the active site.

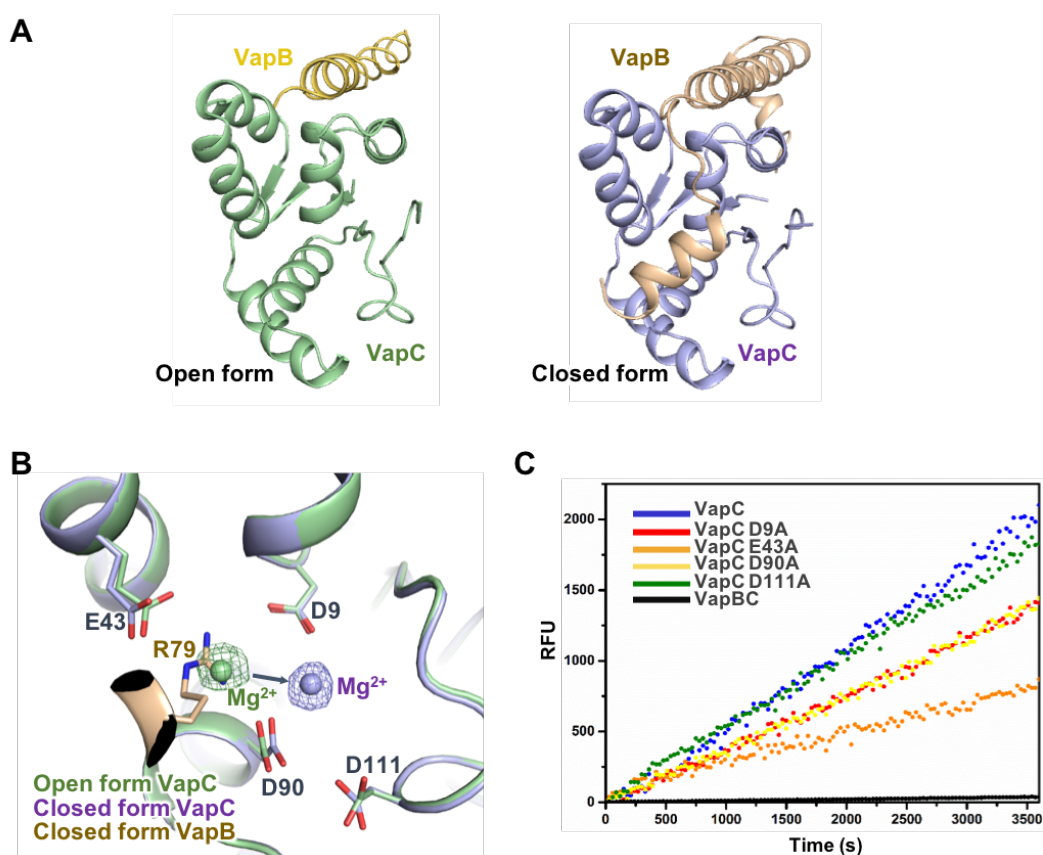


Figure 25. Active site and RNase activities of VapC. **(A)** Two forms of the VapBC complex structure: open form (left) (PDB ID: 7BY2) and closed form (right) (PDB ID: 7BY3). **(B)** Two forms of the active site are presented with a cartoon diagram of VapC. Four conserved residues are shown in stick representation. Active-site conformations are denoted as black dotted squares and enlarged. The 2m*Fo*-*DFc* electron density map of the Mg^{2+} site contouring at σ (calculated with PHENIX) is also displayed. In the open form of the VapC active site, the coordinated Mg^{2+} is located in the midst of residues D9, E43, and D90. In the closed form of the VapC active site, R79 of VapB triggers the displacement of Mg^{2+} . Consequently, R79 of VapB fills the original location of Mg^{2+} , and Mg^{2+} moves to the middle of D9, D90, and D111. **(C)** *In vitro* RNase activities of VapC, VapC mutants, and VapBC. Proteins were treated with EDTA to remove metal ions, and 10 mM Mg^{2+} was then added to proteins. In the assay, 10 μ M proteins were used, and a general RNase inhibitor (40 units) was used to prevent unintended contamination. The kinetics for the RNase activities of these proteins were recorded for 1 h. The data shown are representative of three independent experiments.

2.3.4 Exploration of peptides that activate VapC by disrupting the interface between VapB and VapC

If the formation of the TA complex is artificially inhibited, toxins freely released from the TA complex can arrest the growth or eventually cause the death of bacteria (9). Therefore, to design peptides capable of disrupting the *K. pneumoniae* VapBC complex, the interaction networks between VapB and VapC were analyzed based on the results of analyses from the proteins, interfaces, structures and assemblies (PISA) (90) and protein interactions calculator (PIC) (91) servers. The results showed that the $\alpha 3$ helix of VapB (Figure 26A) and $\alpha 1$ helix of VapC (Figure 26B) were most important in the dimerization interaction between VapB and VapC.

Therefore, several peptides were designed based on the sequence of the $\alpha 3$ helix of VapB and the $\alpha 1$ helix of VapC (Table 10). When a peptide is added to the VapBC complex, the inhibition efficacy of the peptide can be estimated by measuring the RNase activity generated by the free VapC, which is released by the disruption of the VapBC complex. In the complex disruption assay, although the $\alpha 3$ helix of VapB consists of G71–K80 (GMEYQRQLRK), the VapB^{71–78} peptide consisting of G71–L78 (GMEYQRQL), which excludes R79 of VapB that interacts with three active site residues (D9, E43 and D90) of VapC, showed high efficacy. Y74 and Q75 of VapB interact with E43 and D9 of VapC, respectively. As a result, when Y74 and Q75 were individually mutated to alanine, the VapB^{71–78, Y74A} peptide showed the highest efficacy among all of the designed peptides. The VapB^{71–78, Y74A, Q75A} peptide, in which both Y74 and Q75 are mutated to an alanine, showed a lower efficacy than the individual alanine-mutated VapB

peptides. This might be due to defects in the structural integrity of the α helix because of multiple alanine substitutions (Figure 26C).

When the VapB-mimicking peptides were treated with free VapC, the overall activity measured was slightly increased, but the pattern was similar to that resulting from treatment with VapBC (Figure 27A). Since the designed peptides are made by mimicking the binding interface of VapB and VapC, arithmetically, the more residues that participate in the binding of VapB and VapC are present in the peptides, the greater the complex disruption capability should be. However, if a peptide contains the residues that interact with the nucleic acid binding site of VapC, which is the active site of VapC, the disruption capability is inhibited. Moreover, the lack of structural integrity due to multiple alanine substitutions had little effect on the activity of VapC. In summary, among the residues involved in the binding of VapB and VapC included in the peptide, the more residues that interact with the residues constituting the active site of VapC, the more the activity of VapC is unintentionally inhibited. In particular, as shown in the mutational study, this phenomenon is more pronounced when the peptide contains a residue that interacts with D43, which contributes most to the activity of VapC.

In the VapBC complex structure, the $\alpha 1$ helix of VapC is composed of T10–F17 (TNILIDLF). Although D9 and S18 are not included in the $\alpha 1$ helix of VapC, the VapC^{9–18} peptides, including D9 and S18, which interact with VapB, showed lower efficacy than the peptide consisting of only the $\alpha 1$ helix. (Figure 26D). As a result, the importance of the α -helical nature in the artificial disruption of the TA complex was reconfirmed (92).

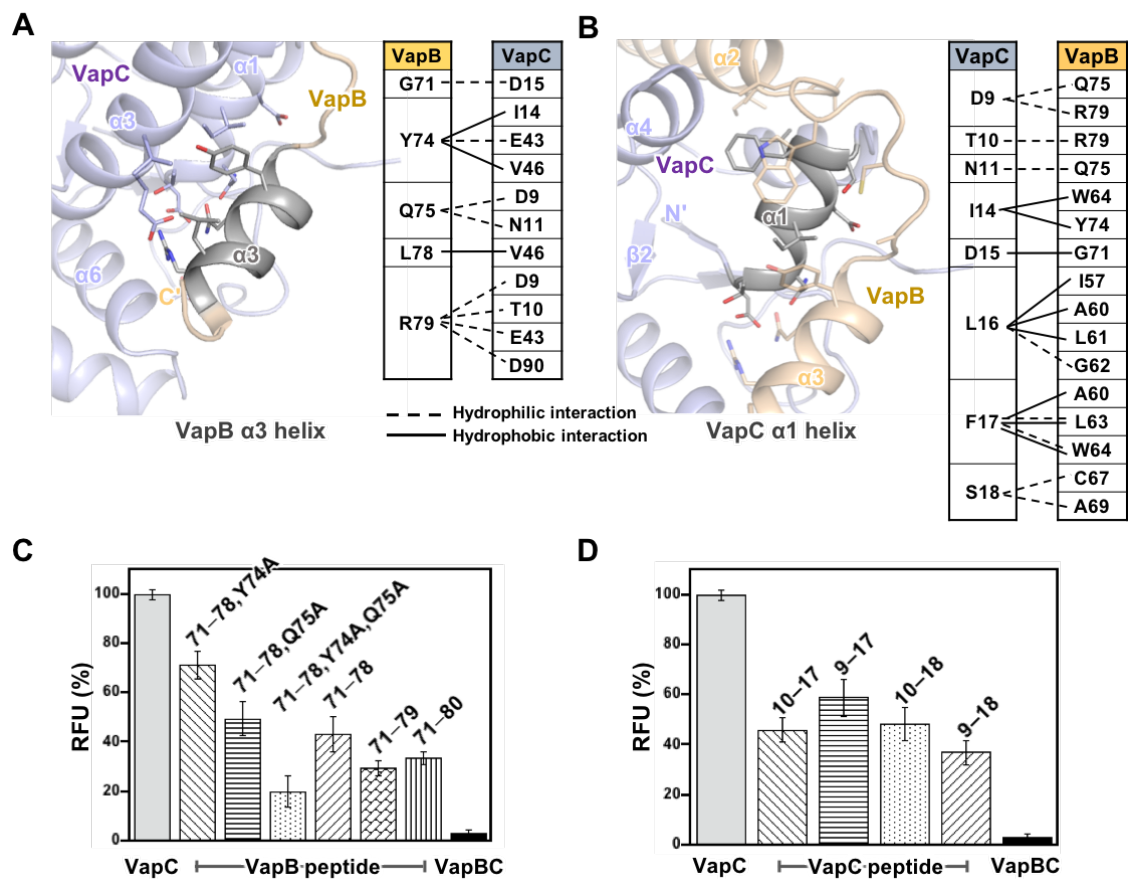


Figure 26. Heterodimeric interface of the VapBC complex (PDB ID: 7BY3) and efficacy of complex disruption using the designed peptides. **(A,B)** Residues involved in interaction networks are shown in stick representation. Schematic diagrams of the hydrophilic and hydrophobic interactions are provided in the table. **(A)** Intermolecular interaction network of the VapB $\alpha 3$ helix. **(B)** Intermolecular interaction network of the VapC $\alpha 1$ helix. **(C,D)** RNase activities resulting from peptides added to the VapBC complex. Activities generated by peptides are plotted in proportion to that of VapC. The pretreatments for the assay were the same as those described in Figure 25C. In these complex disruption assays, 100 μM peptides were added to 10 μM proteins, and their complex disruption efficacies were evaluated. Data are represented as the mean of three independent replicates \pm SD. **(C)** Efficacy of peptides designed based on the sequence of the $\alpha 3$ helix of VapB. **(D)** Efficacy of peptides designed based on the sequence of the $\alpha 1$ helix of VapC.

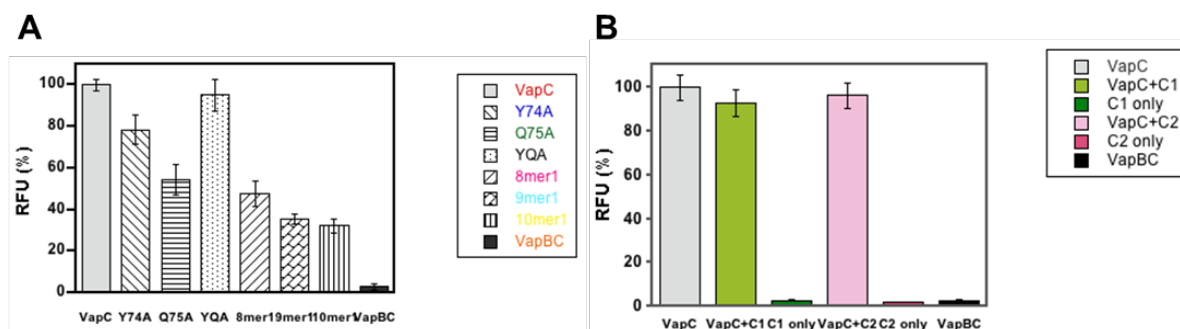


Figure 27. The effects of the peptides and small molecules on free VapC. **(A-B)** The data show the average values obtained in triplicate reactions; the standard deviations are indicated by error bars. **(A)** Treatment of the peptides on free VapC. **(B)** Treatment of small molecules on free VapC.

2.3.5 Exploration of small molecules that activate VapC by occluding the interface pocket

In parallel, based on the information on the interface between *K. pneumoniae* VapB and VapC, a total of 400 small-molecule candidates, which are selected from ~610,000 different kinds of compounds in KCB, capable of binding to the VapB binding pocket of the VapC surface were selected by virtual screening. The majority of these compounds are distributed in an MW range of 300~500 Da with an average of ~5.1 HB acceptors, ~2.2HB donors, and 6.8 rotatable bonds. The predicted AlogP values for most of the compounds are in the range of 0.5 ~ 5, with an average value of 2.8. Each compound was designed to disrupt the VapBC complex by binding not to the active site cavity of VapC but to the cleft through the $\alpha 2$ - $\alpha 3$ loop of VapB, linking the interface pockets (Figure 28A).

Using a similar assay method to that in the previous section, the inhibition efficacies of the compounds were ranked according to the amount of RNase activity by the free VapC released by the disruption of the VapBC complex. A total of 400 compounds were

narrowed to 25 according to inhibition efficacy ranking through triplicate tests, and these 25 small molecules were further narrowed through additional triplicate testing to the two compounds with the highest efficacy, named compound 1 and compound 2 (Figure 28B). These two final compounds did not affect the RNase activity of VapC when added to free VapC (Figure 27B), because they are designed to bind to the binding interface of VapB and other regions of VapC, not the active site of VapC.

These two compounds had a higher efficacy at 1 μM , which is one hundredth of the peptide concentration (100 μM) previously used. Therefore, compounds 1 and 2 are very efficient at disrupting the VapBC complex. Compounds 1 and 2 exhibited IC_{50} values of 0.42 μM and 0.40 μM , respectively (Figure 29). For better understanding, the results of molecular docking simulations of compounds 1 (Figure 28C) and 2 (Figure 28D) are also presented. The carbonyl group of compound 1 interacted with the positively charged amino group on the side chain of K50 by forming a strong HB. Residues E43, S18, and A48 also formed hydrogen and carbon-hydrogen bond interactions. Residues Y51, I14, and V46 formed π -alkyl and alkyl interactions. Similar to the HB of compound 1, the sulfonyl group of compound 2 was also found to have a strong HB with the positively charged amino group in the side chain of K50. Additionally, residues T10, N11, G47, and A48 formed carbon-hydrogen bonds and amide- π stacked interactions. Residues I14 and V46 were involved in the formation of π -alkyl and alkyl interactions, respectively. F17 and Y51 formed π - π stacking interactions with the fluorobenzene ring of the compound. In conclusion, I suggest that these two final compounds are potential candidates for controlling drug-resistant *K. pneumoniae*. This is the first report on small molecules controlling a bacterial TA system.

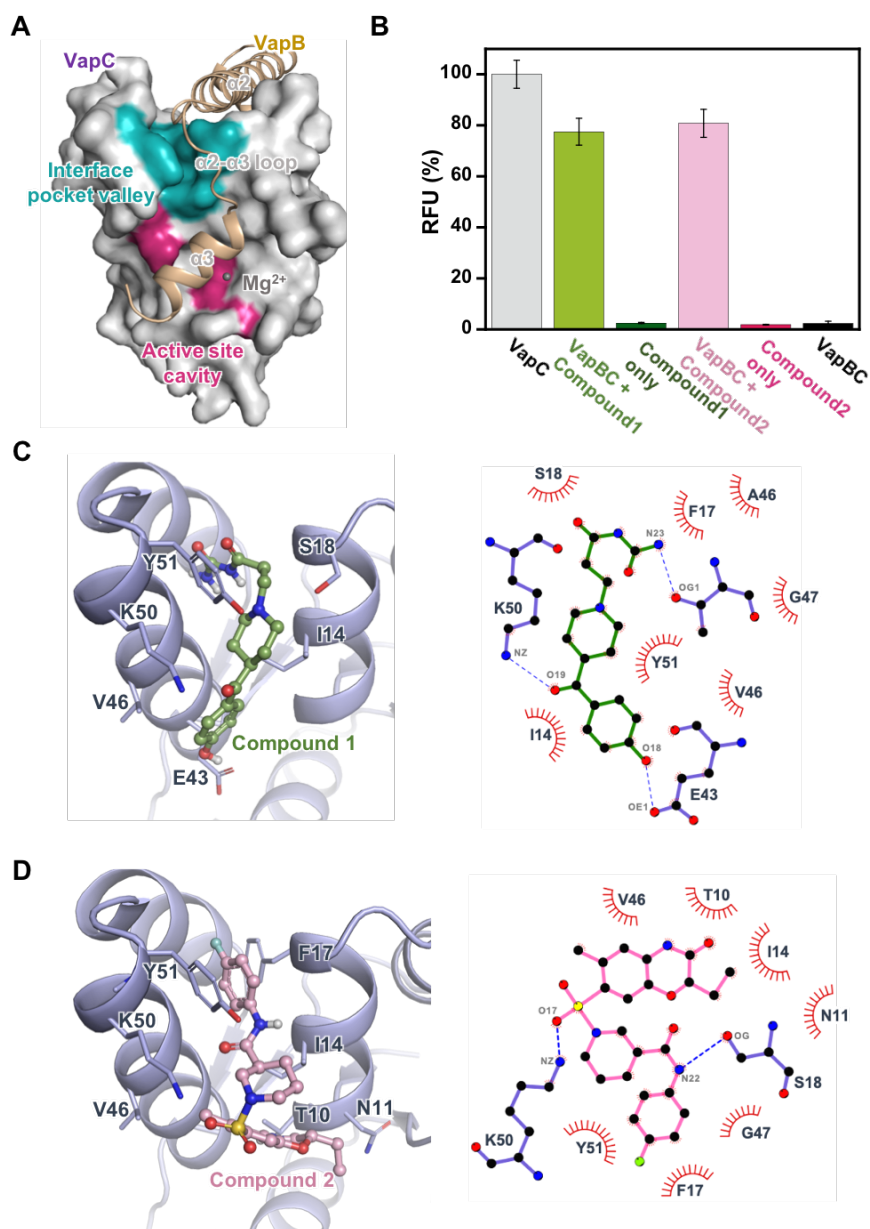


Figure 28. Surface pockets on VapC (PDB ID: 7BY3) and efficacy of final compounds expressed with molecular docking. **(A)** Surface of VapC with a cartoon representation of VapB. The negatively charged active-site cavity and surface cleft interface pockets are linked through the $\alpha 2$ – $\alpha 3$ loop of VapB. The compound-binding site of VapC is located on the surface cleft interface pockets represented as the interface pocket valley. **(B)** RNase activities of compounds when the VapBC complex was added. Activities generated by compounds are plotted in proportion to that of VapC. The activities of compounds without the VapBC complex were also measured. Pretreatments for these assays were the same as those described in Figure 25C. In these complex disruption assays, compound (1, 3.16, and 10 μ M) was added to 10 μ M protein, and the complex disruption efficacy was evaluated. The activity was measured based on the initial velocity during the first hour. Data are represented as the mean of three independent replicates \pm SD. **(C,D)** Results of molecular docking of the compounds on the VapC structure (PDB ID: 7BY3) with the detailed interaction networks. **(C)** Interaction data for compound 1. **(D)** Interaction data for compound 2. In the cartoon diagram, ligand-binding residues of VapC are shown in stick and labeled. 2D ligand-VapC

interaction diagrams were generated using LigPlot+ (93). Compounds 1 and 2 are shown in green and pink, respectively. The residues involved in HBs are shown, and HBs are represented by blue dashes. The residues making nonbonded contacts with the ligand are shown in the red spoked arcs.

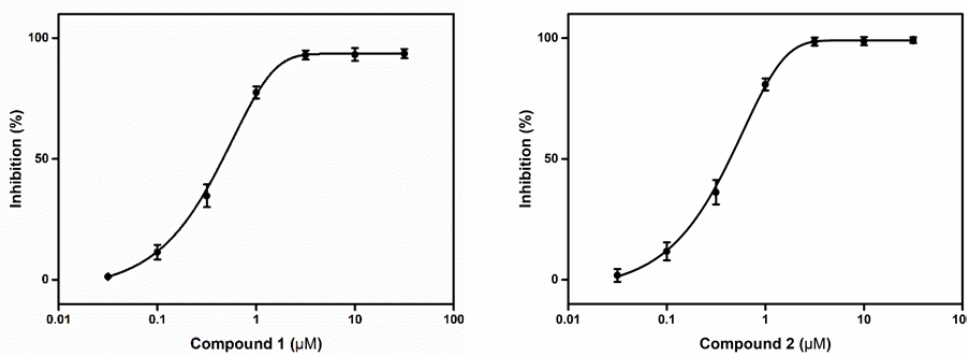


Figure 29. Inhibition curves of compounds. The data show the average values obtained in triplicate reactions; the standard deviations are indicated by error bars.

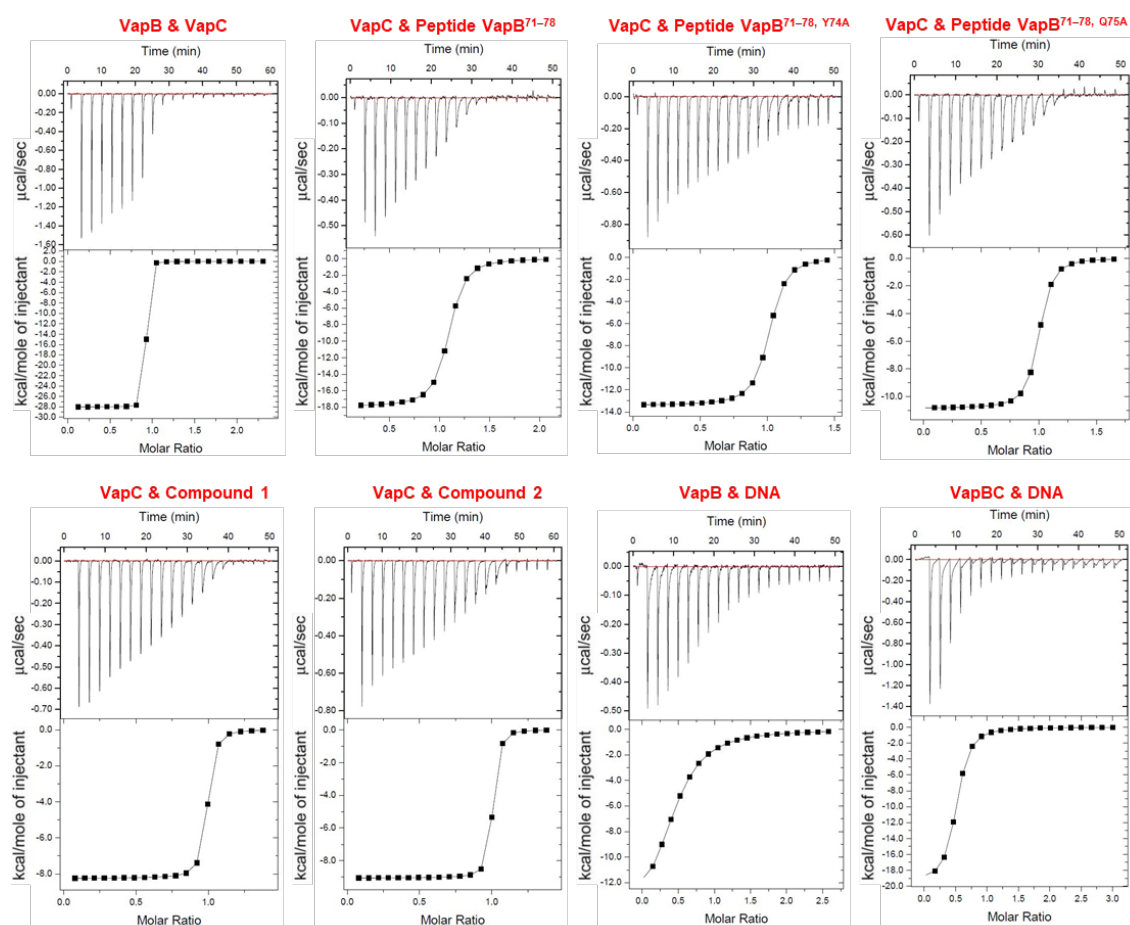
2.3.6 Insights based on binding affinity

To further verify the peptides and small molecules selected through this study, the binding affinities of VapC with VapB, peptides and small molecules were measured by ITC (Figure 30). VapB was most strongly coupled with VapC ($K_d = 3$ nM), and peptides and small molecules also showed affinities with VapC in the nanomolar range ($K_d = 110$ nM ~ 170 nM for peptides and 22 nM ~ 35 nM for small molecules) (Figure 30). Identifications of these affinities confirm that the peptides were successfully rationally designed as competitive inhibitors for the VapB binding region and that the proposed docking models of small molecules are reliable.

The affinities of the peptides VapB⁷¹⁻⁷⁸, VapB^{71-78, Y74A}, and VapB^{71-78, Q75A} to VapC were 110 nM, 170 nM and 150 nM, respectively (Figure 30). By mutation of Y74 and Q75, some interactions with VapC disappear, and the affinity with VapC decreases. However, Y74 and Q75 from VapB interact with the active site of VapC. Therefore, VapB^{71-78, Y74A}

and VapB^{71-78, Q75A} show higher activities than VapB⁷¹⁻⁷⁸ because of the decrease in inhibitions of VapC activity, despite their decreased binding affinity with VapC.

In type II TA systems, the antitoxin and toxin proteins play important roles in transcriptional autoregulation (94,95). To investigate the molecular mechanism of transcriptional regulation, the 28-bp DNA sequence at the promoter region was titrated into VapB and VapBC. The affinity of VapBC to DNA ($Kd = 1.26 \mu\text{M}$) was 5-fold higher than that of VapB ($Kd = 5.38 \mu\text{M}$) (Figure 30). This indicates that VapB serves as a primary repressor in autoregulation by directly binding to its own promoter, while VapC acts as a corepressor, enhancing the interaction between VapB and the operator site by forming a complex with VapB.



For-AAAAGCTATAGATTGCTCATAAATT CAT
 Rev-ATGAAGTTATGACAACTATAGCTTTT

	n (the binding stoichiometry)	K_d (μM)	ΔH (kcal mol^{-1})	$T\Delta S$ (kcal mol^{-1})	ΔG (kcal mol^{-1})
VapB & VapC	0.97 ± 0.002	0.003 ± 0.0002	-28.1 ± 0.04	-16.4	-44.5
VapC & Peptide VapB ⁷¹⁻⁷⁸	1.02 ± 0.002	0.11 ± 0.0002	-17.9 ± 0.07	-8.4	-26.3
VapC & Peptide VapB ^{71-78, Y74A}	0.99 ± 0.001	0.17 ± 0.0002	-13.4 ± 0.02	-4.17	-17.57
VapC & Peptide VapB ^{71-78, Q75A}	0.99 ± 0.001	0.15 ± 0.0003	-10.8 ± 0.02	-1.53	-12.33
VapC & Compound 1	0.98 ± 0.002	0.035 ± 0.0004	-8.3 ± 0.03	1.93	-6.37
VapC & Compound 2	0.99 ± 0.004	0.022 ± 0.0002	-9.1 ± 0.06	1.39	-7.71
VapB & DNA	0.48 ± 0.002	5.38 ± 0.0002	-15.3 ± 0.05	-8.08	-23.38
VapBC & DNA	0.49 ± 0.003	1.26 ± 0.0004	-19.54 ± 0.03	-11.51	-31.05

Figure 30. ITC assays. The components participating in each experiment and the resulting binding parameters are described in each plot.

2.4 Discussion

2.4.1 Insight into the tertiary structure of *K. pneumoniae*

VapBC complex

Based on the crystal structure of *K. pneumoniae* VapBC complex, the binding mode of VapB and VapC is distinctly clarified. In addition, I validated the *K. pneumoniae* VapBC is a bona-fide TA system through the result of growth assay. Comparing the tertiary structure of VapC toxin from *K. pneumoniae* with the structural homologs showed that they share similar folds; however, the binding pattern between VapC toxin and its cognate VapB antitoxin and the DNA-binding domain of VapB antitoxin were quite different. For example, VapB antitoxin could act as intrinsically disordered protein (IDP) in the absence of VapC toxin. It could have several advantages compared to well-folded proteins. One is that IDP is more susceptible to proteolysis than its toxin counterpart, which results in relatively easy degradation of antitoxin under stress condition (96). A second is that IDP could improve the efficacy of VapB antitoxin that binds with VapC toxin. It is demonstrated that IDPs require less residues to bind to extended surfaces than well-folded proteins (97). A third one is that IDP is important for toxin-antitoxin system regulation, which is also regarded as ‘conditional cooperativity’ (98,99). In a growing bacterial population, antitoxin alone or antitoxin-toxin complex specifically bind to their own promoters, resulting in moderate repression and robust repression, respectively. In contrast, exposure to stress, such as antibiotics or nutrient deprivation, leads to the activation of bacterial proteases, especially Lon and ClpXP, which preferentially cleave

the antitoxin, resulting in a transient excess of toxin (100-102). After that, the additional toxin interacts with existing complex, causing conformational change of the complex and bringing about robust transcription. In this autoregulatory mechanism, the former is regarded as negative feedback, while the latter is regarded as positive feedback (101). In the previous studies, most of TA systems exhibit conditional cooperativity, which exclude DinJ/YafQ and MqsRA systems (100). Overall, IDP of VapB antitoxin could play an important role in interacting with VapC toxin. In addition, although the first β -strand of the VapB N-terminus was not observed, VapB is expected to have an RHH DNA-binding domain (85) in the order $\beta 1$ - $\alpha 1$ - $\alpha 2$ at the N-terminus according to prediction. In the previous study, there are two main DNA-binding domains in VapB antitoxin, including RHH (85) and AbrB-type domain (89). However, the orientation of each DNA-binding domain differs not only in their type of domain but also within the same domain type. Hence, it causes a diversity of transcription regulation mechanisms and further explains the specificity in the recognition of their own promoter regions. Through the results of ITC experiments, VapB antitoxin alone and VapBC complex indeed bind with their 28-bp DNA sequence at the promoter region, although the affinity of VapBC to DNA was 5-fold higher than that of VapB. This indicates that VapB antitoxin serves as a moderate repressor by directly binding to its own promoter, while VapBC complex acts as a robust repressor through the interaction between VapB and VapC.

2.4.2 Insight into the mechanism of the *in vitro* ribonuclease activity of VapC

Through the sequence alignment of the VapC toxin with its sequence homologs, seven residues are highly conserved. Among them, four acidic residues (D9, E43, D90, D111) make up the active site of VapC toxin. In addition, RNase activity of VapC is only shown when divalent metal ions such as Mg^{2+} are present, which implies that Mg^{2+} acts as the co-factor of VapC. Interestingly, through the comparison of crystal structure of native form and SeMet form, the molecular mechanism of Mg^{2+} is clearly deduced. In detail, Mg^{2+} is located in the midst of the conserved active site residues (D9, E43 and D90) of VapC in the structure obtained from the SAD data; however, the R79 of VapB displaces Mg^{2+} to the center of residues D9, D90 and D111 of VapC in the structure of native form. In this regard, the former could be regarded as open form, while the latter is regarded as closed form; and role of R79 is Mg^{2+} switch which transform the VapC toxin from the open state to closed state. Furthermore, through the result of *in vitro* RNase assay using several VapC mutants, E43 is the residue with the largest contribution to RNase activity, while the contribution of D111 is negligible. Overall, as R79 of VapB acts as the Mg^{2+} switch, VapC active site inhibition is achieved by completely abolishing the contribution of E43 to the RNase activity. This inhibitory mechanism of the active site is first observed through two states of crystal structures.

According to the previous study, VapC toxins from *M. tuberculosis* were divided into two types of enzyme on the basis of their mode of action. One is ASL enzyme, which cleave tRNA in the anticodon stem loop (ASL); the other one is SRL enzyme which cut the 23S rRNA in the sarcin-rich loop (SRL) (103). Unfortunately, I could not speculate

which type the *K. pneumoniae* VapC belongs to, due to lacking of experimental data. However, the molecular mechanism of ribonuclease activity of *K. pneumoniae* VapC could be deduced by structural comparison. As a result, it is quite similar with *E. coli* RNase III. In detail, the Mg²⁺ was coordinated by the acidic residues (Asp and Glu) and surrounding water molecules, resulting in making water molecules deprotonated and activated. After that, water molecules become nucleophile to assist nucleophile attack by forming penta-covalent intermediate in phosphate group. Finally, the digested product is formed between the new phosphoryl bond and re-protonated 3' leaving group.

2.4.3 Insight into artificial toxin activation using small molecules and peptides

Based on the crystal structure of *K. pneumoniae* VapBC complex, I designed several small molecules and peptides, which can 'attack' the binding pocket between VapB and VapC to disrupt the VapBC complex. Through the result of *in vitro* RNase assay, it is demonstrated that the complex disruption capabilities of both inhibitors are quite strong. However, the MIC values of them are relatively high at present. Now, further effort to improve the present drawbacks is needed by using following strategies. One is to change the application of antimicrobial agents, and the other one is to modify the compounds or peptides themselves. The former seems to be a more challenging strategy, in which we make combination use of cephalosporins and my agents. Since antibiotics indeed transmit stressed signals to bacteria that possess TA systems, low concentrations of cephalosporins would induce the positive feedback loop of TA systems in target bacteria, including VapBC system. Thus, lower concentrations of my agents would be sufficient to arrest or

kill the cells. However, it would be difficult to control the concentration of cephalosporins and the timing of applying my agents to bacteria. For example, bacteria will switch from normal cells to persister cells at present of some antibiotics. The other strategy seems to be more popular and controllable at present. As a result, there are several methods of inhibitor modifications I could consider. As for peptides, their modification using conjugation strategies and surface modulation could be conducted to obtain better structure folding and permeability. However, it should be noted that α -helical peptides could exhibit hemolytic activities in some cases (104). It is suggested that helicity of designed peptides could be properly adjusted using D-amino acids, resulting in less hemolytic activity and enhanced stability of against proteolytic cleavage. Furthermore, it is worth considering that hydrophobicity of peptides could affect permeability of them. In previous study, it shows that hydrophobicity of designed peptides not only affect the activity of them but also change the range of targets. For instance, there is an optimal window of hydrophobicity, beyond which activity of designed peptide decreases rapidly (105). Also, some synthetic analog of peptides, such as magainin, can kill both Gram-negative and Gram-positive bacteria when they were modified to have higher hydrophobicity (106). Lastly, cytotoxicity of designed peptide would be affected by changing amino acid content. It was reported that P60.4 used against Methicillin-resistant *Staphylococcus aureus* (MRSA) exhibited less cytotoxic effects, when it was modified by replacing neutral amino acids (Asn and Gln) with positively charged residues (Arg) (107). As for small molecules, several factors, such as polarity, molecular weight, amine, amphiphilic and rigid, and low globularity, would be computationally analyzed and modified to make them rapidly traverse the membranes of gram-negative bacteria (108).

Furthermore, design of new derivatives using existing scaffold, which possess more interactive groups, would be more effective to disrupt the VapBC complex.

2.5 Conclusion

The structure of the VapBC complex in this study is the first reported structure of a TA complex in *K. pneumoniae*. The VapC toxin inhibition mechanism by VapB R79 displacing Mg^{2+} was revealed through two crystal structures, the open and closed forms of the active site. This is a novel finding first identified in the field of bacterial TA systems. Through the rational design of peptides mimicking the VapBC binding interface, which can disrupt the VapBC complex, the artificial activation of the toxin as an antibacterial strategy can be applied to *K. pneumoniae*. Furthermore, by discovering small compounds that effectively inhibit the formation of the VapBC complex even at low concentrations, controlling drug-resistant *K. pneumoniae* through modification with inhibitors may be possible.

References

1. Ogura, T. and Hiraga, S. (1983) Mini-F plasmid genes that couple host cell division to plasmid proliferation. *Proc Natl Acad Sci U S A*, **80**, 4784-4788.
2. Hayes, F. and Van Melderen, L. (2011) Toxins-antitoxins: diversity, evolution and function. *Crit Rev Biochem Mol Biol*, **46**, 386-408.
3. Otsuka, Y. (2016) Prokaryotic toxin-antitoxin systems: novel regulations of the toxins. *Curr Genet*, **62**, 379-382.
4. Harms, A., Brodersen, D.E., Mitarai, N. and Gerdes, K. (2018) Toxins, Targets, and Triggers: An Overview of Toxin-Antitoxin Biology. *Mol Cell*, **70**, 768-784.
5. Fernandez-Garcia, L., Blasco, L., Lopez, M., Bou, G., Garcia-Contreras, R., Wood, T. and Tomas, M. (2016) Toxin-Antitoxin Systems in Clinical Pathogens. *Toxins (Basel)*, **8**.
6. Kedzierska, B. and Hayes, F. (2016) Emerging Roles of Toxin-Antitoxin Modules in Bacterial Pathogenesis. *Molecules*, **21**.
7. Lee, K.Y. and Lee, B.J. (2016) Structure, Biology, and Therapeutic Application of Toxin-Antitoxin Systems in Pathogenic Bacteria. *Toxins (Basel)*, **8**.
8. Park, S.J., Son, W.S. and Lee, B.J. (2013) Structural overview of toxin-antitoxin systems in infectious bacteria: a target for developing antimicrobial agents. *Biochim Biophys Acta*, **1834**, 1155-1167.
9. Kang, S.M., Kim, D.H., Jin, C. and Lee, B.J. (2018) A Systematic Overview of Type II and III Toxin-Antitoxin Systems with a Focus on Druggability. *Toxins (Basel)*, **10**.

10. Henriques-Normark, B. and Tuomanen, E.I. (2013) The pneumococcus: epidemiology, microbiology, and pathogenesis. *Cold Spring Harb Perspect Med*, **3**.
11. Pletz, M.W., Maus, U., Krug, N., Welte, T. and Lode, H. (2008) Pneumococcal vaccines: mechanism of action, impact on epidemiology and adaption of the species. *Int J Antimicrob Agents*, **32**, 199-206.
12. Wahl, B., O'Brien, K.L., Greenbaum, A., Majumder, A., Liu, L., Chu, Y., Luksic, I., Nair, H., McAllister, D.A., Campbell, H. *et al.* (2018) Burden of *Streptococcus pneumoniae* and *Haemophilus influenzae* type b disease in children in the era of conjugate vaccines: global, regional, and national estimates for 2000-15. *Lancet Glob Health*, **6**, e744-e757.
13. von Mollendorf, C., Tempia, S., von Gottberg, A., Meiring, S., Quan, V., Feldman, C., Cloete, J., Madhi, S.A., O'Brien, K.L., Klugman, K.P. *et al.* (2017) Estimated severe pneumococcal disease cases and deaths before and after pneumococcal conjugate vaccine introduction in children younger than 5 years of age in South Africa. *PLoS One*, **12**, e0179905.
14. Bridy-Pappas, A.E., Margolis, M.B., Center, K.J. and Isaacman, D.J. (2005) *Streptococcus pneumoniae*: description of the pathogen, disease epidemiology, treatment, and prevention. *Pharmacotherapy*, **25**, 1193-1212.
15. Aliberti, S., Cook, G.S., Babu, B.L., Reyes, L.F., A, H.R., Sanz, F., Soni, N.J., Anzueto, A., Faverio, P., Sadud, R.F. *et al.* (2019) International prevalence and risk factors evaluation for drug-resistant *Streptococcus pneumoniae* pneumonia. *J Infect*, **79**, 300-311.

16. Fernandez-Garcia, L., Blasco, L., Lopez, M., Bou, G., Garcia-Contreras, R., Wood, T. and Tomas, M. (2016) Toxin-Antitoxin Systems in Clinical Pathogens. *Toxins (Basel)*, **8**, E227.
17. Gomez-Simmonds, A. and Uhlemann, A.C. (2017) Clinical Implications of Genomic Adaptation and Evolution of Carbapenem-Resistant *Klebsiella pneumoniae*. *J. Infect. Dis.*, **215**, S18-S27.
18. Peleg, A.Y. and Hooper, D.C. (2010) Hospital-acquired infections due to gram-negative bacteria. *N Engl J Med*, **362**, 1804-1813.
19. Velkov, T., Roberts, K.D., Nation, R.L., Thompson, P.E. and Li, J. (2013) Pharmacology of polymyxins: new insights into an 'old' class of antibiotics. *Future Microbiol*, **8**, 711-724.
20. Reygaert, W.C. (2018) An overview of the antimicrobial resistance mechanisms of bacteria. *AIMS Microbiol*, **4**, 482-501.
21. Livermore, D.M. (1987) Mechanisms of resistance to cephalosporin antibiotics. *Drugs*, **34 Suppl 2**, 64-88.
22. Sharma, A., Gupta, V.K. and Pathania, R. (2019) Efflux pump inhibitors for bacterial pathogens: From bench to bedside. *Indian J Med Res*, **149**, 129-145.
23. Ramirez, M.S. and Tolmasky, M.E. (2010) Aminoglycoside modifying enzymes. *Drug Resist Updat*, **13**, 151-171.
24. Hooper, D.C. and Jacoby, G.A. (2015) Mechanisms of drug resistance: quinolone resistance. *Ann N Y Acad Sci*, **1354**, 12-31.
25. Gomez, J.E., Kaufmann-Malaga, B.B., Wivagg, C.N., Kim, P.B., Silvis, M.R., Renedo, N., Ioerger, T.R., Ahmad, R., Livny, J., Fishbein, S. *et al.* (2017)

- Ribosomal mutations promote the evolution of antibiotic resistance in a multidrug environment. *Elife*, **6**.
26. Christensen, S.K., Maenhaut-Michel, G., Mine, N., Gottesman, S., Gerdes, K. and Van Melderen, L. (2004) Overproduction of the Lon protease triggers inhibition of translation in *Escherichia coli*: involvement of the yefM-yoeB toxin-antitoxin system. *Mol Microbiol*, **51**, 1705-1717.
 27. Leung, E., Datti, A., Cossette, M., Goodreid, J., McCaw, S.E., Mah, M., Nakhamchik, A., Ogata, K., El Bakkouri, M., Cheng, Y.Q. *et al.* (2011) Activators of cylindrical proteases as antimicrobials: identification and development of small molecule activators of ClpP protease. *Chem Biol*, **18**, 1167-1178.
 28. Sass, P., Josten, M., Famulla, K., Schiffer, G., Sahl, H.G., Hamoen, L. and Brotz-Oesterhelt, H. (2011) Antibiotic acyldepsipeptides activate ClpP peptidase to degrade the cell division protein FtsZ. *Proc Natl Acad Sci U S A*, **108**, 17474-17479.
 29. Tettelin, H., Nelson, K.E., Paulsen, I.T., Eisen, J.A., Read, T.D., Peterson, S., Heidelberg, J., DeBoy, R.T., Haft, D.H., Dodson, R.J. *et al.* (2001) Complete genome sequence of a virulent isolate of *Streptococcus pneumoniae*. *Science*, **293**, 498-506.
 30. Hadzi, S., Garcia-Pino, A., Haesaerts, S., Jurenas, D., Gerdes, K., Lah, J. and Loris, R. (2017) Ribosome-dependent *Vibrio cholerae* mRNAse HlgB2 is regulated by a beta-strand sliding mechanism. *Nucleic Acids Res*, **45**, 4972-4983.

31. Schureck, M.A., Maehigashi, T., Miles, S.J., Marquez, J., Cho, S.E., Erdman, R. and Dunham, C.M. (2014) Structure of the *Proteus vulgaris* HigB-(HigA)₂-HigB toxin-antitoxin complex. *J Biol Chem*, **289**, 1060-1070.
32. Yang, J., Zhou, K., Liu, P., Dong, Y., Gao, Z., Zhang, J. and Liu, Q. (2016) Structural insight into the *E. coli* HigBA complex. *Biochem Biophys Res Commun*, **478**, 1521-1527.
33. Kruger, N.J. (1994) The Bradford method for protein quantitation. *Methods Mol Biol*, **32**, 9-15.
34. Adams, P.D., Afonine, P.V., Bunkoczi, G., Chen, V.B., Davis, I.W., Echols, N., Headd, J.J., Hung, L.W., Kapral, G.J., Grosse-Kunstleve, R.W. *et al.* (2010) PHENIX: a comprehensive Python-based system for macromolecular structure solution. *Acta Crystallogr D Biol Crystallogr*, **66**, 213-221.
35. Emsley, P., Lohkamp, B., Scott, W.G. and Cowtan, K. (2010) Features and development of Coot. *Acta Crystallogr D Biol Crystallogr*, **66**, 486-501.
36. Brunger, A.T. (1992) Free R value: a novel statistical quantity for assessing the accuracy of crystal structures. *Nature*, **355**, 472-475.
37. Murshudov, G.N., Skubak, P., Lebedev, A.A., Pannu, N.S., Steiner, R.A., Nicholls, R.A., Winn, M.D., Long, F. and Vagin, A.A. (2011) REFMAC5 for the refinement of macromolecular crystal structures. *Acta Crystallogr D Biol Crystallogr*, **67**, 355-367.
38. Chen, V.B., Arendall, W.B., Headd, J.J., Keedy, D.A., Immormino, R.M., Kapral, G.J., Murray, L.W., Richardson, J.S. and Richardson, D.C. (2010) MolProbity: all-atom structure validation for macromolecular crystallography. *Acta Crystallogr D Biol Crystallogr*, **66**, 12-21.

39. Delano, W.L. (2002) *The PyMOL Molecular Graphics System*. DeLano Scientific, San Carlos, CA.
40. Baker, N.A., Sept, D., Joseph, S., Holst, M.J. and McCammon, J.A. (2001) Electrostatics of nanosystems: application to microtubules and the ribosome. *Proc. Natl. Acad. Sci. U. S. A.*, **98**, 10037-10041.
41. Delaglio, F., Grzesiek, S., Vuister, G.W., Zhu, G., Pfeifer, J. and Bax, A. (1995) NMRPipe: a multidimensional spectral processing system based on UNIX pipes. *J. Biomol. NMR*, **6**, 277-293.
42. Johnson, B.A. (2004) Using NMRView to visualize and analyze the NMR spectra of macromolecules. *Methods Mol. Biol.*, **278**, 313-352.
43. Dominguez, C., Boelens, R. and Bonvin, A.M. (2003) HADDOCK: a protein-protein docking approach based on biochemical or biophysical information. *J. Am. Chem. Soc.*, **125**, 1731-1737.
44. van Dijk, M. and Bonvin, A.M. (2009) 3D-DART: a DNA structure modelling server. *Nucleic Acids Res.*, **37**, W235-W239.
45. Klose, D.P., Wallace, B.A. and Janes, R.W. (2010) 2Struc: the secondary structure server. *Bioinformatics*, **26**, 2624-2625.
46. Xiong, W., Li, T., Chen, K. and Tang, K. (2009) Local combinational variables: an approach used in DNA-binding helix-turn-helix motif prediction with sequence information. *Nucleic Acids Res.*, **37**, 5632-5640.
47. Thompson, J.D., Higgins, D.G. and Gibson, T.J. (1994) CLUSTAL W: improving the sensitivity of progressive multiple sequence alignment through sequence weighting, position-specific gap penalties and weight matrix choice. *Nucleic Acids Res*, **22**, 4673-4680.

48. Robert, X. and Gouet, P. (2014) Deciphering key features in protein structures with the new ENDscript server. *Nucleic Acids Res*, **42**, W320-324.
49. Holm, L. and Rosenstrom, P. (2010) Dali server: conservation mapping in 3D. *Nucleic Acids Res.*, **38**, W545-W549.
50. Aakre, C.D., Herrou, J., Phung, T.N., Perchuk, B.S., Crosson, S. and Laub, M.T. (2015) Evolving new protein-protein interaction specificity through promiscuous intermediates. *Cell*, **163**, 594-606.
51. Takagi, H., Kakuta, Y., Okada, T., Yao, M., Tanaka, I. and Kimura, M. (2005) Crystal structure of archaeal toxin-antitoxin RelE-RelB complex with implications for toxin activity and antitoxin effects. *Nat. Struct. Mol. Biol.*, **12**, 327-331.
52. Kamada, K. and Hanaoka, F. (2005) Conformational change in the catalytic site of the ribonuclease YoeB toxin by YefM antitoxin. *Mol Cell*, **19**, 497-509.
53. Schureck, M.A., Meisner, J., Hoffer, E.D., Wang, D., Onuoha, N., Ei Cho, S., Lollar, P., 3rd and Dunham, C.M. (2019) Structural basis of transcriptional regulation by the HigA antitoxin. *Mol Microbiol*, **111**, 1449-1462.
54. Neubauer, C., Gao, Y.G., Andersen, K.R., Dunham, C.M., Kelley, A.C., Hentschel, J., Gerdes, K., Ramakrishnan, V. and Brodersen, D.E. (2009) The structural basis for mRNA recognition and cleavage by the ribosome-dependent endonuclease RelE. *Cell*, **139**, 1084-1095.
55. Schureck, M.A., Repack, A., Miles, S.J., Marquez, J. and Dunham, C.M. (2016) Mechanism of endonuclease cleavage by the HigB toxin. *Nucleic Acids Res.*, **44**, 7944-7953.

56. Page, R. and Peti, W. (2016) Toxin-antitoxin systems in bacterial growth arrest and persistence. *Nat. Chem. Biol.*, **12**, 208-214.
57. Michiels, J.E., van den Bergh, B., Verstraeten, N. and Michiels, J. (2016) Molecular mechanisms and clinical implications of bacterial persistence. *Drug Resist. Updates*, **29**, 76-89.
58. Griffin, M.A., Davis, J.H. and Strobel, S.A. (2013) Bacterial toxin RelE: a highly efficient ribonuclease with exquisite substrate specificity using atypical catalytic residues. *Biochemistry*, **52**, 8633-8642.
59. Kang, S.M., Kim, D.H., Lee, K.Y., Park, S.J., Yoon, H.J., Lee, S.J., Im, H. and Lee, B.J. (2017) Functional Details of the *Mycobacterium tuberculosis* VapBC26 Toxin-Antitoxin System based on a Structural Study: Insights into Unique Binding and Antibiotic Peptides. *Nucleic Acids Res*, **45**, 8564-8580.
60. Kim, D.H., Kang, S.M., Park, S.J., Jin, C., Yoon, H.J. and Lee, B.J. (2018) Functional Insights into the *Streptococcus pneumoniae* HicBA Toxin-Antitoxin System Based on a Structural Study. *Nucleic Acids Res*, **46**, 6371-6386.
61. Chapman, R.N., Dimartino, G. and Arora, P.S. (2004) A highly stable short alpha-helix constrained by a main-chain hydrogen-bond surrogate. *J. Am. Chem. Soc.*, **126**, 12252-12253.
62. Cromm, P.M., Spiegel, J. and Grossmann, T.N. (2015) Hydrocarbon stapled peptides as modulators of biological function. *ACS Chem. Biol.*, **10**, 1362-1375.
63. Xie, Y., Wei, Y., Shen, Y., Li, X., Zhou, H., Tai, C., Deng, Z. and Ou, H.Y. (2018) TADB 2.0: An Updated Database of Bacterial Type II Toxin-Antitoxin Loci. *Nucleic Acids Res*, **46**, D749-D753.

64. Burley, S.K., Berman, H.M., Bhikadiya, C., Bi, C., Chen, L., Di Costanzo, L., Christie, C., Dalenberg, K., Duarte, J.M., Dutta, S. *et al.* (2019) RCSB Protein Data Bank: Biological Macromolecular Structures Enabling Research and Education in Fundamental Biology, Biomedicine, Biotechnology and Energy. *Nucleic Acids Res*, **47**, D464-D474.
65. Mattison, K., Wilbur, J.S., So, M. and Brennan, R.G. (2006) Structure of FitAB from *Neisseria gonorrhoeae* Bound to DNA Reveals a Tetramer of Toxin-Antitoxin Heterodimers Containing Pin Domains and Ribbon-Helix-Helix Motifs. *J. Biol. Chem.*, **281**, 37942-37951.
66. Dienemann, C., Boggild, A., Winther, K.S., Gerdes, K. and Brodersen, D.E. (2011) Crystal Structure of the VapBC Toxin-Antitoxin Complex from *Shigella Flexneri* Reveals a Hetero-Octameric DNA-Binding Assembly. *J. Mol. Biol.*, **414**, 713-722.
67. Mate, M.J., Vincentelli, R., Foos, N., Raoult, D., Cambillau, C. and Ortiz-Lombardia, M. (2012) Crystal Structure of the DNA-Bound VapBC2 Antitoxin/Toxin Pair from *Rickettsia felis*. *Nucleic Acids Res*, **40**, 3245-3258.
68. Bendtsen, K.L., Xu, K., Luckmann, M., Winther, K.S., Shah, S.A., Pedersen, C.N.S. and Brodersen, D.E. (2017) Toxin Inhibition in *C. Crescentus* VapBC1 is Mediated by a Flexible Pseudo-Palindromic Protein Motif and Modulated by DNA Binding. *Nucleic Acids Res*, **45**, 2875-2886.
69. Molinaro, A.L., Kashipathy, M.M., Lovell, S., Battaile, K.P., Coussens, N.P., Shen, M. and Daines, D.A. (2019) Crystal Structure of VapBC-1 from Nontypeable *Haemophilus influenzae* and the Effect of PIN Domain Mutations on Survival during Infection. *J. Bacteriol.*, **201**, e00026-00019.

70. Min, A.B., Miallau, L., Sawaya, M.R., Habel, J., Cascio, D. and Eisenberg, D. (2012) The Crystal Structure of the Rv0301-Rv0300 VapBC-3 Toxin-Antitoxin Complex from *M. tuberculosis* Reveals a Mg(2)(+) Ion in the Active Site and a Putative RNA-Binding Site. *Protein Sci.*, **21**, 1754-1767.
71. Miallau, L., Faller, M., Chiang, J., Arbing, M., Guo, F., Cascio, D. and Eisenberg, D. (2009) Structure and Proposed Activity of a Member of the VapBC Family of Toxin-Antitoxin Systems. VapBC-5 from *Mycobacterium tuberculosis*. *J. Biol. Chem.*, **284**, 276-283.
72. Deep, A., Tiwari, P., Agarwal, S., Kaundal, S., Kidwai, S., Singh, R. and Thakur, K.G. (2018) Structural, Functional and Biological Insights into the Role of *Mycobacterium tuberculosis* VapBC11 Toxin-Antitoxin System: Targeting a tRNase to Tackle Mycobacterial Adaptation. *Nucleic Acids Res*, **46**, 11639-11655.
73. Das, U., Pogenberg, V., Subhramanyam, U.K., Wilmanns, M., Gourinath, S. and Srinivasan, A. (2014) Crystal Structure of the VapBC-15 Complex from *Mycobacterium tuberculosis* Reveals a Two-Metal Ion Dependent PIN-Domain Ribonuclease and a Variable Mode of Toxin-Antitoxin Assembly. *J. Struct. Biol.*, **188**, 249-258.
74. Lee, I.G., Lee, S.J., Chae, S., Lee, K.Y., Kim, J.H. and Lee, B.J. (2015) Structural and Functional Studies of the *Mycobacterium tuberculosis* VapBC30 Toxin-Antitoxin System: Implications for the Design of Novel Antimicrobial Peptides. *Nucleic Acids Res*, **43**, 7624-7637.
75. Williams, J.J. and Hergenrother, P.J. (2012) Artificial Activation of Toxin-Antitoxin Systems as an Antibacterial Strategy. *Trends Microbiol.*, **20**, 291-298.

76. Rownicki, M., Pienko, T., Czarnecki, J., Kolanowska, M., Bartosik, D. and Trylska, J. (2018) Artificial Activation of *Escherichia coli* mazEF and hipBA Toxin-Antitoxin Systems by Antisense Peptide Nucleic Acids as an Antibacterial Strategy. *Front. Microbiol.*, **9**, 2870.
77. Otwinowski, Z. and Minor, W. (1997) [20] Processing of X-Ray Diffraction Data Collected in Oscillation Mode. *Method Enzymol*, **276**, 307-326.
78. Adams, P.D., Afonine, P.V., Bunkoczi, G., Chen, V.B., Davis, I.W., Echols, N., Headd, J.J., Hung, L.W., Kapral, G.J., Grosse-Kunstleve, R.W. *et al.* (2010) PHENIX: A Comprehensive Python-Based System for Macromolecular Structure Solution. *Acta Crystallogr. Sect. D: Biol. Crystallogr.*, **66**, 213-221.
79. Emsley, P., Lohkamp, B., Scott, W.G. and Cowtan, K. (2010) Features and Development of Coot. *Acta Crystallogr. Sect. D: Biol. Crystallogr.*, **66**, 486-501.
80. Murshudov, G.N., Skubak, P., Lebedev, A.A., Pannu, N.S., Steiner, R.A., Nicholls, R.A., Winn, M.D., Long, F. and Vagin, A.A. (2011) REFMAC5 for the Refinement of Macromolecular Crystal Structures. *Acta Crystallogr. Sect. D: Biol. Crystallogr.*, **67**, 355-367.
81. Chen, V.B., Arendall, W.B., 3rd, Headd, J.J., Keedy, D.A., Immormino, R.M., Kapral, G.J., Murray, L.W., Richardson, J.S. and Richardson, D.C. (2010) MolProbity: All-Atom Structure Validation for Macromolecular Crystallography. *Acta Crystallogr. Sect. D: Biol. Crystallogr.*, **66**, 12-21.
82. Arcus, V.L., McKenzie, J.L., Robson, J. and Cook, G.M. (2011) The PIN-Domain Ribonucleases and the Prokaryotic VapBC Toxin-Antitoxin Array. *Protein Eng. Des. Sel.*, **24**, 33-40.

83. Wu, G., Robertson, D.H., Brooks, C.L., 3rd and Vieth, M. (2003) Detailed Analysis of Grid-based Molecular Docking: A Case Study of CDOCKER-A CHARMM-Based MD Docking Algorithm. *J. Comput. Chem.*, **24**, 1549-1562.
84. Buchan, D.W.A. and Jones, D.T. (2019) The PSIPRED Protein Analysis Workbench: 20 Years on. *Nucleic Acids Res*, **47**, W402-W407.
85. Schreiter, E.R. and Drennan, C.L. (2007) Ribbon-Helix-Helix Transcription Factors: Variations on a Theme. *Nat. Rev. Microbiol.*, **5**, 710-720.
86. McWilliam, H., Li, W., Uludag, M., Squizzato, S., Park, Y.M., Buso, N., Cowley, A.P. and Lopez, R. (2013) Analysis Tool Web Services from the EMBL-EBI. *Nucleic Acids Res*, **41**, W597-W600.
87. Robert, X. and Gouet, P. (2014) Deciphering Key Features in Protein Structures with the New ENDscript Server. *Nucleic Acids Res*, **42**, W320-W324.
88. Arcus, V.L., Rainey, P.B. and Turner, S.J. (2005) The PIN-Domain Toxin-Antitoxin Array in Mycobacteria. *Trends Microbiol.*, **13**, 360-365.
89. Coles, M., Djuranovic, S., Soding, J., Frickey, T., Koretke, K., Truffault, V., Martin, J. and Lupas, A.N. (2005) AbrB-Like Transcription Factors Assume a Swapped Hairpin Fold that is Evolutionarily Related to Double-Psi Beta Barrels. *Structure*, **13**, 919-928.
90. Krissinel, E. and Henrick, K. (2007) Inference of Macromolecular Assemblies from Crystalline State. *J. Mol. Biol.*, **372**, 774-797.
91. Tina, K.G., Bhadra, R. and Srinivasan, N. (2007) PIC: Protein Interactions Calculator. *Nucleic Acids Res*, **35**, W473-W476.

92. Luong, H.X., Kim, D.H., Lee, B.J. and Kim, Y.W. (2018) Effects of Lysine-to-Arginine Substitution on Antimicrobial Activity of Cationic Stapled Heptapeptides. *Arch. Pharmacol Res.*, **41**, 1092-1097.
93. Laskowski, R.A. and Swindells, M.B. (2011) LigPlot+: multiple ligand-protein interaction diagrams for drug discovery. *J Chem Inf Model*, **51**, 2778-2786.
94. Kedzierska, B., Lian, L.Y. and Hayes, F. (2007) Toxin-Antitoxin Regulation: Bimodal Interaction of YefM-YoeB with Paired DNA Palindromes Exerts Transcriptional Autorepression. *Nucleic Acids Res*, **35**, 325-339.
95. Overgaard, M., Borch, J., Jorgensen, M.G. and Gerdes, K. (2008) Messenger RNA Interferase RelE Controls relBE Transcription by Conditional Cooperativity. *Mol. Microbiol.*, **69**, 841-857.
96. van der Lee, R., Lang, B., Kruse, K., Gsponer, J., Sanchez de Groot, N., Huynen, M.A., Matouschek, A., Fuxreiter, M. and Babu, M.M. (2014) Intrinsically disordered segments affect protein half-life in the cell and during evolution. *Cell Rep*, **8**, 1832-1844.
97. Ragusa, M.J., Dancheck, B., Critton, D.A., Nairn, A.C., Page, R. and Peti, W. (2010) Spinophilin directs protein phosphatase 1 specificity by blocking substrate binding sites. *Nat Struct Mol Biol*, **17**, 459-464.
98. Garcia-Pino, A., Balasubramanian, S., Wyns, L., Gazit, E., De Greve, H., Magnuson, R.D., Charlier, D., van Nuland, N.A. and Loris, R. (2010) Allostery and intrinsic disorder mediate transcription regulation by conditional cooperativity. *Cell*, **142**, 101-111.

99. De Jonge, N., Garcia-Pino, A., Buts, L., Haesaerts, S., Charlier, D., Zangger, K., Wyns, L., De Greve, H. and Loris, R. (2009) Rejuvenation of CcdB-poisoned gyrase by an intrinsically disordered protein domain. *Mol Cell*, **35**, 154-163.
100. Page, R. and Peti, W. (2016) Toxin-antitoxin systems in bacterial growth arrest and persistence. *Nat Chem Biol*, **12**, 208-214.
101. Nikolic, N. (2019) Autoregulation of bacterial gene expression: lessons from the MazEF toxin-antitoxin system. *Curr Genet*, **65**, 133-138.
102. Nikolic, N., Bergmiller, T., Vandervelde, A., Albanese, T.G., Gelens, L. and Moll, I. (2018) Autoregulation of mazEF expression underlies growth heterogeneity in bacterial populations. *Nucleic Acids Res*, **46**, 2918-2931.
103. Winther, K., Tree, J.J., Tollervey, D. and Gerdes, K. (2016) VapCs of *Mycobacterium tuberculosis* cleave RNAs essential for translation. *Nucleic Acids Res*, **44**, 9860-9871.
104. Papo, N., Oren, Z., Pag, U., Sahl, H.G. and Shai, Y. (2002) The consequence of sequence alteration of an amphipathic alpha-helical antimicrobial peptide and its diastereomers. *J Biol Chem*, **277**, 33913-33921.
105. Chen, L. and Harrison, S.D. (2007) Cell-penetrating peptides in drug development: enabling intracellular targets. *Biochem Soc Trans*, **35**, 821-825.
106. Dathe, M., Wieprecht, T., Nikolenko, H., Handel, L., Maloy, W.L., MacDonald, D.L., Beyermann, M. and Bienert, M. (1997) Hydrophobicity, hydrophobic moment and angle subtended by charged residues modulate antibacterial and haemolytic activity of amphipathic helical peptides. *FEBS Lett*, **403**, 208-212.
107. Goblyos, A., Schimmel, K.J., Valentijn, A.R., Fathers, L.M., Cordfunke, R.A., Chan, H.L., Oostendorp, J., Nibbering, P.H., Drijfhout, J.W., Hiemstra, P.S. *et*

- al.* (2013) Development of a nose cream containing the synthetic antimicrobial peptide P60.4Ac for eradication of methicillin-resistant *Staphylococcus aureus* carriage. *J Pharm Sci*, **102**, 3539-3544.
108. Richter, M.F., Drown, B.S., Riley, A.P., Garcia, A., Shirai, T., Svec, R.L. and Hergenrother, P.J. (2017) Predictive compound accumulation rules yield a broad-spectrum antibiotic. *Nature*, **545**, 299-304.

국문초록

*Streptococcus pneumoniae*와 *Klebsiella pneumoniae*에서 유래한 두가지 toxin-antitoxin system 단백질의 구조적, 기능적 연구

독소-항독소(TA) 시스템은 박테리아내에서 주요한 세포 기능을 조절한다. 이번 연구를 통하여 폐렴 연쇄상구균에서 유래한 HigBA 계열 단백질의 3차원 구조를 밝히고 또한 HigB 독소를 활성화 시키면서 mRNA의 분해를 촉진하여 박테리아를 사멸할 수 있는 새로운 기전의 항생물질을 발굴하게 되었다. 단백질의 3차원 구조를 기반으로 펩타이드가 설계되었고 폐렴 연쇄상구균의 세포막을 침투하여 박테리아를 사멸하는데 성공하였다. 이번 발견은 항생제에 내성이 있는 폐렴 연쇄상구균의 치료에서 주목할 만한 이정표이며, 박테리아의 사멸 기전은 기존의 항생제와는 완전히 다르다. 또한 HigBA 복합체는 HigA 항독소의 N 말단과 C 말단에 존재하는 두개의 분자 간 β -평면 구조를 통하여 교차-가위 인터페이스를 보인다는 것을 발견하였다. 우리의 생화학 및 구조 연구는 HigA 항독소의 구조적 변동성과 관련된 전사 조절 기전의 관한 정보를 제공했다. 또한 HigB 독소의 촉매 활성화와 관련된 잔기들 및 그들의 기능 관계를 *in vivo* 실험을 통하여 밝혀냈다. 또한, HigBA 복합체를 교란시켜 독소를 방출하는 독소 모방 또는

항독소 모방 펩타이드가 고안되어 새로운 개념 항생제 개발에 대한 접근 방법을 제공하였다. 결론적으로 HigBA 복합체에 관한 구조적인 분석은 새로운 항생제 개발 전략에 발판을 마련해 주었다.

폐렴간균은 가장 중요한 기회감염균 중 하나이다. TA 시스템은 병원성 박테리아의 생존과 관련이 있기 때문에 유망한 약물 타겟이다. 그러나 현재 폐렴간균의 TA 시스템에 대한 구조적 정보는 여전히 부족하다. 따라서 항생제 개발을 위해 이에 관한 정보를 연구할 필요가 있다. 이번 연구를 통하여 우리는 2.00 Å 의 해상도로 폐렴간균에서 유래한 VapBC 복합체의 첫 번째 결정 구조를 제시하게 되었다. 우리는 Mg²⁺ 스위치를 통해 VapB 항독소의 독소 억제 메커니즘을 규명하게 되었고 이 스위치에서 Mg²⁺는 VapB 의 R79 에 의해 변위 되는 것을 확인할 수 있었다. VapC 독소의 활성화 부위의 관한 이러한 억제 메커니즘은 박테리아의 TA 시스템에서의 최초의 발견이다. 또한 VapC 독소를 활성화하는 펩타이드와 소분자 화합물을 포함한 억제제가 발견 되었다. 이러한 억제제는 VapBC 복합체를 교란시키고 VapC 독소를 활성화함으로써 항생제의 역할을 할 수 있다. 폐렴간균 유래의 VapBC 시스템에 대한 이번 연구결과는 VapBC 시스템의 미해결 난제를 설명하고 잠재적인 항생제를 개발하는 데 도움이 될 것이다.

주요어: 독소-항독소 시스템, HigBA, VapBC, X-선 결정학, 핵자기공명

학번: 2017-38501